University of Kentucky
UKnowledge

Theses and Dissertations--Chemical and Materials Engineering

Chemical and Materials Engineering

2023

MOLECULAR UNDERSTANDING OF ZWITTERIONS AND QUANTUM COMPUTING FOR SUSTAINABILITY

Manh Tien Nguyen
University of Kentucky, tienmng7@gmail.com
Author ORCID Identifier:
https://orcid.org/0000-0001-5264-3583
Digital Object Identifier: https://doi.org/10.13023/etd.2023.370

Right click to open a feedback form in a new tab to let us know how this document benefits you.

Recommended Citation
Nguyen, Manh Tien, "MOLECULAR UNDERSTANDING OF ZWITTERIONS AND QUANTUM COMPUTING FOR SUSTAINABILITY" (2023). *Theses and Dissertations--Chemical and Materials Engineering*. 154.
https://uknowledge.uky.edu/cme_etds/154

This Doctoral Dissertation is brought to you for free and open access by the Chemical and Materials Engineering at UKnowledge. It has been accepted for inclusion in Theses and Dissertations--Chemical and Materials Engineering by an authorized administrator of UKnowledge. For more information, please contact UKnowledge@lsv.uky.edu.

STUDENT AGREEMENT:

I represent that my thesis or dissertation and abstract are my original work. Proper attribution has been given to all outside sources. I understand that I am solely responsible for obtaining any needed copyright permissions. I have obtained needed written permission statement(s) from the owner(s) of each third-party copyrighted matter to be included in my work, allowing electronic distribution (if such use is not permitted by the fair use doctrine) which will be submitted to UKnowledge as Additional File.

I hereby grant to The University of Kentucky and its agents the irrevocable, non-exclusive, and royalty-free license to archive and make accessible my work in whole or in part in all forms of media, now or hereafter known. I agree that the document mentioned above may be made available immediately for worldwide access unless an embargo applies.

I retain all other ownership rights to the copyright of my work. I also retain the right to use in future works (such as articles or books) all or part of my work. I understand that I am free to register the copyright to my work.

REVIEW, APPROVAL AND ACCEPTANCE

The document mentioned above has been reviewed and accepted by the student's advisor, on behalf of the advisory committee, and by the Director of Graduate Studies (DGS), on behalf of the program; we verify that this is the final, approved version of the student's thesis including all changes required by the advisory committee. The undersigned agree to abide by the statements above.

Manh Tien Nguyen, Student

Dr. Qing Shao, Major Professor

Dr. J. Zach Hilt, Director of Graduate Studies

MOLECULAR UNDERSTANDING OF ZWITTERIONS AND QUANTUM COMPUTING FOR SUSTAINABILITY

DISSERTATION

A dissertation submitted in partial fulfillment of the
requirements for the degree of Doctor of Philosophy in the
College of Engineering
at the University of Kentucky

By
Manh Tien Nguyen
Lexington, Kentucky
Director: Dr. Qing Shao, Professor of Chemical and Materials Engineering
Lexington, Kentucky
2023

Copyright © Manh Tien Nguyen 2023
https://orcid.org/0000-0001-5264-3583

ABSTRACT OF DISSERTATION

MOLECULAR UNDERSTANDING OF ZWITTERIONS
AND QUANTUM COMPUTING FOR SUSTAINABILITY

The sustainable development of society needs sustainable energy solutions and the mitigation of greenhouse gas emissions. One key subject in this area is the development of safe and efficient ion-based batteries. Moreover, CO_2 capture is a crucial pathway in mitigating emissions from the combustion of fossil fuels. Ongoing efforts are to improve both technologies' safety and efficiency. This thesis presents our efforts to conduct computational research on understanding advanced zwitterionic electrolytes and CO_2 capture. Chapters 2-4 illustrate the computational research to understand ionic solvation in zwitterionic electrolytes. Solid-state electrolytes are essential for safer batteries. While solid polymer electrolytes have advantages such as high safety standards, flexibility, and ease of processing, they suffer from low ionic conductivity. Zwitterionic (ZW) materials have potential due to their unique structures and properties, offering high ionic conductivity and mechanical strength. However, the understanding of their underlying mechanisms and design principles is limited. Our study investigated the effect of ZW molecules in lithium salts and poly(ethylene oxide)-based (PEO) electrolytes through molecular dynamics simulations. We found that ZW molecules can make small Li^+ and large anions diffuse at the same level under an electric field and have two distinct effects on Li^+ transport and solvation in PEO electrolytes. ZW molecules can release Li^+ from the trapping effect of EO chains, enhancing Li^+ transport and slowing down Li^+ transport by strong Li^+-ZW associations. The accelerating effect becomes stronger as the EO chain length increases. We also studied how the chemical structure of ZW molecules affects their ionic disassociation effect and found that MPC, SB, and CB reduce Li^+–EO association in the order of MPC > CB > SB (MPC: 2-methacryloyloxyethyl phosphorylcholine, SB: sulfobetaine ethylimidazole, CB: carboxybetaine ethylimidazole). Our simulations suggest that ZW molecule additives may be beneficial in high Li^+ concentration environments. At a low Li^+ concentration, all three molecules decrease Li^+ diffusion, but at a high Li^+ concentration, only SB has this effect. Chapter 5 illustrates our effort to develop quantum computing on CO_2 capture. Quantum computing has the potential to enhance the efficiency, accuracy, and capabilities of simulating CO_2 capture reactions through increased computational power, precision, and resources. In addition to molecular electronic energies, vibrational properties are crucial for understanding reaction kinetics. However, the anharmonicity effect correlates with the molecule size and plays a substantial role in molecular vibrational properties, which can be challenging to address using classical computing. By employing a variational quantum eigensolver algorithm, this work calculates both the molecular electronic and vibrational energies for the reaction pathways between CO_2 and NH_3. The study showcased the potential of quantum computing for calculating the vibrational energies of large molecules, thus demonstrating its applications in the study of CO_2 capture reactions. In summary, this work illustrates the fundamental relationship between the chemical structures of ZW molecules and their ability to alter the ionic solvation and transport in electrolytes. This relationship can be used to rationalize the

design of advanced electrolytes with high ionic conductivity. This work also illustrates the potential of quantum computing in enabling the computation of molecular properties critical for CO_2 capture and conversion.

KEYWORDS: Zwitterion, Lithium-ion electrolytes, CO_2 capture, Quantum computing

Manh Tien Nguyen

(Name of Student)

06/21/2023

Date

MOLECULAR UNDERSTANDING OF ZWITTERIONS
AND QUANTUM COMPUTING FOR SUSTAINABILITY

By
Manh Tien Nguyen

Dr. Qing Shao
Director of Dissertation

Dr. Zach Hilt
Director of Graduate Studies

06/21/2023
Date

DEDICATION

To *my grandparents, parents, brother, and sisters.*

ACKNOWLEDGMENTS

First and foremost, I am deeply indebted to my advisor Dr. Qing Shao, who is not only a remarkable teacher but also an exceptional mentor. Your guidance, unwavering support, and insightful advice have been instrumental in shaping my research and helping me navigate through life's challenges. I am greatly grateful to you for equipping me with the skills needed to succeed in life. I truly believe that without your influence, I would not be the person I am today.

I extend my sincerest appreciation to my family—my parents, sisters, and brother—for your constant support and presence by my side from the very first day I arrived in the United States. Your love, encouragement, and sacrifices have been a constant source of strength throughout my doctoral journey.

To my dear friends, Francisco Leniz and Usman Abbas, who have been with me since the beginning to the end of my doctorate, I am incredibly thankful for your help, support, and companionship. Your presence has made this journey all the more meaningful and memorable. I am also grateful to all the friends I have had the opportunity to meet, spend time with, and be influenced by, such as Ufuoma Kara, Xu Nan, and Japheth E. Gado. Each of you has left an indelible mark on my life, and I am grateful for the experiences we have shared.

I am truly fortunate to have had the privilege of working with mentors at the National Energy Technology Laboratory, namely Dr. Yuhua Duan, Dr. Yueh-lin Lee, Dr. Dominic Alfonso, and Dr. Fan Shi. Your kindness, support, and expertise during my internship and SCGSR program have been instrumental in my professional development.

To my friends, Deb Becker and Bruce Becker, who have always kept me in their prayers, I am deeply grateful for your spiritual support and positive energy.

Lastly, I would like to express my gratitude to God for making all of this possible. The opportunities, blessings, and growth I have experienced throughout my doctoral journey are a testament to His grace and guidance.

TABLE OF CONTENTS

MOLECULAR UNDERSTANDING OF ZWITTERIONS AND QUANTUM COMPUTING FOR SUSTAINABILITY i

ABSTRACT OF DISSERTATION i

ACKNOWLEDGMENTS iii

TABLE OF CONTENTS v

LIST OF TABLES viii

LIST OF FIGURES ix

CHAPTER 1. INTRODUCTION 1

1.1 Introduction 1

CHAPTER 2. EFFECT OF ZWITTERIONIC MOLECULES ON IONIC TRANSPORT UNDER ELECTRIC FIELDS 5

2.1 Introduction 5

2.2 Molecular model and simulation detail 8

2.2.1 Molecular model 8

2.2.2 Simulation detail 10

2.3 Results and discussion 12

2.3.1 Diffusion coefficients of Li^+, anions and Z2C molecules 12

2.3.2 Structure of association among Li^+, anions, and Z2C molecules 14

2.3.3 Association residence time 19

2.3.4 Effect of scaled charges on association and diffusion in the electrolytes 21

2.3.5 Ionic conductivity 24

2.3.6 Conclusion 26

CHAPTER 3. ZWITTERIONIC EFFECTS ON IONIC ASSOCIATION IN ETHYLENE OXIDE-BASED ELECTROLYTES 27

3.1 Introduction 27

3.2 Molecular model and simulation detail 30

3.2.1 Molecular model 30

3.2.2 Simulation detail 32

3.3 Results and discussion 33

3.3.1 Diffusion coefficients of ions, EO_x and ZW molecules 33
3.3.2 Radial distribution functions 37
3.3.3 Association number 41
3.3.4 Association status 42
3.3.5 Association dynamics 47
3.3.6 Conclusion 50

CHAPTER 4. DISTINCT EFFECT OF ZWITTERIONIC MOLECULES ON IONIC SOLVATION IN (ETHYLENE OXIDE)$_{10}$: A MOLECULAR DYNAMICS SIMULATION STUDY 52

4.1 Introduction *52*

4.2 Methods *55*
4.2.1 Molecular Models 55
4.2.2 Simulation Details 57
4.2.3 Sigma profile calculation 57

4.3 Results and Discussion *59*
4.3.1 Radial Distribution Functions (RDFs) 59
4.3.2 Coordination Number 62
4.3.3 Percentage of Li^+ leaving the coordination with EO_{10} chains 64
4.3.4 Li^+ coordination lifetime 67
4.3.5 Diffusion coefficients 69
4.3.6 Radius of gyration of EO_{10} 73
4.3.7 Sigma profiles 74
4.3.8 Effect of simulation temperature 75

4.4 Conclusion *76*

CHAPTER 5. DESCRIPTION OF REACTION AND VIBRATIONAL ENERGETICS OF CO_2-NH_3 INTERACTION USING QUANTUM COMPUTING ALGORITHMS... 78

5.1 Introduction *78*

5.2 Calculation Methods *81*
5.2.1 Reaction profile construction 81
5.2.2 Ground state vibrational energy calculation 82

5.3 Results and Discussions *86*
5.3.1 Reaction profile based on the electronic energy calculations 86
5.3.2 Assessment of molecular ground state vibrational energies in noiseless simulations 88
5.3.3 Quantum computation of vibrational structures in noise simulations 91
5.3.4 Quantum computation of the vibrational excited states 92

5.4 Conclusion *94*

CHAPTER 6. CONCLUSIONS AND PERSPECTIVE 96
6.1 Conclusions *96*
6.2 Perspective *98*
APPENDICES 100
APPENDIX 1. SUPPORTING INFORMATION FOR CHAPTER 2 ..... *100*
APPENDIX 2. SUPPORTING INFORMATION FOR CHAPTER 3 ..... *108*
APPENDIX 3. SUPPORTING INFORMATION FOR CHAPTER 4 ..... *114*
REFERENCES 127
VITA 143

LIST OF TABLES

Table 3.1. Details of the simulation systems 31
Table 3.2. Details of the snapshots in Figure 3.13. 47
Table 4.1. Coordination numbers of Li^+-O in case-A systems 62
Table 4.2. Coordination numbers of Li^+-O in case-B systems 63
Table 4.3. Percentage of Li^+ only coordinating with ZW 65
Table 5.1. Quantum circuit resource estimation for the calculation of the ground-state vibrational energy of CO_2, NH_3, and NH_2COOH with the UVCC and CHC approaches with single excitation. The number of CNOT gates (CX) is given for both approaches.. 84
Table 5.2. Results of vibrational energy calculations for CO2, NH3, and NH2COOH molecules. 93

LIST OF FIGURES

Figure 1.1. Organizational overview of the dissertation 4
Figure 2.1. Molecular structures of zwitterionic molecules and anions in this work. (a) Z2C, (b) Z3C, (c) $[TFSI]^-$ and (d) $[BETI]^-$. Every atom is labeled using a unique name... 9
Figure 2.2. Initial configuration of a simulation box containing 200 Li^+, 200 $[TFSI]^-$, and 200 Z2C molecules (Li^+ ions are represented using the VDW model and the others are represented by the CPK model). This figure was generated using VMD-1.9.1[84]..... 9
Figure 2.3. Diffusion coefficients (D) of Z2C molecules and ions in the z direction (the direction of the electric field) as a function of electric field strength (scaled charge) (a) LiTFSI, (b) Z2C/LiTFSI, (c) LiBETI and (d) Z2C/LiBETI. 12
Figure 2.4. Radial distribution functions (RDFs) in the electrolyte solutions (scaled charge). (a) Li^+-O11$[TSFI]^-$ in LiTFSI solution and (b) Li^+-O11$[TFSI]^-$ and (c) Li^+-O1(ZW) in Z2C/LiTFSI solution. The O11 of $[TFSI]^-$ and O1 of Z2C were shown in Figure 2.1 14
Figure 2.5. (a) Z2C-$[TFSI]^-$ and (b) Z2C-Z2C radial distribution functions (scaled charge) 16
Figure 2.6. Number of molecular and ionic associations in (a) Z2C/LiTFSI and (b) Z2C/LiBETI solutions (scaled charge). 17
Figure 2.7. Radial distribution functions in electrolyte solutions. (a) Li^+-O11$[BETI]^-$ and (b) Li^+-O1(ZW) in Z2C/LiBETI solution (scaled charge)..... 18
Figure 2.8. Residence curves C(t) for associations in Z2C/LiTFSI systems (scaled charge). (a) Li^+ and $[TFSI]^-$, (b) Li^+ and ZW, (c) ZW and $[TFSI]^-$; (d) ZW and ZW..... 19
Figure 2.9. Diffusion coefficients of Li^+, $[TFSI]^-$ and zwitterionic Z2C in the z direction as a function of electric field (full charge) (a) LiTFSI and (b) Z2C/LiTFSI 21
Figure 2.10. Association numbers in Z2C/LiTFSI electrolytes as a function of the electric field (full charge) 22
Figure 2.11. Association residence curves in Z2C/LiTFSI electrolytes (full charge). (a) Li^+ and $[TFSI]^-$; (b) Li^+ and ZW; (c) ZW and $[TFSI]^-$; and (d) ZW and ZW 23
Figure 2.12. Ionic conductivity of Z2C/LiTFSI and Z3C/LiTFSI electrolytes without electric field. 24
Figure 2.13. Ionic conductivity of electrolytes under electric field. (a) Z2C/LiTFSI; (b) Z2C/LiBETI..... 25
Figure 3.1. Molecular structures of (a) ZW, (b) $[TFSI]^-$, (c) EO_2, (d) EO_3, (e) EO_4, and (f) EO_5.Every atom labeled with a unique name. 30
Figure 3.2. Initial configuration of a simulation box containing 200 Li^+, 200 $[TFSI]^-$, 200 ZW molecules and 120 EO_5 molecules. (Li^+ ions are represented using the VDW model and the others are represented by the CPK model). This figure was generated using VMD-1.9.1[84] 32
Figure 3.3. Diffusion coefficients of (a) Li^+, (b) $[TFSI]^-$ and (c) EO_x in LiTFSI/EO_x/ZW and LiTFSI/EO_x (cases A and B)..... 33
Figure 3.4. Ratio of diffusion coefficients D/Do (with ZW/case-B-without ZW) of (a) Li^+, (b) $[TFSI]^-$, and (c) EO_x. 35

Figure 3.5. Diffusion coefficients of ZW molecules in LiTFSI/EO_x/ZW. 36
Figure 3.6. Peak height in radial distribution functions (RDFs) of (a) Li^+-O(EO_x, ter) and (b) Li^+-O(EO_x, mid) with and without ZW molecules. 37
Figure 3.7. Peak height in Li^+-O11($[TFSI]^-$) RDFs in the 12 electrolytes with and without ZW. 38
Figure 3.8. RDFs of (a) Li^+-O1(ZW), (b) H5(ZW)-O (EO_x, ter), (c) H5(ZW)-O (EO_x, mid) and (d) H5(ZW)-O11($[TFSI]^-$). 39
Figure 3.9. Association number of Li^+-O(EO_x), Li^+-O($[TFSI]^-$) and Li^+-O(ZW) and their sum. (a) case A without ZW, (b) case B without ZW and (c) electrolytes with ZW..... 41
Figure 3.10. Percentage of Li^+-EO_x association status with and without ZW molecules. (a) EO_2, (b) EO_3, (c) EO_4, and (d) EO_5. 43
Figure 3.11. Percentage of Li^+-$[TFSI]^-$ association status with and without ZW in (a) EO_2, (b) EO_3, (c) EO_4, and (d) EO_5. 44
Figure 3.12. Percentage of "single" and "double" status of Li^+-ZW associations. 45
Figure 3.13. Snapshot of Li^+ association in the electrolytes with and without ZW (a) EO_2, (b) EO_3, (c) EO_4, (d) EO_5. For each panel, the snapshots on the left are those from the electrolytes without ZW and the snapshots on the right are from the electrolytes with ZW. 46
Figure 3.14. Residence curve C(t) of all associations in (a) EO_2 without ZW (b) EO_2 with ZW, (c) EO_3 without ZW (d) EO_3 with ZW, (e) EO_4 without ZW (f) EO_4 with ZW, (g) EO_5 without ZW (h) EO_5 with ZW. 48
Figure 4.1. Molecular structures of (a) MPC, (b) SB, (c) CB, (d) $[TFSI]^-$, and (e) EO_{10}. Every atom is labeled with a unique name. Atom color code: hydrogen (silver), carbon (cyan), nitrogen (blue), oxygen (red), sulfur (yellow). 56
Figure 4.2. The initial configuration of a simulation box containing 100 Li^+, 100 $[TFSI]^-$, 20 SB molecules and 180 EO_{10} molecules. Li^+ ions are represented using the VDW model with purple color and the others are represented by the CPK model with the same color code in Figure 4.1. This figure was generated using VMD-1.9.1[84]..... 56
Figure 4.3. RDFs of (a) Li^+-O($[TFSI]^-$), (b) Li^+-O(EO_{10}), (c) Li^+-O(ZW) and (d) Li^+-Li^+ in case-A systems. 59
Figure 4.4. RDFs of (a) Li^+-O($[TFSI]^-$), (b) Li^+-O(EO_{10}), (c) Li^+-O(ZW) and (d) Li^+-Li^+ in case-B systems. 60
Figure 4.5. Percentage of Li^+ not coordinating with EO_{10}..... 64
Figure 4.6. Distribution of Li^+-O(ZW) coordination number in (a) case-A and (b) case-B systems. 65
Figure 4.7. Snapshot of (a) 4 MPC coordinating with 5 Li^+, (b) 2 CB coordinating with 3 Li^+, and (c) 1 SB coordinating with 3 Li^+ in case-A system. (Li^+ ions are represented using the VDW model with purple color; ZW molecules are displayed with the CPK model; $[TFSI]^-$ and EO_{10} molecules are displayed using the line model with the same color code in Figure 4.1). 66
Figure 4.8. Lifetime of Li^+-O coordination in case-A and case-B systems: (a) Li^+-O($[TFSI]^-$), (b) Li^+-O(EO_{10}), and (c) Li^+-O(ZW). 67

Figure 4.9. Diffusion coefficients of (a) Li^+, and (b) $[TFSI]^-$ at 600 K. Experimental values (Expt) of electrolytes comparable to case-A systems from the work of Panzer group at 293 K. [30] 69
Figure 4.10. Distance travelled by Li^+ ions in a specific O coordination number over 1-ns for systems (a) with MPC, (b) with CB, and (c) with SB in case-A systems. The bars in the figures show the standard deviation. 71
Figure 4.11. Radius of gyration (Rg) of EO_{10} chains in (a) case-A, and (b) case-B systems. 73
Figure 4.12. (a) Sigma profiles and (b) integral of H-bond acceptor region for three ZW structures 74
Figure 5.1. Ground state energy calculation flowchart using variational quantum eigensolver algorithm. 82
Figure 5.2. Molecular representations of (a) CO_2, (b) NH_3, (c) NH_2COOH initial state (IS: NH_3+CO_2), (d) NH_2COOH transitional state 1 (TS1), (e) NH_2COOH transitional state 2 (TS2), (f) NH_2COOH final state 1 (FS1), and (g) NH_2COOH final state 2 (FS2). Atom color code: hydrogen (silver), carbon (cyan), nitrogen (blue), and oxygen (red)... 86
Figure 5.3. Potential energy curve for addition reaction between CO_2 and NH_3 calculated by HF embedding, CCSD and HF.Atom colors: H: white, N: blue, C: gray, O: red..... 87
Figure 5.4. (a) Ground state vibrational energy and (b) accuracy convergence with number of iterations (eval count) for CO_2 molecule. E_{exact} values are obtained by diagonalization of the vibrational Hamiltonian. 88
Figure 5.5. (a) Ground state energy and (b) accuracy convergence with number of iterations (eval count) for NH_3 molecule. Reference values (E_{exact}) are obtained by diagonalization of the vibrational Hamiltonian. 89
Figure 5.6. Ground state energy convergence with number of iterations (eval count) for NH_2COOH molecule in its (a) initial state (IS), (b) transition state 1 (TS1), (c) transitional state 2 (TS2), (d) final state 1 (FS1), and (e) final state 2 (FS2). 90
Figure 5.7. Ground state energy convergence with number of iterations (eval count) for (a) CO_2 and (b) NH_3 molecules in the presence of simulated hardware noise and ZNE error-mitigation technique. 91

CHAPTER 1. INTRODUCTION

1.1 Introduction

Combating climate change requires sustainable energy solutions to reduce greenhouse gas emissions. The development of safe and efficient lithium-ion batteries, which have emerged as a critical technology for sustainable energy storage and usage, is one breakthrough in this subject[1–3]. Furthermore, CO_2 capture technologies are crucial for reducing CO_2 emissions to the atmosphere[4]. There have been ongoing efforts to improve the safety, efficiency, and scalability of lithium-ion batteries and CO_2 capture technologies, thereby easing the transition to a sustainable future.

Solid-state electrolytes have emerged as important components of safer lithium-ion batteries. These electrolytes have advantages over traditional liquid electrolytes, including enhanced stability, lower flammability, and higher energy density[5,6]. Implementing solid-state electrolytes in lieu of their volatile liquid counterparts can effectively mitigate the potential hazards of leakage and combustion, thereby enhancing the safety of battery systems[5,6]. Solid polymer electrolytes (SPEs) have become a promising category of solid-state materials in the field of battery technology due to their high safety standards, flexibility, and simplicity of processing[7–9]. These characteristics render SPEs desirable candidates for a variety of energy storage applications. However, a significant challenge associated with SPEs is their inherently low ionic conductivity[7,10–12].

Extensive research has been conducted to increase the ionic conductivity of SPEs. One approach involves incorporating various additives or fillers into the polymer matrix to facilitate ion transport. For instance, adding inorganic nanoparticles, such as ceramic materials or metal oxides, can create pathways for ion conduction and enhance the conductivity of the electrolyte[13,14]. Another strategy is adding plasticizers or liquid electrolyte components to the solid polymer matrix to enhance ion mobility[15,16]. In addition, there has been increased interest in the design and synthesis of novel polymer

architectures with enhanced ion transport properties. Using copolymers or block copolymers, for example, it is possible to incorporate segments with greater ion mobility into the polymer matrix, thereby accelerating ion diffusion[17,18]. Furthermore, the incorporation of functional groups that facilitate ionic solvation can increase the electrolyte's overall conductivity[19,20].

Zwitterionic (ZW) materials are promising candidates for improving performance of SPEs due to unique structures and properties. ZW molecules are characterized by having both positive and negative charges within the same molecule[21–23]. The presence of oppositely charged groups on ZW facilitates the formation of ion-dipole interactions, leading to enhanced solvation of ions[24–26]. This improved solvation promotes the dissociation of ions from the polymer backbone, allowing for faster ion mobility, and higher ionic conductivity compared to conventional polymer electrolytes[27–31]. Additionally, ZW materials exhibit high mechanical strength and stability, making them suitable for battery applications[32,33].

Despite the promising potential of ZW materials in improving the performance of polymer electrolytes, several challenges still need to be addressed. One of the main obstacles is the lack of a comprehensive understanding of the underlying mechanisms and design principles of zwitterionic electrolytes. The intricate interplay between ZW-regulated ionic solvation and transport behavior is not yet fully elucidated.

If we can better understand the mechanisms behind the ZW effect, we can harness the ability of ZW molecules to improve ionic transport in solid polymer electrolytes. The transport of ions largely depends on the interactions between them and polymer chains[34–37]. Since zwitterionic molecules can interact with both anions and cations, different zwitterionic structures can influence the ion-ion associations and, consequently, ionic transport in electrolytes[30,31]. Various parameters need to be considered in the design of zwitterionic materials, including cationic and anionic groups, the inclusion of nonpolar groups, and the specific electrolytic environment, which depends on the types of ions, and

polymer. By carefully manipulating these parameters, we can optimize the design of zwitterionic materials for improved performance in polymer electrolytes.

This study employs molecular dynamics simulations to gain insights into the behavior of ZW materials at the atomic scale. This work will answer several fundamental questions about the mechanism behind the ZW effect. First, how do ZW molecules affect ionic solvation and transport of lithium ions in polymer ethylene oxide electrolytes? Second, what is the correlation between the effect of ZW molecules and their chemical structures? The investigation provides valuable information on the dynamics of ionic diffusion, solvation behavior, and interactions with the polymer chains, aiding in developing strategies to improve the performance of ZW-based electrolytes. Understanding ZW materials and their mechanisms will enable the rational design and synthesis of novel ZW electrolytes tailored for specific battery applications, leading to the development of safer, more efficient energy storage systems for a sustainable future.

Simultaneously, investigating chemisorption reactions is crucial for optimizing CO_2 capture and conversion processes[38]. The study of CO_2 capture reactions requires a comprehensive understanding of the electronic and vibrational energies involved in the reaction pathways. Traditional computational methods, such as density functional theory (DFT) or coupled cluster theory, have been used to calculate the electronic and vibrational properties. However, these methods have limitations when determining vibrational structures, particularly for larger molecules, due to the anharmonicity effect[39].

Quantum computing has the potential to provide more accurate and fast molecular property calculations[40,41]. Quantum algorithms, such as the variational quantum eigensolver (VQE) algorithm[42], have been developed to address classically challenging problems such as the anharmonicity effect in large molecules. The VQE algorithm employs a variational approach to find the lowest energy state of a molecular system by utilizing a parameterized quantum circuit and optimizing the parameters iteratively[42,43]. This

algorithm has successfully calculated molecular properties, including electronic and vibrational energies[44–47].

This study applied VQE algorithm to investigate the reaction pathways between CO_2 and NH_3 for CO_2 capture. In addition, the study sought to showcase the capabilities of quantum computing in calculating the vibrational energies for the CO_2 capture reaction. This study highlights the potential of quantum computing in enhancing the simulation of CO_2 capture reactions. By providing accurate vibrational energy calculations for large molecules, quantum computing offers a valuable tool for studying and optimizing the capture of CO_2. This work contributes to the growing body of research demonstrating the applications of quantum computing in chemical simulations, showcasing its potential for tackling complex molecular systems and accelerating the development of sustainable technologies.

The dissertation content is as follows: Chapter 2 describes the ZW effect in lithium salt electrolytes under an electric field. Chapter 3 shows the ZW effect on ethylene oxide-based electrolytes. Chapter 4 illustrates the distinct effect of three ZW structures on ionic solvation of lithium ions in ethylene oxide-based electrolytes. Chapter 5 showcases the application of quantum computing to describe the reaction and vibrational energetics of CO_2-NH_3 interaction. Chapter 6 summarizes the research reported in Chapter 2-5 with a perspective on the future direction. Figure 1.1 shows the structure of this dissertation.

1	• Introduction
2	• Effect of zwitterionic molecules on ionic transport under electric fields
3	• Zwitterionic effects on ionic association in ethylene oxide-based electrolytes
4	• Distinct effect of zwitterionic molecules on ionic solvation in $(\text{ethylene oxide})_{10}$
5	• Description of reaction and vibrational energetics of CO_2-NH_3 interaction using quantum computing algorithms
6	• Conclusions and perspective

Figure 1.1. Organizational overview of the dissertation

CHAPTER 2. EFFECT OF ZWITTERIONIC MOLECULES ON IONIC TRANSPORT UNDER ELECTRIC FIELDS

2.1 Introduction

The design of high-performance Li^+ batteries plays a critical role in realizing the sustainable development of the society[1,48–51]. One task is to develop safe electrolytes with high ionic conductivity. Various materials have been explored for this purpose, ranging from ionic liquids[52] to polyethylene glycol[53]. Zwitterionic (ZW) molecules recently emerged as candidates for this purpose due to their unique structures[27,28,54–57]. ZW molecules possess both cationic and anionic groups[21,23,58]. They can associate with both Li^+ and anions, and even among themselves[24–26,59,60]. This ability can be used to adjust ionic associations, paving a new avenue to develop electrolytes with high ionic conductivity. However, despite encouraging experimental observations, little is known about the mechanisms by which ZW molecules affect the molecular properties of the electrolytes. We must understand these mechanisms to develop high-performance electrolytes based on ZW molecules.

One question is how zwitterionic molecules affect the ionic associations and transport in the electrolytes. The Li^+ and anions associate in electrolytes due to the electrostatic attractions and these ionic associations play an important role in their distribution and transport. As stated above, ZW molecules can associate with both Li^+ and anions at the same time. This ability may impact the diffusion of Li^+ and anions in electrolytes. If this hypothesis is right, we could manipulate the ionic transport in electrolytes by selecting ZW molecules with suitable structures. This chapter aims to investigate the effect of ZW molecules on ionic associations and explore the underlying mechanisms.

Several experiments show the promising role of ZW molecules in electrochemical applications. As early as 2001, Yoshizawa et al.[61] prepared ZW materials containing

imidazolium and sulfonate or sulfonamide groups. They found that the ionic conductivity of ZW polymers could be 10^{-5} S·cm^{-1}. Ohno et al.[54] also investigated electrolyte gels with the same ZW motifs and got similar results. Their experiments also showed the high thermal stability of the ZW materials. More recently, the Panzer group[27,28,62] reported polymers containing ZW sulfobetaine vinylimidazole and phosphorylcholine with ionic conductivity around 10^{-3} S·cm^{-1}. Their research also shows the high mechanical strength of these ZW materials. These studies imply that ZW materials can be developed into electrolytes with high ionic conductivity if we understand the related mechanisms.

The potential of ZW materials to possess great electrochemical properties are also suggested by some research that mixes them with other types of molecules. For instance, Byrne et al.[63,64] showed that the electrolytes containing *N*-methyl-*N*-propylpyrrolidiniumbis(trifluoro-methanesulfonyl)-amide (P_{13}TFSA) and ZW motifs had an ionic conductivity five times of that for electrolytes just containing P_{13}TFSA. Tiyapiboonchaiya et al.[55] showed that adding ZW motifs enhanced ionic conductivity of polyelectrolyte gels by seven times. Yamaguchi et al.[65,66] showed that the cycle stability of electrolytes containing poly(ethylene glycol)dimethyl ether and ZW motifs was higher than those only with PEGDME. Some research groups have also investigated the applications of ZW materials in capacitors[67,68] and fuel cells[69–71].

Some research shows the ability of ZW molecules to adjust ionic associations and transport in electrolytes. The simulations of Shao et al.[24] showed that the ZW molecules could associate strongly with Li^+. Such a strong association may be leveraged to dissociate ionic associations between Li^+ and anions. Their simulations[26] also showed that the associations among ZW molecules relied on the types of anionic and cationic groups. Narita et al.[72] showed that long alkyl-chain length in an ammonium cation structure resulted in low ionic density and conductivity. Their experiments also showed that the ionic conductivity of methylpyrolidinio cation type was lower than that of imidazole cation type. Their FT-IR spectra also showed that Li^+ and $TFSI^-$ were not fully dissociated in mixtures

with ZW molecules of one carbon spacer. Yoshizawa et al.[73] found that the type of Li salts affected the glass transition temperature and ionic conductivity of electrolytes. They examined the properties of mixtures containing the same type of ZW molecules and five types of Li salts (LiTFSI, LiBETI, $LiBF_4$, $LiCF_3SO_3$, and $LiClO_4$). The mixture with LiTFSI possesses the lowest glass transition temperature (-37 °C) and highest ionic conductivity (8.9×10^{-4} $S\cdot cm^{-1}$ at 100 °C).

An external electric field will be deployed in this research to help understand the effect of ZW molecules on ionic associations and transport. External electric fields have been used as an effective tool to investigate the behavior of molecules in solutions. The electric field can be used to adjust the orientation of molecules or dissociate ionic associations. The cations and anions may diffuse differently under the same electric field due to the difference in their masses and charged densities. However, ZW molecules may change this scenario due to their ability to associate with cations and anions.

The behavior of molecules under external electric field has been extensively investigated in traditional molecular dynamics simulations. Several reviews[74,75] have summarized these efforts. He et al.[76] investigated ionic hydration under an electric field using molecular dynamics simulations. They found that the electric field had to be strong enough to disturb the orientation of the water molecules in the solvation shells of ions. Their research also indicates the difference in the effects of electric fields on the solvation of cations and anions. Zhao et al.[77] investigated the effect of electric field on the structure of $[C_2MIM][BF_4]$ using molecular dynamic simulations. They also found that the electric field strength had to be higher than a threshold to dissociate the hydrogen bonding network in the ionic liquids. Ren et al.[78] investigated the structural and dynamic properties of NaCl solution under electric field using molecular dynamics simulations. They found that Na^+ and Cl^- ions diffused at different rates under the same electric field. They attribute this difference to the asymmetric feature of water molecules in the hydration shells. Kerisit et al.[79] also investigated the solvation structure and transport of alkali cations in dimethyl

sulfoxide solvent under electric field using molecular dynamics simulations. They found that the electric field only affected solvation of cations when larger than a threshold and the threshold value was related to the charge density of cations.

The objective of this chapter is to investigate the effects of ZW molecules on ionic associations and transport in electrolytes under electric fields. We will focus on seeking answers to two questions. First, how does the presence of zwitterionic molecules change the association environment of Li^+ in electrolytes? Second, how do these changes affect ionic transport in electrolytes? This work will use ZW molecules with cationic imidazolium, anionic sulfonate group with a carbon spacer of two or three methylene groups as the main model (Figures 2.1a and 2.1b). Two types of Li salts will be used: LiTFSI and LiBETI (bis (trifluoromethanesulfonyl) imide ($[TFSI]^-$) and bis(perfluoroethylsulfonyl)imide ($[BETI]^-$)). The electric field ranges from 0 to 1.1 V/nm in most of the research. Some research[80–82] indicates that scaling partial charges plays an important role in investigating organic electrolytes containing ionic liquid-like compounds. The ZW molecules in this work possess structures similar to ionic liquids, and the anions belong to ionic liquids. We will investigate if scaling partial charges impacts the major conclusion of this work. The rest of the chapter is organized as follows: section 2.2 presents molecular models and simulation details, section 2.3 presents the results and discussion, and section 2.4 presents a conclusion.

2.2 Molecular model and simulation detail

2.2.1 Molecular model

This work applies all-atom models to represent ZW molecules and anions. Figure 2.1shows the structures of ZW molecules (Z2C and Z3C) and anions used in this work. A Li^+ ion is described using a single sphere. The simulation box was created by randomly placing 200 ZW molecules, 200 selected anions and 200 Li^+ ions in a cubic box with an

initial length of 6.0 nm. This process was conducted using Packmol[83]. Figure 2.2 shows the initial configuration of a simulation box containing 200 Li^+, 200 $[TFSI]^-$, and 200 Z2C molecules.

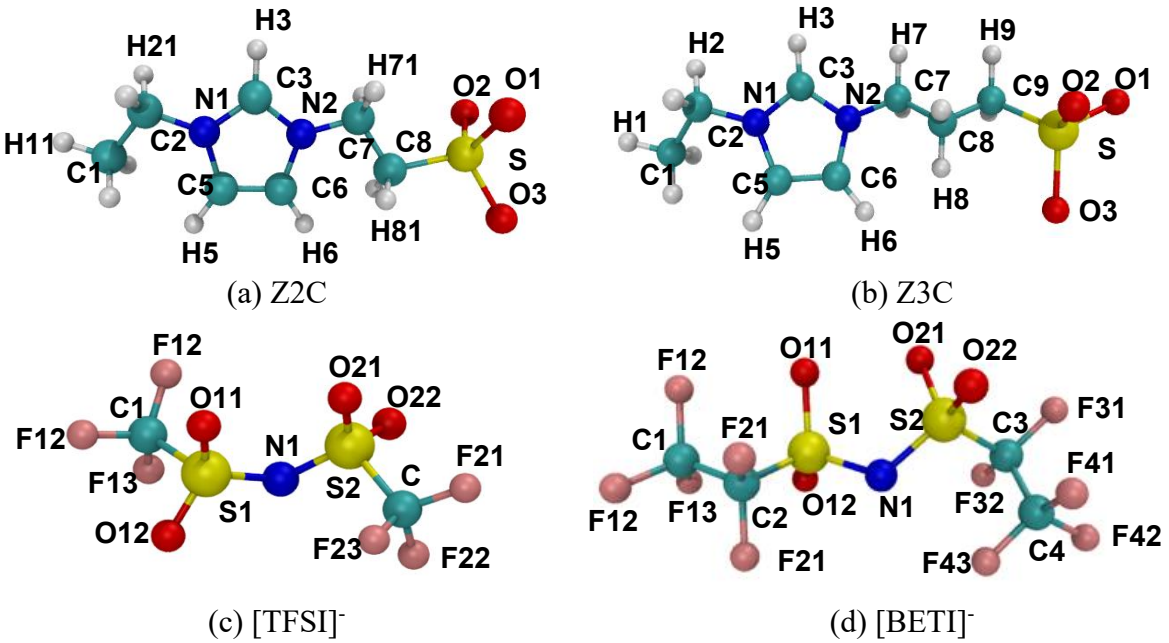

Figure 2.1. Molecular structures of zwitterionic molecules and anions in this work. (a) Z2C, (b) Z3C, (c) $[TFSI]^-$ and (d) $[BETI]^-$. Every atom is labeled using a unique name.

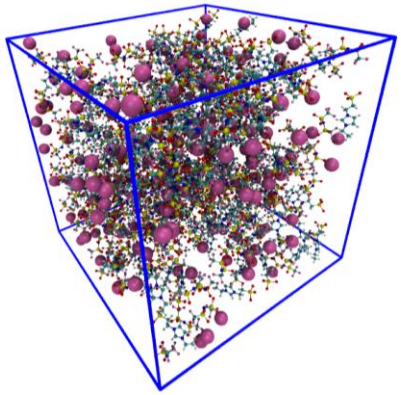

Figure 2.2. Initial configuration of a simulation box containing 200 Li^+, 200 $[TFSI]^-$, and 200 Z2C molecules (Li^+ ions are represented using the VDW model and the others are represented by the CPK model). This figure was generated using VMD-1.9.1[84].

$$E = \sum_{i}\sum_{j<i}\left\{\frac{1}{4\pi\varepsilon_0}\frac{q_i q_j e^2}{r_{ij}} + 4\varepsilon_{ij}\left[\left(\frac{\sigma_{ij}}{r_{ij}}\right)^{12} - \left(\frac{\sigma_{ij}}{r_{ij}}\right)^{6}\right]\right\} \qquad (2.1)$$

The non-bonded interactions among Li^+, anions and zwitterionic molecules are described using a sum of the short-range Lennard-Jones 12-6 potential and long-range Coulomb potential (Equation 2.1). The ZW molecules used in this work are structurally similar to ionic liquids and the anions belong to the ionic liquid category. Thus, the non-bonded force field parameters are derived from the OPLS-AA ionic liquid force field[85,86] and our previous research of ZW molecules[26,60,87]. Table A1 lists the non-bonded force field parameters for molecules and ions in this work. The bonded potential is described as a sum of bond, angle and dihedral-angle potentials. These parameters are derived from the OPLS-AA force field[86]. An electric field is applied to the system by adding corresponding forces upon atoms based on their partial charges.

The ionic liquid force field used in this research was initially developed based on scaled partial charges with a factor of 0.8. Thus, the net charge of anions is -0.8. We decide to scale all the partial charges of other ions by a factor of 0.8 so the system can have the same number of cations and anions while having zero charge overall. The simulation results with this set of partial charges will be labeled as "scaled charge". The impact of scale-charges on simulation results will be investigated by timing the scaled charges again by a factor of 1.25. The simulation results with this set of partial charges will be labeled as "full charge".

2.2.2 Simulation detail

Three steps of simulations were carried out for each system. The first step is an energy minimization that lets the system reach a configuration. This configuration will be

used to start molecular dynamics (MD) simulations. This step should eliminate any too-close contact between atoms. The second step is a 100-ns isothermal-isobaric (NPT) MD simulation using a 2-fs integral step. The second step ensures that the system reaches a thermodynamic equilibrium. The Berendsen algorithm[88] was used to control the temperature at 300 K and the pressure at 100 kPa in this step because it can let the system reach the targeted temperature and pressure fast. The third step is a 1000-ns canonical (NVT) MD simulation using a 2-fs integral step to collect the trajectory every 10 ps. The velocity-rescaling method[89] was used to control the temperature at 300 K. A 1.0-nm cut-off was applied to the short-range potential, and the particle mesh Ewald sum[90] was applied to calculate the long-range potential. All bonds involving hydrogen atoms were constrained using the LINCS algorithm[91]. Gromacs-2019[92] was used to conduct all energy minimization and MD simulations.

2.3 Results and discussion

2.3.1 Diffusion coefficients of Li^+, anions and Z2C molecules

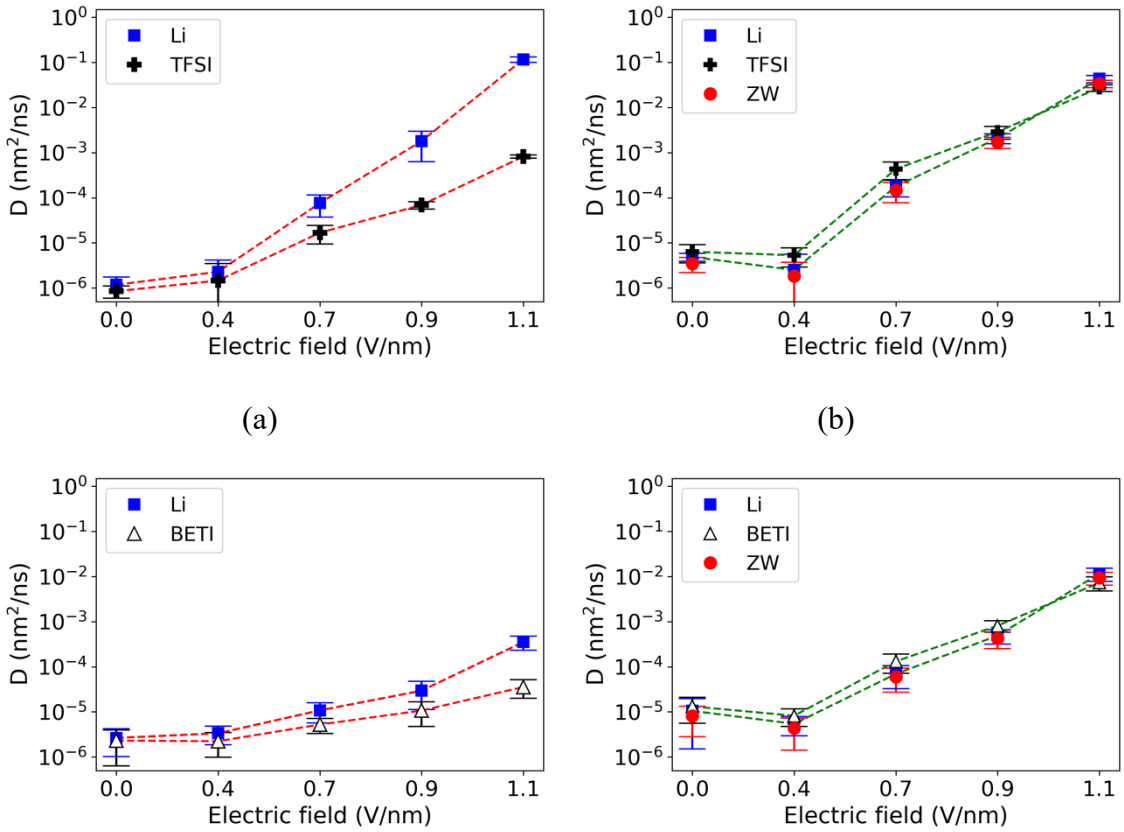

Figure 2.3. Diffusion coefficients (D) of Z2C molecules and ions in the z direction (the direction of the electric field) as a function of electric field strength (scaled charge) (a) LiTFSI, (b) Z2C/LiTFSI, (c) LiBETI and (d) Z2C/LiBETI.

Figure 2.3 shows the diffusion coefficients (D) of Li^+, anions and Z2C molecules in the LiTFSI, LiBETI, Z2C/LiTFSI and Z2C/LiBETI systems in the z direction (the direction of the electric field) under electric fields ranging from 0-1.1 V/nm. The LiTFSI and LiBETI systems are only used as a reference to investigate how ZW molecules may affect ionic diffusion. They should be solid and those with ZW molecules should be molten salt[20] at 300K. The Einstein expression $D = \lim_{t \to 0} \frac{\langle x(t+t_0) - x(t_0) \rangle}{2t}$ has been widely used to calculate D that can characterize the diffusion of ions and molecules under electric fields[74–

[76]. Indeed, the Einstein expression was developed based on the systems without an external field, and arguments remain how well it can be used to describe the diffusion of substances under an external field. However, the diffusion coefficients calculated by the Einstein expression can be used to characterize the diffusion ability of ions and molecules in the system. Here we calculate D of Z2C molecules and ions using the Einstein expression based on the mean square displacement (MSD) curves of four 250-ns blocks from the 1000 ns MD simulations. The diffusion coefficients in the other two directions are shown in Figure A.1.

The Z2C molecules attenuate the distinct effects of electric fields on the diffusion of Li^+ and anions. As shown in Figure 2.3a, D_{Li+} and $D_{[TFSI]^-}$ increase and their difference expands as the electric field strength increases in the system without Z2C molecules. The different effects of electric fields on D_{Li+} and $D_{[TFSI]^-}$ are expected because they receive the same forces from the electric field but possess different masses. The difference increases with electric field strength. However, Z2C molecules alter this trend. As shown in Figure 2.3b, D_{Li+}, $D_{[TFSI]^-}$ and D_{Z2C} still increase with electric field strength, but they are very similar.

The Z2C/LiBETI system presents the similar phenomenon. Figures 2.3c and 2.3d show the diffusion coefficients D of the Z2C molecules and ions in the LiBETI and Z2C/LiBETI systems under electric field from 0 to 1.1 V/nm. The diffusion coefficients of Li^+ and $[BETI]^-$ show increasing differences as the electric field strength enhances without Z2C molecules (Figure 2.3c), while they are similar under the electric fields from 0 to 1.1 V/nm with the presence of Z2C molecules (Figure 2.3d). Thus, it may be a general trend for ZW molecules to attenuate the differences between the diffusion of Li^+ and anions caused by the electric fields. We will explore the origin of this effect from ionic associations in the next section.

Figure 2.3 also shows that the electric field strength must be stronger than a threshold to increase the diffusion of molecules and ions in the electrolytes significantly.

As shown in Figure 2.3b, increasing the electric field from 0 to 0.4 V/nm does not result in any significant change in the diffusion coefficients of Li^+, $[TFSI]^-$ and Z2C molecules. But increasing the electric field further to 0.7 V/nm results in a 10-time increase of the diffusion coefficients. Similar electric field thresholds have been reported regarding their ability to change the structure and dynamics of ionic solvation[76]. The influence of electric field on the diffusion coefficients of ions and Z2C molecules may relate to its ability to adjust their associations.

2.3.2 Structure of association among Li^+, anions, and Z2C molecules

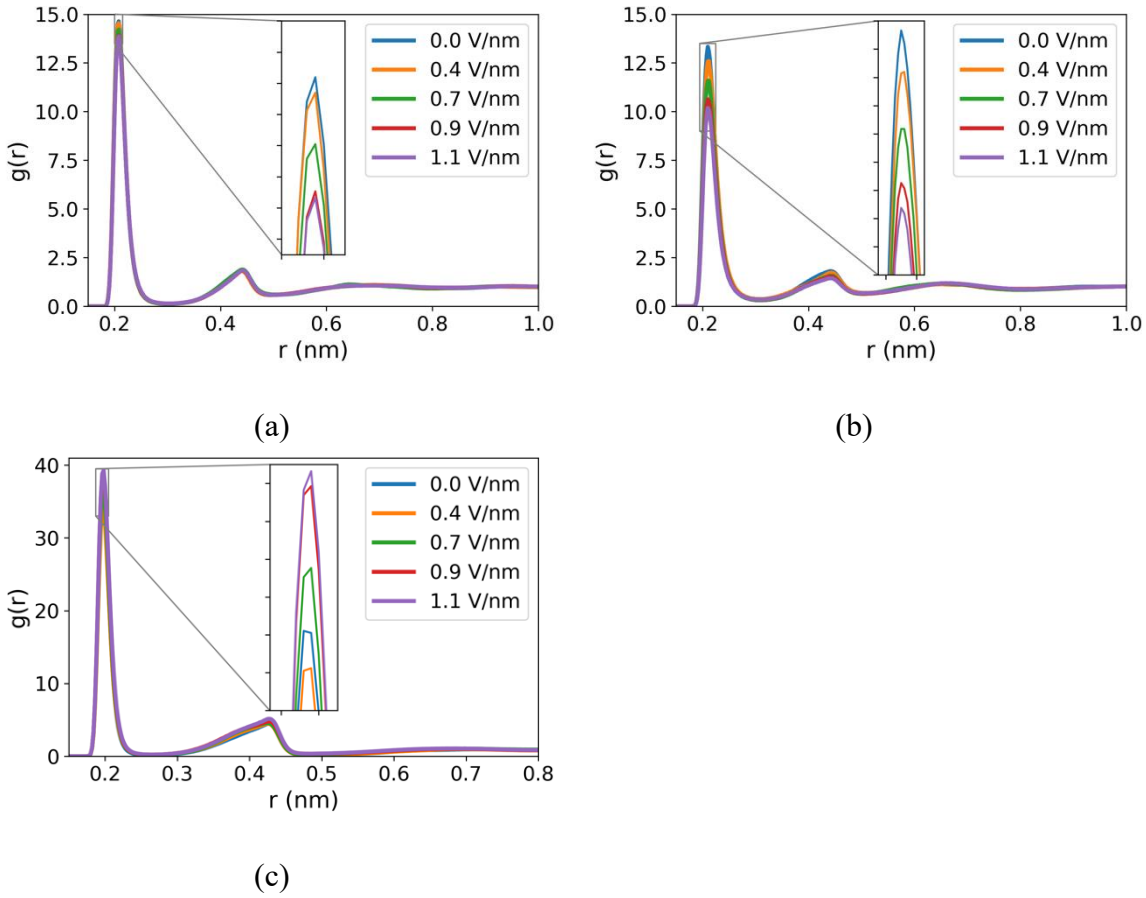

Figure 2.4. Radial distribution functions (RDFs) in the electrolyte solutions (scaled charge). (a) Li^+-O11$[TSFI]^-$ in LiTFSI solution and (b) Li^+-O11$[TFSI]^-$ and (c) Li^+-O1(ZW) in Z2C/LiTFSI solution. The O11 of $[TFSI]^-$ and O1 of Z2C were shown in Figure 2.1

Z2C molecules dissociate Li^+-$[TFSI]^-$ associations. Figures 2.4a and 2.4b show the Li^+-O11($[TFSI]^-$) radial distribution functions (RDFs) in the systems without and with Z2C molecules under 0-1.1 V/nm electric field. All RDFs show a high peak around 0.2 nm, consistent with the Li^+-O RDFs founded in other simulations[24]. The high peaks indicate that Li^+ associates with $[TFSI]^-$ strongly in the LiTFSI and Z2C/LiTFSI systems. However, the RDF peaks in Figure 2.4b are lower than those in Figure 2.4a with the same electric field. For instance, the RDF peak heights are 14 and 10 in the LiTFSI and Z2C/LiTFSI systems with a 1.1 V/nm electric field. The lower peak height indicates that the ZW molecules decrease the number of Li^+-$[TFSI]^-$ associations.

The decrease of Li^+-$[TFSI]^-$ RDF peak height may be due to the dissociation ability of ZW molecules. Figure 2.4c shows the Li^+-O1(ZW) RDFs in the Z2C/LiTFSI solution under 0-1.1 V/nm electric fields. All RDFs show a high peak around 0.22 nm. This high peak indicates that Li^+ also associates strongly with ZW molecules through their sulfonate groups, consistent with the previous research. The ZW molecules then compete with [TFSI]- to associate with Li^+. Such competition would dissociate ionic associations and affect the Li^+ solation and transport in the electrolytes.

Increasing electric field strength dissociates Li^+-$[TFSI]^-$ pairs and promote Li^+-ZW associations. As shown in Figure 2.4b, the peak height of Li^+-$[TFSI]^-$ RDF decreases as the electric field increases. This is expected because an electric field tends to dissociate ionic associations. However, as shown in Figure 2.4c, the peak height of Li^+-O(ZW) RDF increases with the electric field. For instance, the peak height is 32 at 0 V/nm and shifts to around 40 at 1.1 V/nm. This shift of Li^+-O(ZW) RDF may be due to two reasons. First, the ZW molecules are neutrality in charge, making them less influenced by an electric field. Second, increasing the electric field dissociates more Li^+-$[TFSI]^-$ associations and thus makes more Li^+ ions available for Li^+-ZW associations.

The large dipole moment may also contribute to the Li^+-ZW associations and their variation under the electric field. ZW molecules usually have a dipole moment much

stronger than the others. The dipole moment of a Z2C molecule is 20±2.5 D, while those of $[TFSI]^-$ and $[BETI]^-$ are 3.2±1 and 4.7±1.4 D, respectively. The electric field strengths needed to dissociate the Li^+-Z2C association may be much stronger than that to dissociate the Li^+-$[TFSI]^-$ or Li^+-$[BETI]^-$ association.

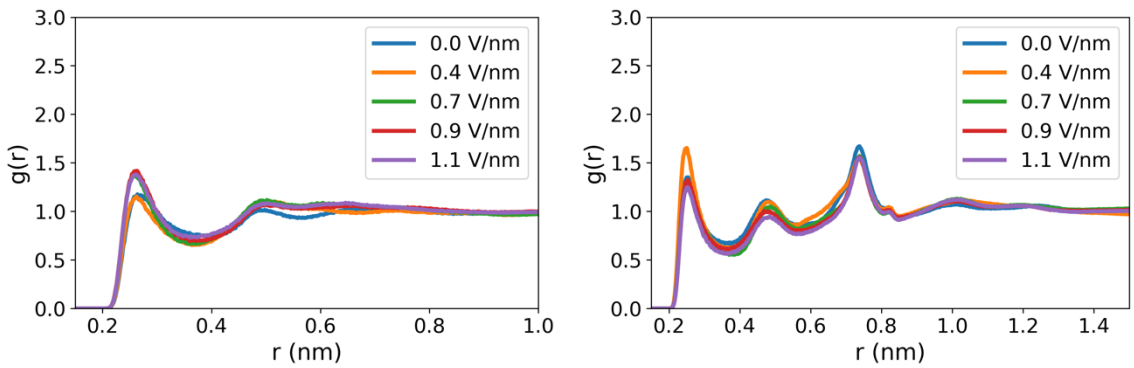

(a) (b)

Figure 2.5. (a) Z2C-$[TFSI]^-$ and (b) Z2C-Z2C radial distribution functions (scaled charge)

Z2C molecules associate with $[TFSI]^-$ but these associations are weaker than those with Li^+. Figure 2.5a shows the RDFs between N1 atoms on Z2C molecules and O11 atoms on $[TFSI]^-$. These RDFs present a peak with a height of 1.2-1.5 around 0.25 nm under 0-1.1 V/nm electric field. These low peaks indicate that Z2C molecules could associate with $[TFSI]^-$, but the associations are not as strong and many as those involving Li^+. The relatively large volumes of imidazolium groups and $[TFSI]^-$ anions may play a role in decreasing and weakening their associations. However, it does not exclude the importance of these Z2C-$[TFSI]^-$ associations. They could serve as bridges for anions to connect to Li^+ indirectly since ZW molecules also associate with Li^+ strongly.

ZW molecules could associate among themselves weakly. Figure 2.5b shows the RDFs between N and O atoms on Z2C molecules. The two peaks are due to the two N atoms on imidazolium groups. Figure 2.5b shows that the peak heights are around 1.2-1.5. These low peaks indicate the weak associations among ZW molecules themselves. The traditional theory assumes that ZW molecules should associate with themselves. However,

recent research[26] has shown that the association among ZW molecules is not granted. They are determined by the types of charged groups and their solvation environment. The weak association among ZW molecules could disrupt the association environment of Li^+ and thus change their transportations instead of just compensating among themselves.

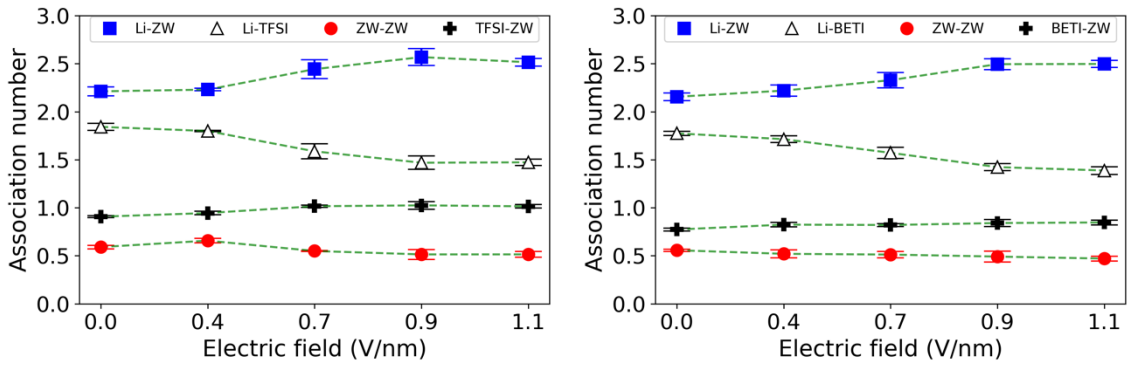

(a) (b)

Figure 2.6. Number of molecular and ionic associations in (a) Z2C/LiTFSI and (b) Z2C/LiBETI solutions (scaled charge).

The numbers of association among Li^+, anions and Z2C molecules correlate well with their diffusion coefficients. Figure 2.6a shows the average numbers of Li^+-Z2C association (N_{Li+-ZW}), and Li^+-$[TFSI]^-$ association ($N_{Li+-TFSI}$) as a function of electric field strength. A Li^+-Z2C association forms when the distance between the Li^+ ion and any oxygen atom on the Z2C molecule is less than 0.25 nm. A Li^+-$[TFSI]^-$ association forms if the distance between the Li^+ ion and any oxygen atom on the $[TFSI]^-$ ion is less than 0.3 nm. These two distance cutoffs are the minimal positions on the Li^+-O1(ZW) and Li^+-O1$[TFSI]^-$ RDFs. As shown in Figure 2.6, $N_{Li+-TFSI}$ and N_{Li+-ZW} change little when the electric field varies from 0 to 0.4 V/nm. The diffusion coefficients of Li^+, $[TFSI]^-$ and Z2C molecules also change little in this range. The value of $N_{Li+-TFSI}$ starts to decrease while N_{Li+-ZW} starts to increase when the electric field change from 0.4 to 0.7 V/nm. The diffusion coefficients of the three compounds also start to change at this point, as shown in Figure 2.3b.

The Z2C/LiBETI system presents a similar phenomenon. As shown in Figure 2.6b, the Li^+-$[BETI]^-$ and Li^+-ZW association numbers ($N_{Li+-BETI}$ and N_{Li+-ZW}) change gradually as a function of the electric field. The corresponding diffusion coefficients present the same trend (Figures 2.3c and 2.3d). Such a match in electric field thresholds indicates a possible role of Li^+ solvation environment in its transport. We will analyze this match and the mechanisms behind it further in the next section.

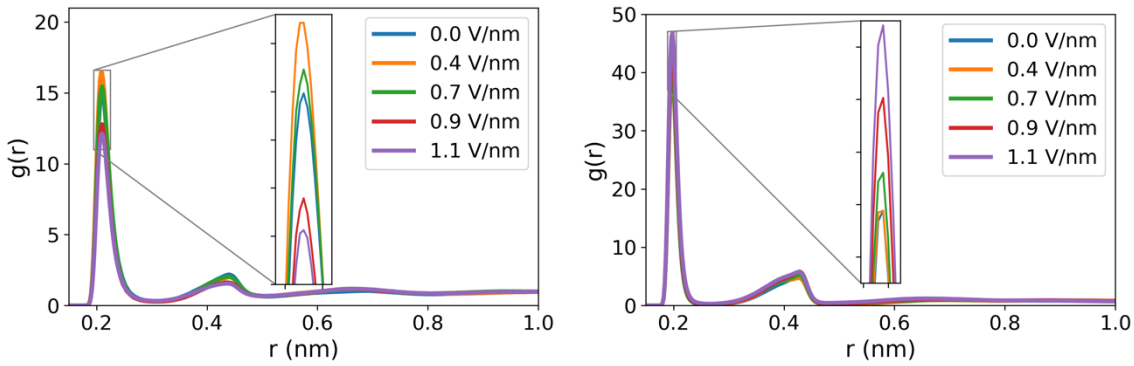

(a) (b)

Figure 2.7. Radial distribution functions in electrolyte solutions. (a) Li^+-O11$[BETI]^-$ and (b) Li^+-O1(ZW) in Z2C/LiBETI solution (scaled charge).

Differences are present between the Z2C/LiBETI and Z2C/LiTFSI systems. Figure 2.7 shows the Li^+-O11$[BETI]^-$ and Li^+-O1(ZW) RDFs in Z2C/LiBETI electrolytes. The peak height of the Li^+-O1(ZW) RDF can be higher than 40 in Z2C/BETI electrolytes while it is less than 40 in Z2C/LiTFSI electrolytes (Figure 2.4c). The higher peak indicates that Z2C may associate with more Li^+ ions more strongly with LiBETI. Such difference also indicates that the anion type in Li salt should play a role in the effect of ZW molecules on ionic associations. A competition of associations among Li^+, anions and ZWs may exist and the roles of anions and ZW molecules in this competition may rely on the charge strength of the related charged groups. Based on the force field used in this work (Table A.1), the charge strength of the anionic group of a Z2C molecule is stronger than those of

[BETI]$^-$ and [TFSI]$^-$. The stronger charge strength may lead to higher peaks of Li^+-O1(ZW) RDFs.

2.3.3 Association residence time

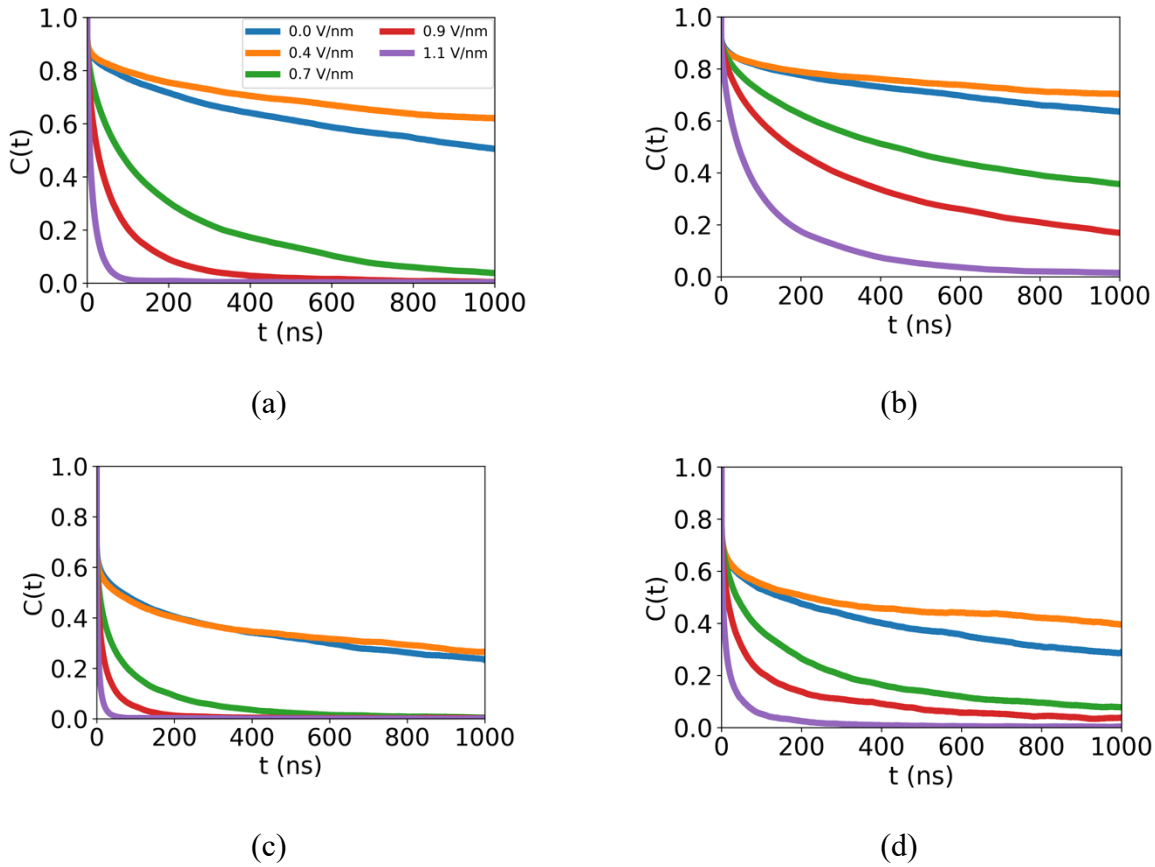

Figure 2.8. Residence curves C(t) for associations in Z2C/LiTFSI systems (scaled charge). (a) Li^+ and [TFSI]$^-$, (b) Li^+ and ZW, (c) ZW and [TFSI]$^-$; (d) ZW and ZW

Electric fields also affect the dynamics of molecular and ionic associations in the electrolytes. Figure 2.8 shows the residence curves C(t) for Li^+-[TFSI]$^-$, Li^+-ZW, ZW-[TFSI]$^-$ and ZW-ZW associations in the Z2C/LiTFSI solution under 0-1.1 V/nm electric fields. The value of C(t) is calculated based on $C(t) = \frac{1}{N_0}\sum_{j=0}^{N_0}\frac{\langle P_j(0)P_j(t)\rangle}{\langle P_j(0)\rangle^2}$ where N_0 is the total number of certain associations at t=0, $P_j(0) = 1$, and $P_j(t)$ =1 if the association j still exist at t and $P_j(t)$ =0 if the associate j breaks at t. It does not matter if an association breaks or not during the period.

The electric field also presents a threshold at 0.7 V/nm regarding its ability to change the decay rate of C(t) for the Z2C/LiTFSI system. As shown in Figure 2.8, all the four associations have their C(t) curves decaying faster as the electric field increases. This effect enhances significantly when the electric field reaches 0.7 V/nm. Taking the Li^+-$[TFSI]^-$ association in Figure 2.8a for example, around 25% of the associations break after 400 ns without an electric field. The broken association percentage becomes ~32% when the electric field increases to 0.4 V/nm, increasing by only 28%. However, the broken association percentage is 80% when the electric field is 0.7 V/nm, increasing by 220%. The other three associations present a similar trend.

Based on the simulation observations above, we propose a possible scenario that connects diffusion and associations in the electrolytes. In principle, molecular and ionic associations help attenuate the difference in their diffusion abilities. External electric fields dissociate these associations; therefore, the molecules and ions are more likely to behave as individuals instead of associated entities. This is probably why the difference in the diffusion of Li^+ and anions expands as the electric field increases.

The above scenario suggests a possible role of ZW molecules in the electrolytes: providing extra associations. ZW molecules associate with more Li^+ as the electric field increases, thus deducting the number of unassociated Li^+ ions in the systems. The ZW-anion and ZW-ZW associations also provide extra associations among molecules and ions in the systems, even though they are relatively weak. In addition, ZW molecules could associate with both Li^+ and anions, providing an indirect connection for them even under a high electric field. These extra ZW-enabled associations may be the reason why the electrolyte compounds diffuse at the same level, even at a high electric field.

2.3.4 Effect of scaled charges on association and diffusion in the electrolytes

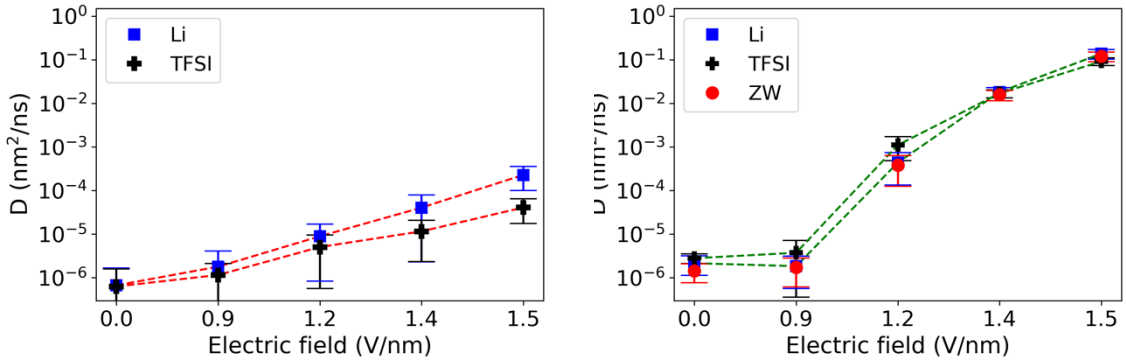

(a) (b)

Figure 2.9. Diffusion coefficients of Li^+, $[TFSI]^-$ and zwitterionic Z2C in the z direction as a function of electric field (full charge) (a) LiTFSI and (b) Z2C/LiTFSI

This section investigates how scaling charges may affect the simulation results. The results above are based on the simulations using the scaled charges reported in the original force field. They scaled partial charges so the net charge of a monovalent ion is ±0.8. Indeed, scaled charges have been a practical method to investigate the molecular properties of nonaqueous solutions such as ionic liquids and deep eutectic solvents[80–82]. ZW-based electrolytes in this work belong to the category of organic electrolytes. However, research also presents the limitation of scaled charges and the fundamental roots of scaling charges may remain unclear[93–96]. Thus, we decide to scale the partial charges back (the net charge of an ion is ±1) and investigate how this change in partial charges may affect the results.

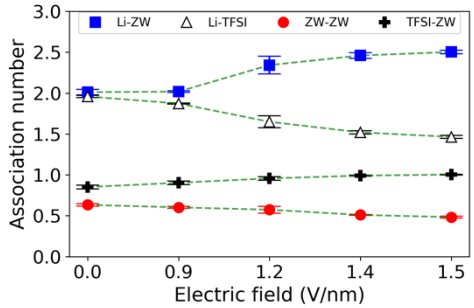

Figure 2.10. Association numbers in Z2C/LiTFSI electrolytes as a function of the electric field (full charge)

Scaled charges do not qualitatively change the effects of ZW molecules on ionic transport and molecule and ionic associations under an electric field. Figure 2.9 shows the diffusion coefficients of Li^+, $[TFSI]^-$ and Z2C molecules in LiTFSI and Z2C/LiTFSI with full charges. Two features are still present: (1) Li^+ and $[TFSI]^-$ diffuse at similar rates with the presence of Z2C molecules, and (2) the electric field presents a threshold regarding its ability to accelerate ionic transport. The Li^+-ZW association number in Figure 2.10 also presents an increase after an electric field threshold.

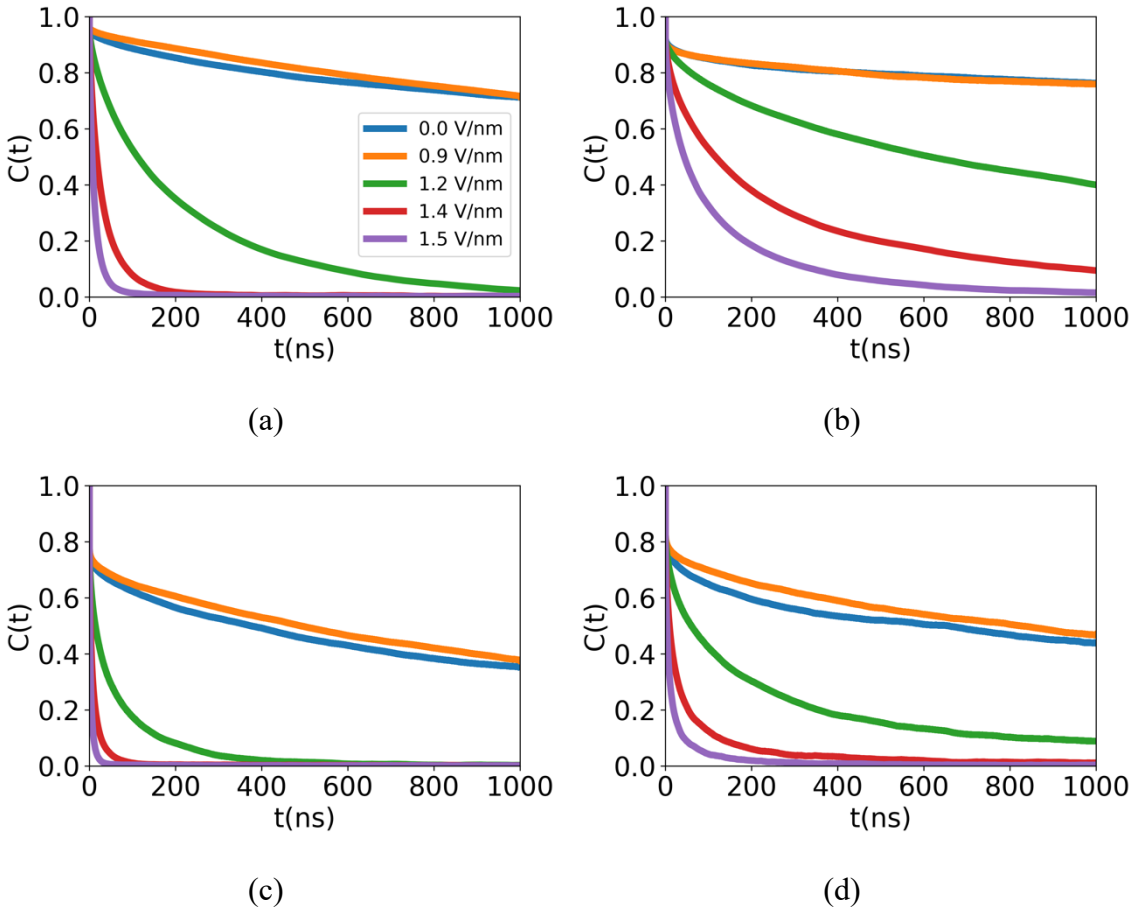

Figure 2.11. Association residence curves in Z2C/LiTFSI electrolytes (full charge). (a) Li^+ and $[TFSI]^-$; (b) Li^+ and ZW; (c) ZW and $[TFSI]^-$; and (d) ZW and ZW

However, the value of the electric field threshold shifts from 0.7 to 1.2 V/nm, meaning more external forces are needed to break associations among electrolyte compounds. Such a shift is expected because full partial charges enhance electrostatic attractions among Li^+, anions and ZW molecules. As shown in Figure 2.10, the number of Li^+-ZW associations increases as the electric field reaches 1.2 V/nm. The residence curves in Figure 2.11 also indicate the same shift of the electric field threshold.

2.3.5 Ionic conductivity

To verify our simulations, we calculated the ionic conductivity of Z2C/LiTFSI and Z3C/LiTFSI electrolytes without the electric field at 325 K with scaled and full charges and compared them with experimental data. These ionic conductivities were calculated using the Nernst-Einstein equation, as $\sigma_{NE}=(e^2)/(Vk_BT)(n^+D^++n^-D^-)$ where e is the electron charge, n^+ and n^- are the numbers of cations and anions, D^+ and D^- are their diffusion coefficients, V is the volume of the simulation box, kB is Boltzmann constant, and T is the electrolyte temperature.

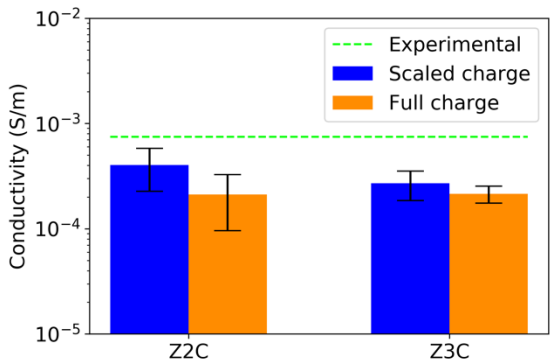

Figure 2.12. Ionic conductivity of Z2C/LiTFSI and Z3C/LiTFSI electrolytes without electric field.

The ionic conductivities of the simulations agree well with the experimental reports qualitatively[61]. Figure 2.12 shows the simulation results of ionic conductivity for Z2C/LiTFSI and Z3C/LiTFSI electrolytes without electric field. The experimental value of Z3C/LiTFSI system is also presented in Figure 2.12. The simulation results are in the same magnitude with the experimental observation but relatively smaller in values. The simulation result with the scaled charges is 64% less than the experimental one, while that with the full charges is 71% less than experimental data. The difference between ionic

conductivity in simulations and experiments may be because the Nernst-Einstein equation cannot describe the system's multiple molecular and ionic associations.

We also explore the change of the ionic conductivities for the Z2C/LiTFSI and Z2C/LiBETI electrolytes under the electric fields. The ionic conductivity of the electrolytes was calculated by driving the net ionic current by the applied electric field. This calculation was performed based on the definition of ionic conductivity. The net ionic current was the sum of net cationic and anionic currents along the electric field direction (z-direction). The net cationic and anionic currents were determined by analyzing the number of cations and anions crossing an *xy*-plane perpendicular to the electric field direction. The net ionic current was averaged over five 200-ns blocks.

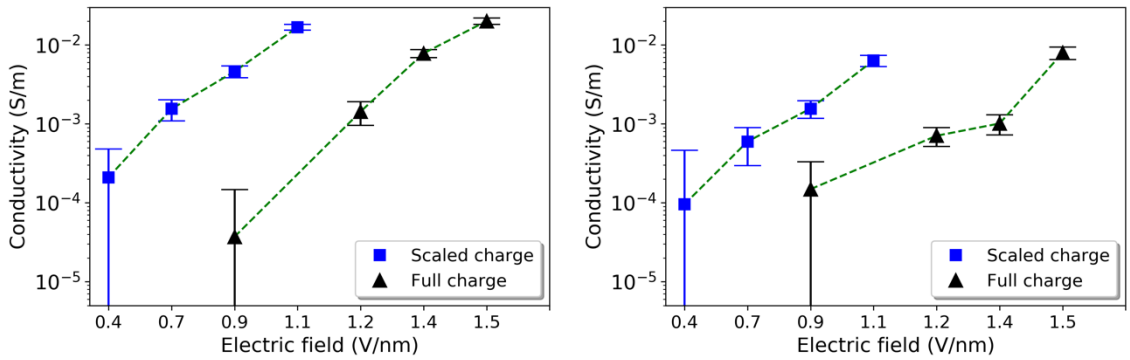

(a) (b)

Figure 2.13. Ionic conductivity of electrolytes under electric field. (a) Z2C/LiTFSI; (b) Z2C/LiBETI

Figure 2.13 shows the calculated ionic conductivities of Z2C/LiTFSI and Z2C/LiBETI electrolytes with the scaled and full charges under electric field ranging from 0.4 to 1.5 V/nm. As shown in Figure 2.13, the ionic conductivity for all four cases increases as electric field strength enhances. This trend is consistent with diffusion coefficients calculated using MSD curves in Figure 2.3. This consistency suggests that the diffusion coefficients and Nernst-Einstein equation could indicate the tendency for ionic conductivity even under an external field. Increasing the strength of the electric field not only enhances the directional transport of cations and anions, but also changes the ionic

associations in the electrolytes. Zwitterionic molecules can associate with both cations and anions, but they possess a zero net charge themselves. The variation of the ionic conductivity should be the synergistic effect of all the factors.

2.3.6 Conclusion

This work investigates the effect of zwitterionic molecules on ionic associations and transport in electrolytes under electric fields using MD simulations. We simulated electrolytes containing 1:1 Li salts (LiTFSI and LiBETI) and zwitterionic molecules composed of cationic imidazolium and anionic sulfonate groups under an external electric field ranging from 0 to 1.1 V/nm. The simulation trajectories were used to analyze diffusion coefficients of Li^+, anions and zwitterionic molecules, and their radial distribution functions and association number and stability. The analysis shows (1) zwitterionic molecules make small Li^+ and big anions diffuse at the same level under electric fields, and (2) the electric field must be stronger than a threshold to affect the diffusion and association of molecules and ions in the electrolytes. These two features indicate a close relationship between ionic transport and their associations in the electrolytes. Zwitterionic molecules may affect ionic and molecular associations in two ways. First, zwitterionic molecules enable Li^+ and anions to connect indirectly because they can associate with both. Second, zwitterionic molecules introduce extra associations in electrolytes that compensate the decrease of direct Li^+-anion associations due to electric fields.

CHAPTER 3. ZWITTERIONIC EFFECTS ON IONIC ASSOCIATION IN ETHYLENE OXIDE-BASED ELECTROLYTES

3.1 Introduction

Electrolytes with high ionic conductivity are critical for developing high-performance Li^+ batteries[2,6,51,97,98]. One of the keys to developing such electrolytes is to understand the mechanisms governing the ionic association and transport[6]. Zwitterionic (ZW) materials emerge as candidates for developing electrolytes with high ionic conductivity[27,28,54–57]. They contain both cationic and anionic groups[21,23,58]. Such a unique structure enables them to associate with both cations and anions[26-28, 47]. Despite the encouraging experimental observations[27,29,66,33,54–56,62–65], it remains unclear how ZW molecules affect the ionic associations and transport in the electrolytes. A better understanding of the effects would enable us to leverage the ability of ZW materials to design electrolytes with high ionic conductivity.

One question is how ZW molecules affect the ionic associations and transport in the known electrolytes such as those based on ethylene oxide (EO). One application of ZW molecules is to leverage their features to accelerate the ionic conductivity of existing electrolytes[54,55,63,64]. EO-based electrolytes have been widely used in Li^+ batteries[6,97,99–105]. One key issue for them is that Li^+ could be trapped by the association of multiple oxygen atoms, especially those from the single chain[106,107]. Therefore, polyethylene oxide (PEO) electrolytes usually have very low Li^+ transference number (t_{Li+}) (often in the range of 0.1–0.2)[108,109]. Morioka et al.[110] studied the effect of the EO side chain of polycarbonate-based electrolytes. The value of t_{Li+} decreased with the increase of EO side chain length. They suggested that the EO side groups trapped Li^+ ions. Another issue is that highly concentrated lithium electrolytes in oligoethers (3-4 M) suffer from high viscosities and low ionic conductivities[111]. The low ionic transport is possibly due to the increased Li^+-

anion association at high ionic concentration. ZW molecules may influence the Li^+-EO_x and Li^+-anion associations and affect the ionic transport in the electrolytes.

We hypothesize that ZW molecules could adjust ionic association in EO based electrolytes through the strong ion-ZW associations. Such strong associations may have two effects on ionic associations that could lead to the opposite consequences to ionic transport. First, it may release Li^+ from the "trapping" effect of EO_x chains. It was reported that ZW could mobilize Li^+, resulting in high t_{Li+} values. For example, the t_{Li+} values were over 0.5 in the mixture of LiTFSI (lithium bis (trifluoromethanesulfonyl) imide) and ZW molecules containing trifluoromethylsulfonylamide or organoborate anionic groups[72,112]. However, the mechanism remains unclear. We hypothesize that ZW molecules may release Li^+ from the association with EO_x chains by two ways. First, ZW molecules may compete with EO_x chains and reduce Li^+-O(EO_x) associations. Second, ZW molecules may associate with the oxygen cites on EO_x chains and act as separators to reduce the interaction between Li^+ and EO_x chains.

Second, the ion-ZW associations may slow down Li^+ transport themselves if they are too strong. Due to larger mass, ZW molecules are not as mobile as Li^+ ions. The strong Li^+-ZW association may decrease the mobility of Li^+ to match with that of ZW molecules. For instance, Ohno et al.[56] suggested that the design of ZW molecules should avoid strong Li^+-ZW associations.

ZW materials have shown their potential in energy applications despite the unclear mechanisms. Research has reported the use of ZW materials to increase the ionic conductivity of electrolytes[54,55,63,64]. ZW gel electrolytes can be developed with high ionic conductivity and mechanical strength. For instance, the Panzer group reported ZW co-polymers sulfobetaine vinylimidazole and 2-methacryloyloxyethyl phosphorylcholine with ionic conductivity up to 6.7 $mS \cdot cm^{-1}$ and compressive elastic moduli up to 11 MPa[27–29,62]. ZW addition also increased cycle stability in poly(ethylene glycol)dimethyl ether

(PEGDME) electrolytes[65,66]. Moreover, some research showed the applications of ZW materials in capacitors[67,68], fuel cells[69–71] and solar cells[113].

The current understanding of ion-ZW interactions is limited. Shao et al.[24,60] simulations showed that ZW molecules could associate strongly with Li^+. ZW molecules can also associate among themselves, depending on the types of cationic and anionic groups. Narita et al.[72] showed that the N-ethylimidazolium cation of the ZW molecule interacted with the anions more than with themselves. The design of ZW molecule structure can affect their ability to disassociate Li^+-anion associations. In their experiments, the ionic conductivity of ZW with N-methylpyrrolidinium cationic group was lower than that of ZW with N-ethylimidazolium cationic group. They also found that the design of ZW molecules with one carbon spacer was not effective in disassociating Li^+ and $[TFSI]^-$.

Based on the above hypothesis, we will investigate the ionic associations and transport in several EO based electrolytes with and without ZW molecules using molecular dynamics (MD) simulations. The focus is to reveal how the presence of ZW molecules may change the structural and dynamic properties of ionic associations in the electrolytes and how these changes may affect ionic transport. This work will use four EO based molecules: EO_2, EO_3, EO_4, and EO_5, as the model system, LiTFSI as the model for Li salt; and the ZW molecules containing cationic imidazolium and anionic sulfonate groups. We set two types of LiTFSI/EO_x systems to compare with the corresponding LiTFSI/EO_x/ZW systems and labeled them as case A and B separately. The case A systems have the same Li^+: O(EO_x) molar ratio as the LiTFSI/EO_x/ZW systems, and the case B systems have a similar molar concentration of Li^+ to the LiTFSI/EO_x/ZW systems. By keeping the Li^+: O(EO_x) molar ratio constant and adding ZW molecules (case A), we can investigate how ZW molecules can change ionic associations and transport in the electrolytes. However, adding ZW molecules changes the LiTFSI molar concentration of the EO based electrolytes, which may influence ionic conductivity[111]. Therefore, we will also investigate LiTFSI/EO_x electrolytes with a similar molar concentration (case B) to LiTFSI/EO_x/ZW electrolytes to

better understand the effect of ZW molecules. The rest of the chapter is as follows: Section 3.2 describes the molecular model and simulation detail; Section 3.3 presents the results and discussion, and Section 3.4 presents the conclusion.

3.2 Molecular model and simulation detail

3.2.1 Molecular model

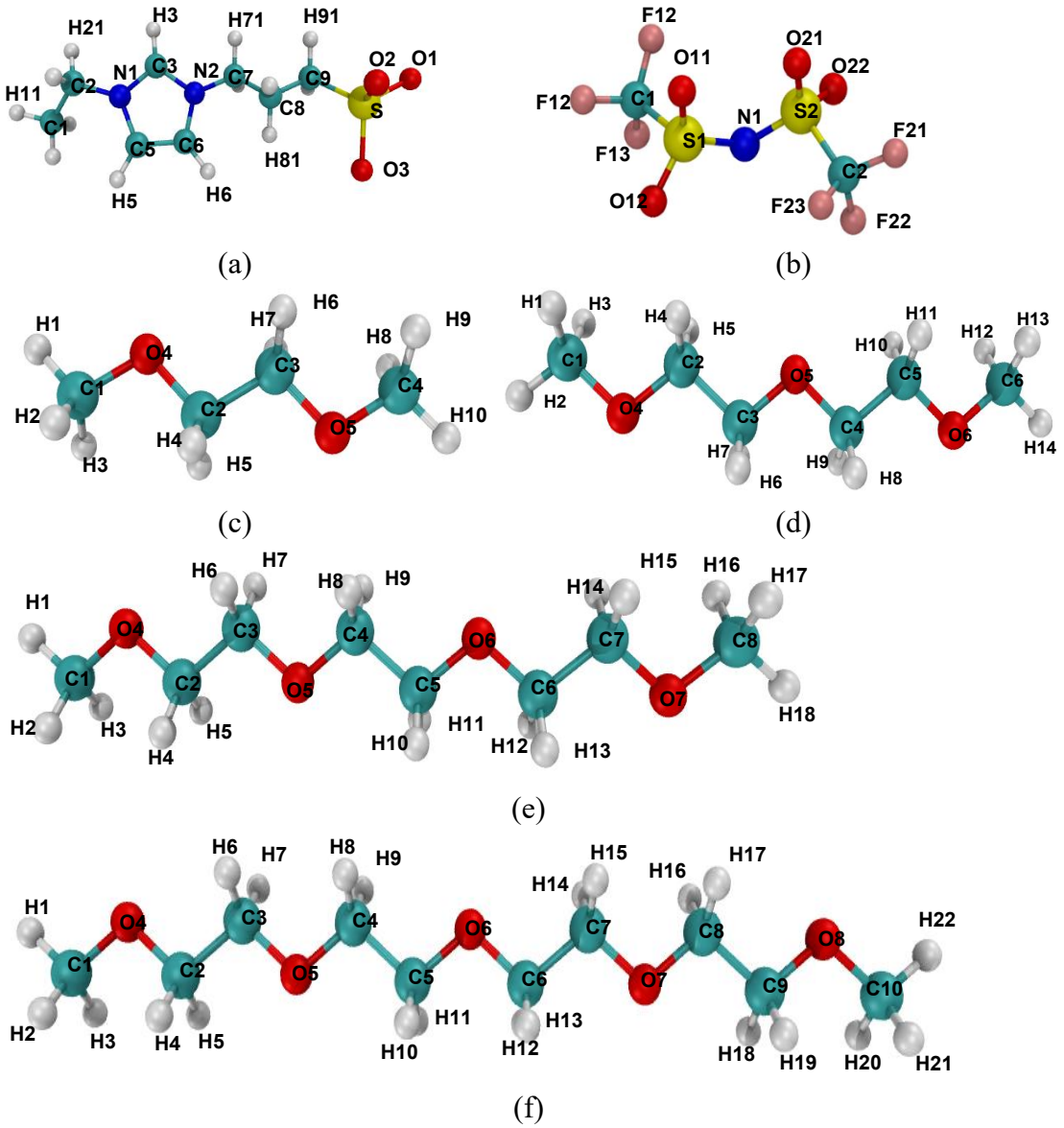

Figure 3.1. Molecular structures of (a) ZW, (b) $[TFSI]^-$, (c) EO_2, (d) EO_3, (e) EO_4, and (f) EO_5.Every atom labeled with a unique name.

This work describes all ions and molecules using the all-atom model. Figure 3.1 shows the structures of ZW molecules, $[TFSI]^-$ ions and the four EO_x molecules used in this work. The non-bonded potential is a sum of the short-range Lennard-Jones 12-6 potential and long-range Coulomb potential (equation 3.1). The bonded potential is a sum of bond, angle and dihedral-angle potentials. The OPLSAA force field and its derivatives[85,86] were used to describe the bonded and nonbonded interactions in the system. Table B1 lists the non-bonded force field parameters used in this work.

$$E = \sum_{i}\sum_{j<i}\left\{\frac{1}{4\pi\varepsilon_0}\frac{q_i q_j e^2}{r_{ij}} + 4\varepsilon_{ij}\left[\left(\frac{\sigma_{ij}}{r_{ij}}\right)^{12} - \left(\frac{\sigma_{ij}}{r_{ij}}\right)^{6}\right]\right\} \quad (3.1)$$

Table 3.1. Details of the simulation systems

#	Li^+	$[TFSI]^-$	EO_x	ZW	Li^+: $O(EO_x)$	Molar conc. (mol/L)	total number of atoms
Systems with ZW molecules							
1	200	200	300 EO_2	200	1:3	2.2	13600
2	200	200	200 EO_3	200	1:3	2.2	13400
3	200	200	150 EO_4	200	1:3	2.3	13300
4	200	200	120 EO_5	200	1:3	2.3	13240
Case A: Systems with the same Li^+:$O(EO_x)$ molar ratio							
5	200	200	300 EO_2		1:3	3.5	8000
6	200	200	200 EO_3		1:3	3.6	7800
7	200	200	150 EO_4		1:3	3.7	7700
8	200	200	120 EO_5		1:3	3.7	7640
Case B: Systems with the similar molar concentration							
9	100	100	300 EO_2		1:6	2.2	6400
10	100	100	200 EO_3		1:6	2.4	6200
11	100	100	150 EO_4		1:6	2.5	6100
12	100	100	120 EO_5		1:6	2.5	6040

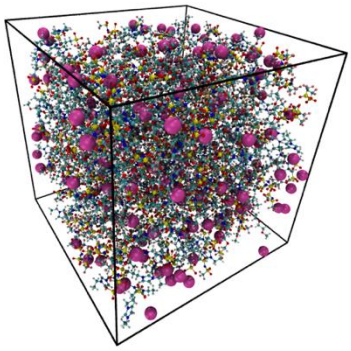

Figure 3.2. Initial configuration of a simulation box containing 200 Li^+, 200 $[TFSI]^-$, 200 ZW molecules and 120 EO_5 molecules. (Li^+ ions are represented using the VDW model and the others are represented by the CPK model). This figure was generated using VMD-1.9.1[84]

This work prepares the simulation systems by randomly placing certain numbers of Li^+, $[TFSI]^-$, EO_x molecules and ZW molecules in a cubic box. Table 3.1 lists the detail of the three types of simulation systems. The initial configurations were prepared using Packmol[83]. Figure 3.2 shows the initial configuration of a simulation box containing 200 Li^+, 200 $[TFSI]^-$, 200 ZW molecules and 120 EO_5 molecules.

3.2.2 Simulation detail

The whole simulation process contains four steps. First, energy minimization was conducted to eliminate any bad contacts between atoms. Second, a 100-ns isothermal-isobaric (NPT) MD simulation was conducted at 500 K and 100 kPa to relax the system fully. Third, a 200-ns NPT MD simulation was conducted at 353 K and 100 kPa to let the system reach the desired temperature and density. Fourth, an 800-ns canonical (NVT) MD simulation was conducted at 353 K to collect the data at a frequency of 10 ps. The Berendsen method[88] was used to control the temperature and pressure in the second and third steps because it enables the system to reach the controlled temperature and pressure in a fast pace. The velocity-rescaling method[89] was used to control the system temperature

in the fourth step. The short-range potential energies were calculated using a 1.0-nm cut-off, while the long-range electrostatic interaction energy was calculated using the particle mesh Ewald sum[90]. All bonds involving hydrogen atoms were constrained during the fourth step using the LINCS algorithm[91]. The energy minimization and MD simulations were conducted using Gromacs 2019[92].

3.3 Results and discussion

3.3.1 Diffusion coefficients of ions, EO_x and ZW molecules

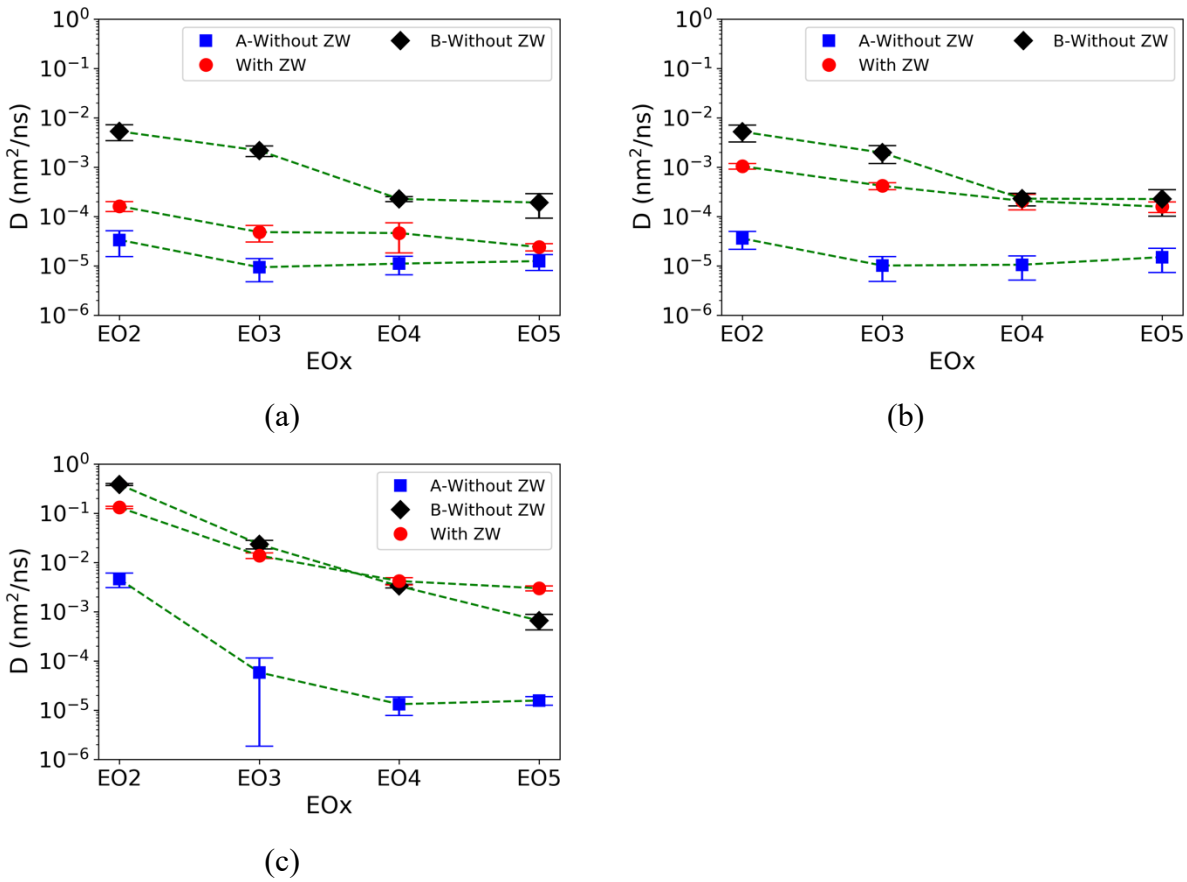

Figure 3.3. Diffusion coefficients of (a) Li^+, (b) $[TFSI]^-$ and (c) EO_x in LiTFSI/EO_x/ZW and LiTFSI/EO_x (cases A and B).

The presence of ZW molecules affects the diffusion of Li^+ in the EO-based electrolytes. Figure 3.3a shows the diffusion coefficients of Li^+ (D_{Li+}) in the 12 LiTFSI/EO_x

and LiTFSI/EO_x/ZW systems. The diffusion coefficients were calculated based on the corresponding mean square displacement curves of four 200-ns blocks from the 800-ns MD simulations using the Einstein equation $D = \lim_{t \to 0} \frac{\langle x(t+t_0) - x(t_0) \rangle}{2t}$. As shown in Figure 3.3a, D_{Li+} is the highest in the EO_2 electrolyte and decreases gradually in the EO_3, EO_4 and EO_5 electrolytes in cases A and B, consistent with the trend reported in the literature[111,114]. For all the four EO_x electrolytes, D_{Li+} with ZW is higher than that in case A but lower than that in case B. In other words, Li^+ diffuses faster in an EO_x/ZW mixture than in an EO_x solution with the same Li^+:O(EO_x) molar ratio, while more slowly than in an EO_x solution with the similar molar concentration.

The diffusion coefficients of $[TFSI]^-$ and EO_x molecules ($D_{[TFSI]-}$ and D_{EOx}) present a similar trend. Figure 3.3b and 3.3c show $D_{[TFSI]-}$ and D_{EOx} in the 12 LiTFSI/EO_x and LiTFSI/EO_x/ZW systems. They were also calculated using the Einstein method. As shown in Figure 3.3b and 3.3c, $D_{[TFSI]-}$ and D_{EOx} with ZW are higher than those in the case-A electrolytes. However, unlike D_{Li+} in LiTFSI/EO_x/ZW being lower than that in case-B electrolytes, $D_{[TFSI]-}$ and D_{EOx} in the EO_4 and EO_5 electrolytes are comparable to or even higher than those in the case-B electrolytes. Their values in the EO_2 and EO_3 electrolytes are smaller than those in the case-B electrolytes without ZW.

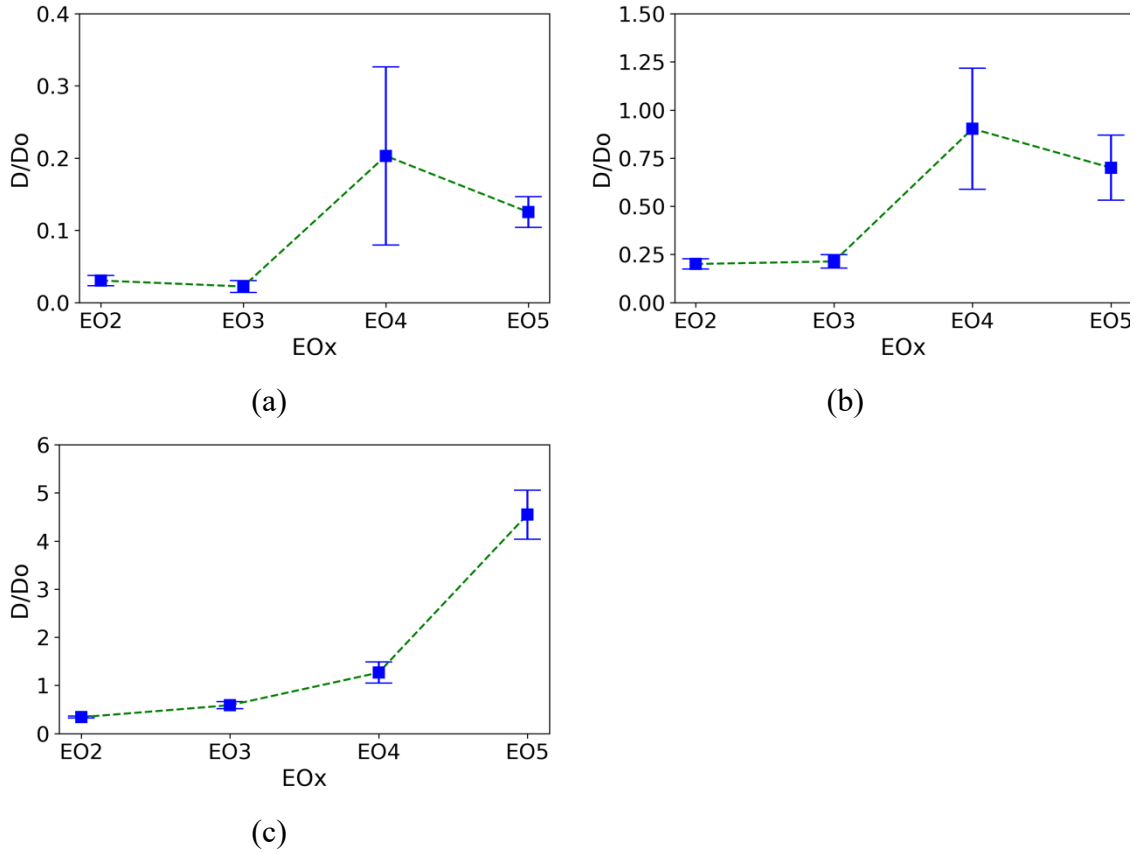

Figure 3.4. Ratio of diffusion coefficients D/Do (with ZW/case-B-without ZW) of (a) Li^+, (b) $[TFSI]^-$, and (c) EO_x.

The length of EO_x chains affects the influence of ZW molecules on the diffusion abilities of ions and molecules in the electrolytes. ZW may slow down ionic transport based on the first glimpse of the diffusion coefficients in Figure 3.3. Indeed, D_{Li+} in an EO_x/ZW electrolyte is smaller than that in an EO_x electrolyte with a similar molar concentration. However, this decreasing effect weakens as the length of EO_x chain increases. Figure 3.4 shows the ratio of diffusion coefficients in the electrolytes with ZW and those in case B for Li^+, $[TFSI]^-$ and EO_x molecules. The ratio for Li^+ increases by four times when the number of EO units increases from two to five. The increase is more obvious for $[TFSI]^-$ and EO_x. The typical PEO used in experiments may have hundreds to thousands of EO units. This dramatic increase indicates that ZW molecules may have the potential to increase the ionic conductivity of electrolytes composed of long PEO chains.

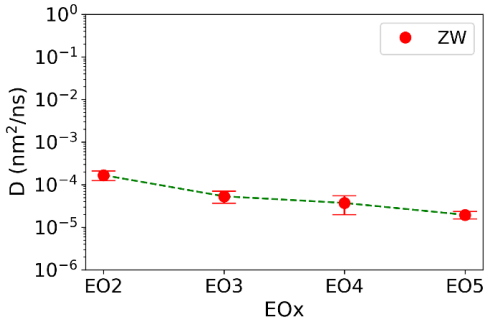

Figure 3.5. Diffusion coefficients of ZW molecules in LiTFSI/EO_x/ZW.

The diffusion of Li^+ and ZW molecules have a strong correlation. Figure 3.5 shows the diffusion coefficient of ZW molecules in the four LiTFSI/EO_x/ZW electrolytes. Its values are 16.6±4.2, 5.3±1.6, 3.7±1.7 and 1.9±0.4 ($\times 10^{-5}$ nm^2/ns) in EO_2, EO_3, EO_4 and EO_5 electrolytes respectively, similar to those of Li^+ in the same electrolytes in Figure 3.3a. Such similarity in diffusion coefficients implies that Li^+ may associate with ZW molecules. We will analyze the association among them in the following sections.

3.3.2 Radial distribution functions

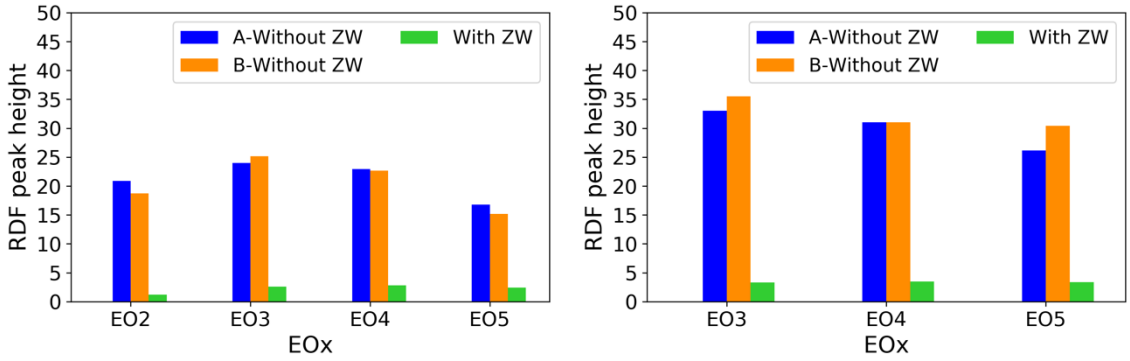

Figure 3.6. Peak height in radial distribution functions (RDFs) of (a) Li^+-O(EO_x, ter) and (b) Li^+-O(EO_x, mid) with and without ZW molecules.

The presence of ZW molecules dissociates the Li^+-EO_x associations. Figures 3.6a and 3.6b show the peak heights of the Li^+-O(EO_x, ter) and Li^+-O(EO_x, mid) radial distribution functions (RDFs) in the 12 electrolyte systems. The corresponding RDFs were shown in Figure B1. O(EO_x, ter) refers to the two O atoms at the two ends of an EO_x molecule. The EO_2 molecules only have the terminal O atoms. O(EO_x, mid) refers to the other O atoms not at the ends of an EO_x molecule. As shown in Figure 3.6, the peak heights of Li^+-O(EO_x, ter) and Li^+-O(EO_x, mid) RDFs are around 20-30 in the cases A and B without ZW. The RDF peaks indicate that there are Li^+-EO_x associations, consistent with the literature reports[114–116]. These RDF peak heights decrease to less than five with the presence of ZW molecules. As shown in Figure 3.6a, the peak heights of Li^+-O(EO_x, ter) RDF decreases to only 1.2 for EO_2 and ~2.5 for the other three EO-based electrolytes if ZW molecules present. The peak height of Li^+-O(EO_x, mid) also decreases to only ~3.5 in the three EO based electrolytes, as shown in Figure 3.6b. Such a dramatic decrease in the RDF peak heights indicates that the Li^+-EO_x associations dissociate with the presence of ZW molecules.

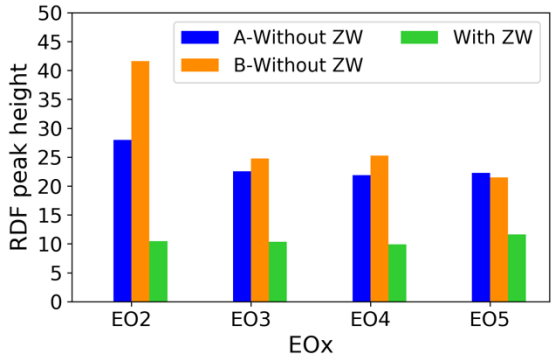

Figure 3.7. Peak height in Li^+-O11($[TFSI]^-$) RDFs in the 12 electrolytes with and without ZW.

The presence of ZW molecules also dissociates the Li^+-$[TFSI]^-$ associations. Figure 3.7 shows the peak heights of the Li^+-O11($[TFSI]^-$) RDFs. The high peaks for the eight systems without ZW molecules show that Li^+ associates with $[TFSI]^-$, consistent with the literature report[24]. The presence of ZW molecules causes the RDF peak height to drop from around 25 to around 10, similar to the phenomenon occurring for Li^+-EO_x associations. Such a decrease in RDF peak heights shows that ZW molecules also dissociate the Li^+-$[TFSI]^-$ associations in the electrolytes.

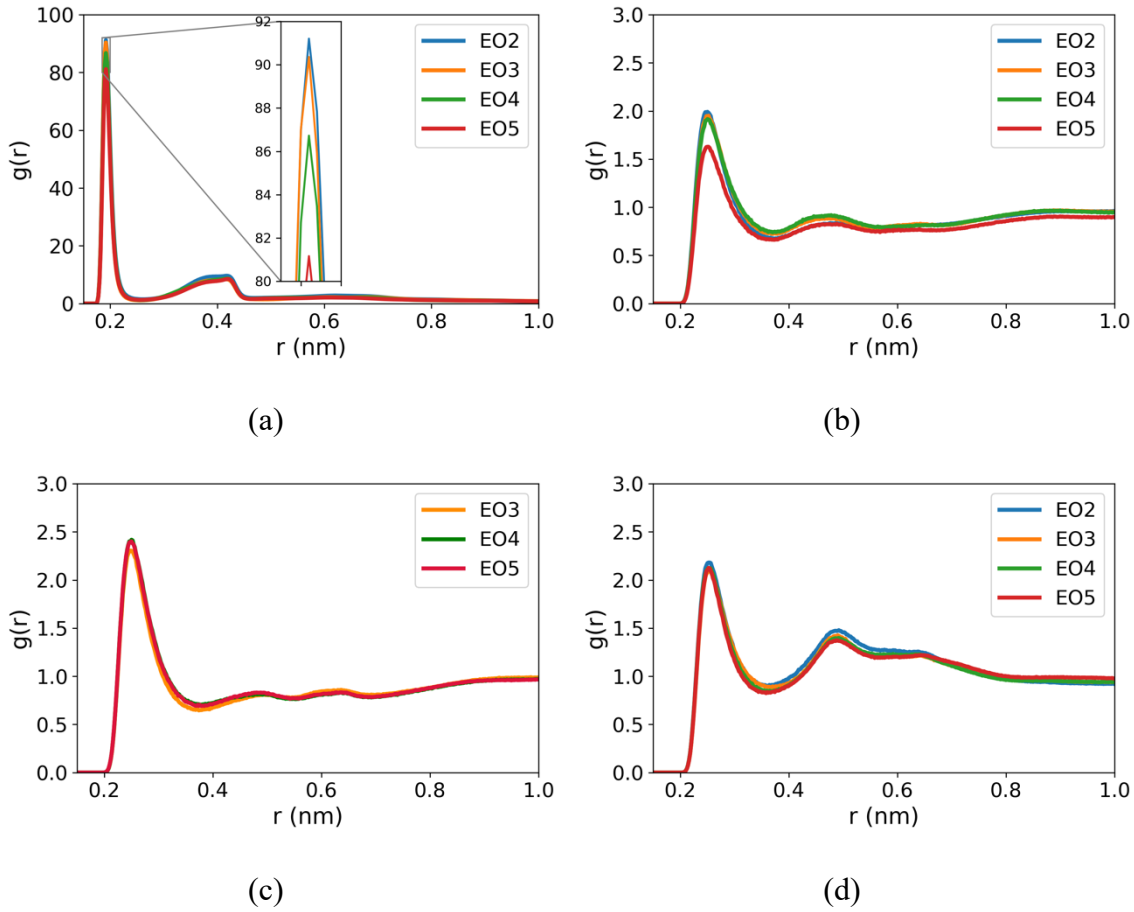

Figure 3.8. RDFs of (a) Li^+-O1(ZW), (b) H5(ZW)-O (EO_x, ter), (c) H5(ZW)-O (EO_x, mid) and (d) H5(ZW)-O11($[TFSI]^-$).

The ability of ZW molecules to dissociate Li^+-EO_x and Li^+-$[TFSI]^-$ associations may relate to their ability to associate with Li^+. Figure 3.8 shows the RDFs between Li^+, ZW, EO_x and $[TFSI]^-$. We deploy H5(ZW)-O11($[TFSI]^-$) RDF as a representative for ZW-$[TFSI]^-$ association because the four oxygen atoms O11, O12, O21 and O22 on $[TFSI]^-$ have same charges and relative geometric positions. For a similar reason, we choose O1 to represent the anionic groups on ZW molecules and H5 to represent the hydrogen atom on the cationic groups on ZW molecules. Figure 3.8a shows the Li^+-O1(ZW) RDFs in the four EO based electrolytes. These RDFs present a peak with a height of around 80-90 at 0.2 nm. The high peaks in RDFs indicate the presence of Li^+-ZW associations in all the four EO

electrolytes, consistent with our previous simulation results[117] for ZW molten salts. ZW molecules compete with EO_x and $[TFSI]^-$ to associate with Li^+. Such a competition weakens the pre-existing Li^+-EO_x and Li^+-$[TFSI]^-$ associations.

ZW molecules could also associate with $[TFSI]^-$ and EO_x molecules through their cationic groups. Figures 3.8b and 3.8c show the H5(ZW)-O(EO_x, ter) and H5(ZW)-O(EO_x, mid) in the four EO-based electrolytes. The peak heights of these RDFs are about 1.5-2.5 at around 0.37 nm. These RDF peaks indicate that ZW molecules could associate with EO_x molecules. Figure 3.8d shows H5(ZW)-O11($[TFSI]^-$) RDFs. These RDFs present a peak of a height of around 2.2 at around 0.37 nm. The positions of these RDF peaks agree well with our previous simulations of ZW/LiTFSI mixtures[29]. These RDF peaks indicate the existence of ZW-$[TFSI]^-$ associations.

3.3.3 Association number

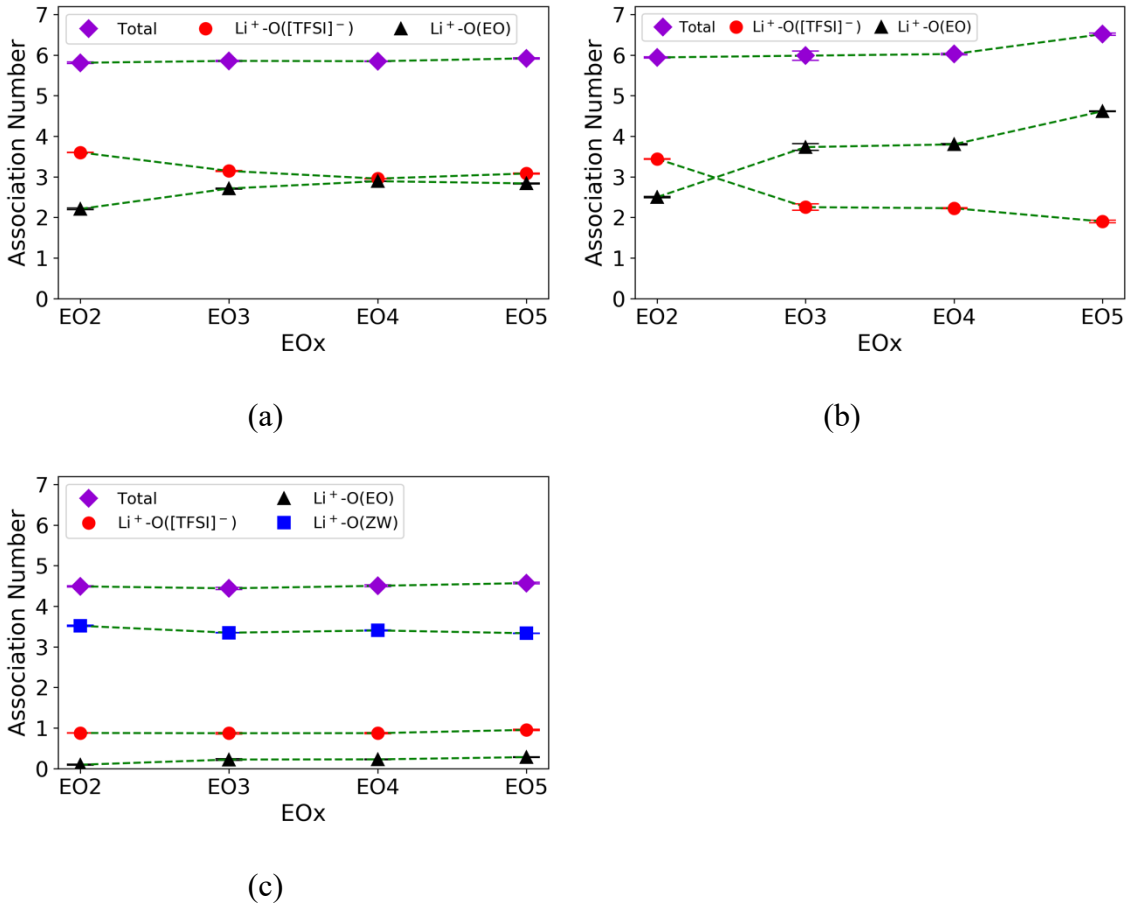

Figure 3.9. Association number of Li^+-O(EO_x), Li^+-O([TFSI]$^-$) and Li^+-O(ZW) and their sum. (a) case A without ZW, (b) case B without ZW and (c) electrolytes with ZW.

The numbers of Li^+-O(EO_x) and Li^+-O([TFSI]$^-$) associations are generally similar in the EO based electrolytes in cases A and B. Figure 3.9a shows the numbers of Li^+-O(EO_x) and Li^+-O([TFSI]$^-$) associations and their sum ($N_{Li+-O(Eox)}$, $N_{Li+-O([TFSI]-)}$ and N_{total} respectively) in the four electrolytes in case A without ZW molecules. The values of $N_{Li+-O(Eox)}$, $N_{Li+-O([TFSI]-)}$ were calculated by numerally integrating the corresponding RDFs within a threshold (Li^+-O(EO_x): 0.35 nm, Li^+-O([TFSI]$^-$): 0.31 nm). As shown in Figure 3.9a, $N_{Li+-O(Eox)}$ is around 2-3 and $N_{Li+-O([TFSI]-)}$ is around 3-4 in the four electrolytes without

ZW molecules. Figure 3.9b shows $N_{Li+-O(Eox)}$, $N_{Li+-O([TFSI]-)}$ and their sum N_{total} in the four electrolytes in case B without ZW molecules. The values of $N_{Li+-O(Eox)}$ in case B is slightly higher than those in case A, probably because the molar ratio of Li^+:O(EO_x) in case B is less than that in case A. The values of N_{total} are around 6 in the eight electrolytes in both cases, indicating that Li^+ is tightly surrounded by other ions and molecules.

ZW molecules decrease $N_{Li+-O(Eox)}$ and $N_{Li+-O([TFSI]-)}$. As shown in Figure 3.9c, the value of $N_{Li+-O(Eox)}$ is only 0.1-0.2, less than 10% of that in the electrolytes without ZW molecules. The value of $N_{Li+-O([TFSI]-)}$ decreases to around one, only 33% of that in the electrolyte without ZW molecules. The value of N_{total} decreases to around 4.5 in the four electrolytes with ZW molecules, 75% of that without ZW molecules. The decrease in N_{total} indicates that Li^+ becomes less surrounded by ions and molecules.

ZW molecules dominate the association of Li^+ when they are present. As shown in Figure 3.9c, the values of $N_{Li+-O(ZW)}$ are around 3.5. The Li^+-ZW associations account for around 80% of the total associations. The dominance of Li^+-ZW associations suggests that Li^+ prefers to associate with ZW molecules. This preference enables ZW molecules to dissociate the Li^+-EO_x and Li^+-$[TFSI]^-$ associations.

3.3.4 Association status

EO_x, $[TFSI]^-$ and ZW molecules can associate with Li^+ via their multiple O atoms. The more O atoms which a molecule can use to associate with Li^+, the tighter that association could be. Here we analyze the distribution of possible association status between Li^+ and EO_x, $[TFSI]^-$ and ZW molecules. The association statuses are labeled by the number of O atoms that a molecule uses to associate with a Li^+ ion. For instance, a Li^+-EO_5 association is of "single" status if an EO_5 molecule uses only one of its five O atoms to associate with a Li^+ ion. In the same manner, a Li^+-EO_5 association is of "quintuple" status if an EO_5 molecule uses five O atoms to associate with a Li^+ ion. Likewise, the

"single" or "double" status of a Li^+-$[TFSI]^-$ association means that one or two O atoms on the same $[TFSI]^-$ molecules associate with a Li^+ ion respectively. For a Li^+-ZW association, the "single" or "double" status refers to whether the number of O atoms on a ZW molecule in association with a Li^+ ion is one or two. This analysis only uses the data from the electrolytes in case A and those with ZW since the electrolytes in cases A and B show similar phenomena.

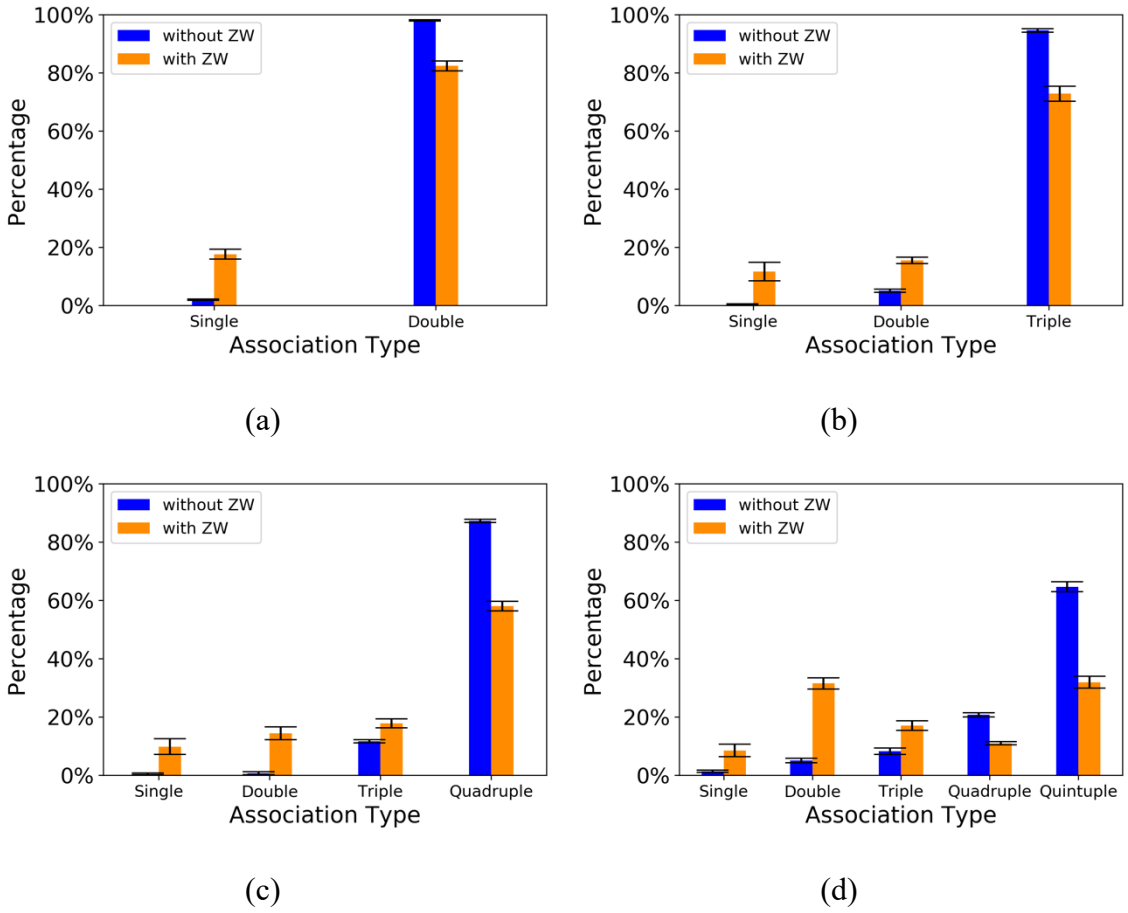

Figure 3.10. Percentage of Li^+-EO_x association status with and without ZW molecules. (a) EO_2, (b) EO_3, (c) EO_4, and (d) EO_5.

All the four types of EO_x molecules prefer to associate with a Li^+ ion using all O atoms. Figure 3.10 shows the percentages of possible Li^+-EO_x association statuses in the four electrolytes without ZW molecules. As shown in Figure 3.10a, almost 99% of EO_2

molecules associate with a Li^+ ion using both O atoms. The majority of the other three EO_x molecules also use all their O atoms to associate with a single Li^+ ion. Such multiple-O associations could trap Li^+ and slowdown their transport. Such trapping effect of EO_x molecules has been considered as one of the major issues for EO-based electrolytes.

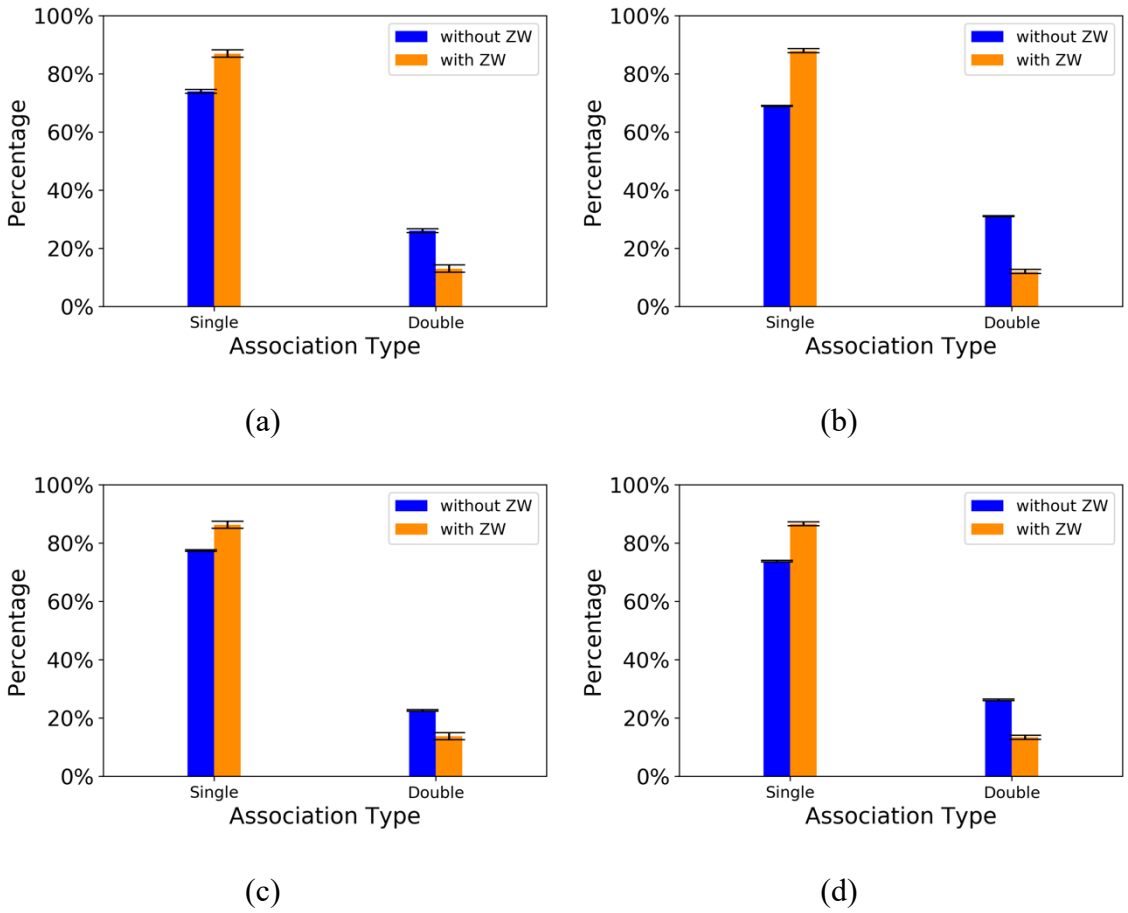

Figure 3.11. Percentage of Li^+-$[TFSI]^-$ association status with and without ZW in (a) EO_2, (b) EO_3, (c) EO_4, and (d) EO_5.

ZW molecules release Li^+ from the trapping effect of EO_x molecules. Figure 3.10 also shows the percentage of possible Li^+-EO_x association statuses in the four electrolytes with ZW molecules. The presence of ZW molecules decreases the percentage of "double" status from almost 99% to 80% for the EO_2 electrolyte, the percentage of "triple" status from 95% to 75% for the EO_3 electrolyte, the percentage of "quadruple" status from 90%

to 60% for the EO_4 electrolyte, and the percentage of "quintuple" status from 65% to 35% for the EO_5 electrolyte. These association statuses should have the strongest trapping effect on Li^+ for the corresponding EO_x molecules. The decrease in their percentages implies that the ZW molecules could release Li^+ from their trapping effect, which may increase the diffusion ability of Li^+.

The presence of ZW molecules also weakens the trapping effect of $[TFSI]^-$ on Li^+. Figure 3.11 shows the percentages of the "single" and "double" status for Li^+-$[TFSI]^-$ associations in all the eight systems. About 75% of Li^+-$[TFSI]^-$ associations are of the "single" status, while the rest 25% is of the "double" status for all the four EO-based electrolytes without ZW molecules. The percentage of "double" status decreases to around 13% for all EO-based electrolytes with ZW molecules. The trapping effect of $[TFSI]^-$ should be stronger in the "double" status than the "single" status. A $[TFSI]^-$ ion in "double" status uses two O atoms while that in "single" status just uses one O atom to associate with a Li^+ ion. The decrease in the percentage of "double" status thus implies that the presence of ZW molecules causes Li^+-$[TFSI]^-$ association weaker in general.

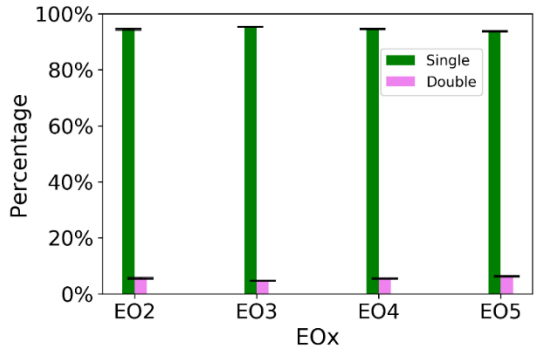

Figure 3.12. Percentage of "single" and "double" status of Li^+-ZW associations.

Most ZW molecules associate with a Li^+ ion using only one O atom. Figure 3.12 shows the percentages of the "single" and "double" status of the Li^+-ZW association in the four EO_x systems. As shown in Figure 3.12, 95% of Li^+-ZW associations are of "single"

status in the four EO_x electrolytes. Thus, ZW molecules do not wrap Li^+ by multiple-O associations as much as EO_x and $[TFSI]^-$ do.

Figure 3.13 shows some snapshots that represent Li^+ association status in the four EO based electrolytes with and without ZW molecules. These snapshots show that the presence of ZW disrupts the coordination shell of Li^+, making them less surrounded by other ions and molecules. For instance, as shown in Figure 3.13d, the Li^+ is wrapped by the EO_5 molecule using five oxygen atoms and $[TFSI]^-$ ion using two oxygen atoms (left). But the presence of ZW molecules disrupts this wrapping (right). In the snapshot, the $[TFSI]^-$ and EO_5 molecules now use only one oxygen to associate with the Li^+ ion. The detailed explanation of the snapshots is shown in Table 3.2.

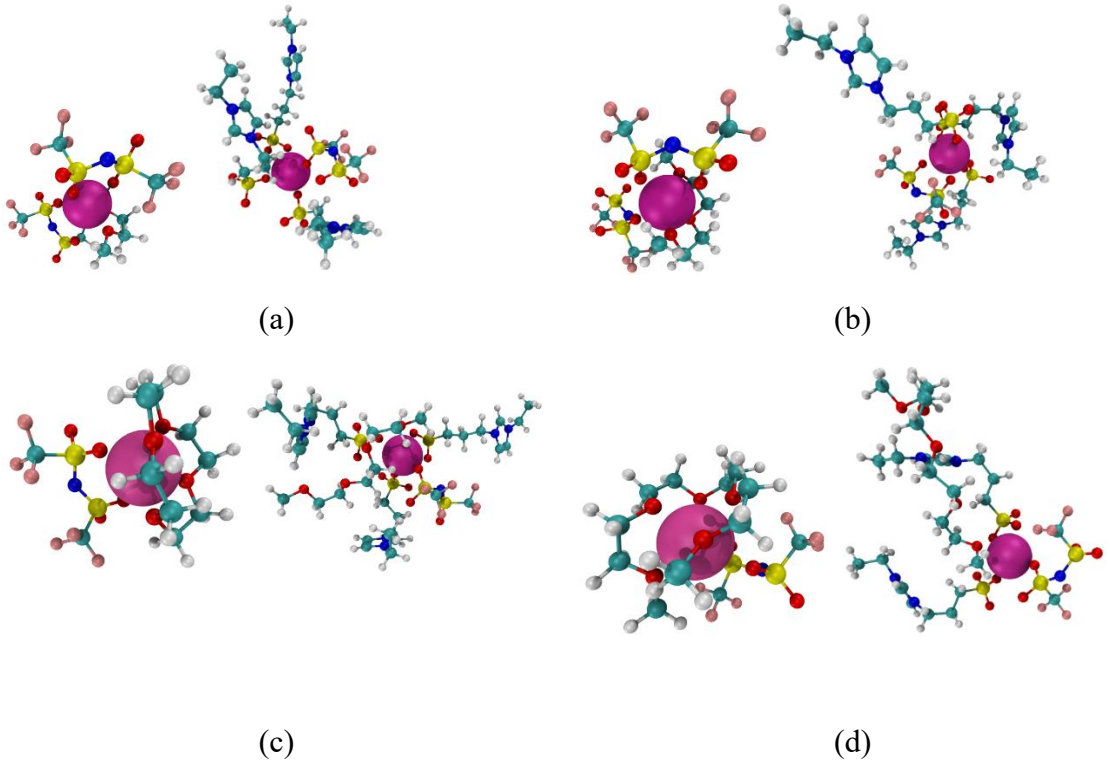

Figure 3.13. Snapshot of Li^+ association in the electrolytes with and without ZW (a) EO_2, (b) EO_3, (c) EO_4, (d) EO_5. For each panel, the snapshots on the left are those from the electrolytes without ZW and the snapshots on the right are from the electrolytes with ZW.

Table 3.2. Details of the snapshots in Figure 3.13.

Figure #	EO_x	$[TFSI]^-$	ZW	$N_{Li+-O(Eox)}$	$N_{Li+-O([TFSI]-)}$	$N_{Li+-O(ZW)}$
13a left	1	2	0	2	4	0
13a right	0	1	3	0	1	3
13b left	1	2	0	3	3	0
13b right	0	1	3	0	2	4
13c left	1	1	0	4	2	0
13c right	1	1	3	1	1	4
13d left	1	1	0	5	2	0
13d right	1	1	2	1	1	2

3.3.5 Association dynamics

We analyzed the stability of ionic associations based on their residence curves *C(t)* to illustrate the effect of ZW molecules on association dynamics of EO-based electrolytes. Figure 3.14 shows the residence curves *C(t)* for the Li^+-O(EO_x, ter), Li^+-O(EO_x, mid), Li^+-O11($[TFSI]^-$) and Li^+-O1(ZW) associations in the EO_2, EO_3, EO_4 and EO_5 electrolytes with and without ZW molecules (case A). The residence curves *C(t)* were calculated as $C(t) = \frac{1}{N_0}\sum_{j=0}^{N_0}\frac{\langle P_j(0)P_j(t)\rangle}{\langle P_j(0)\rangle^2}$ where N_0 is the total number of certain associations at $t = 0$, $P_j(0) = 1$, $P_j(t) = 1$ if the association j still exists at time t and $P_j(t) = 0$ if the associate j breaks at time t. We do not consider the associations that could be broken between timesteps (Δt = 10-ps).

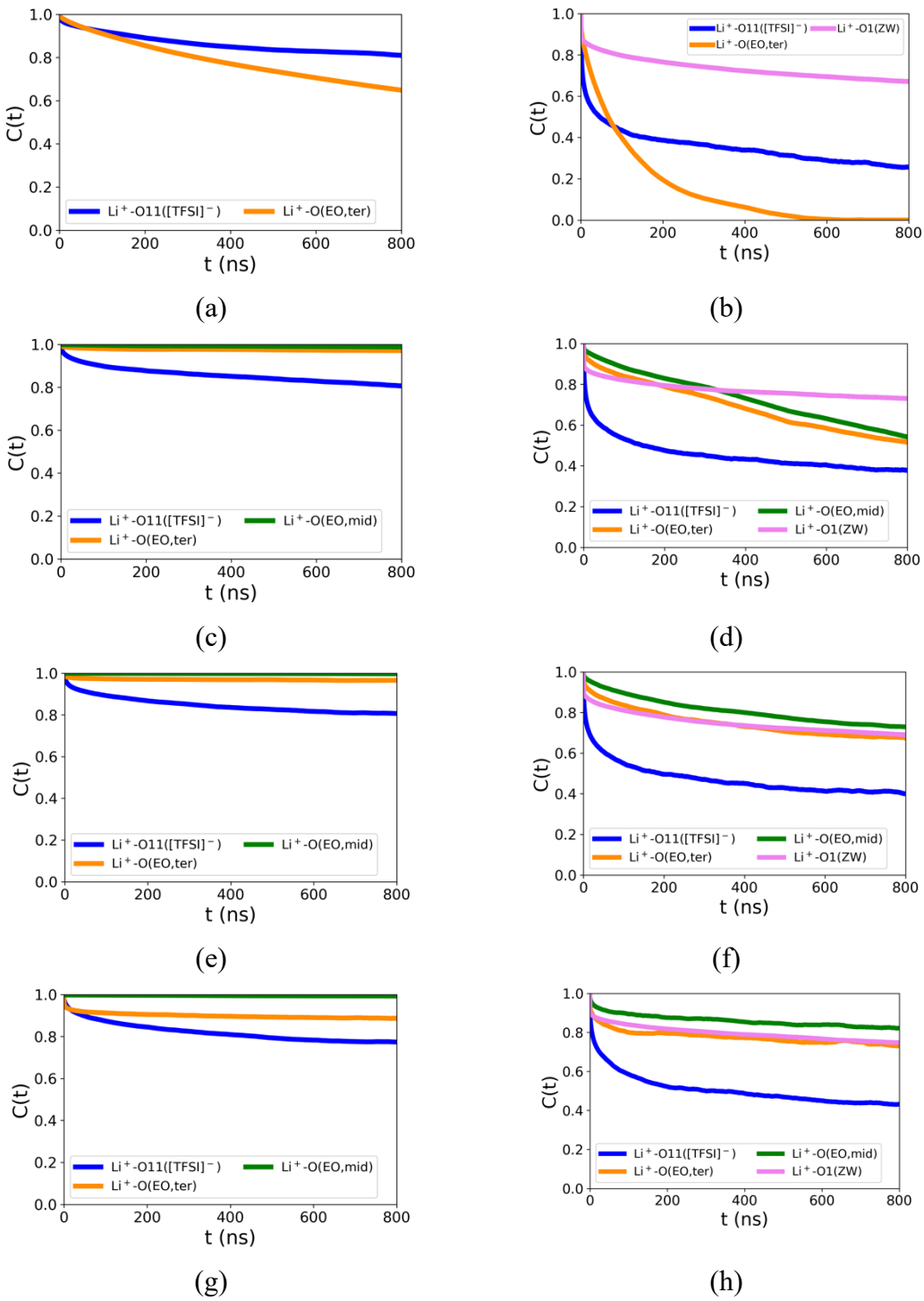

Figure 3.14. Residence curve C(t) of all associations in (a) EO_2 without ZW (b) EO_2 with ZW, (c) EO_3 without ZW (d) EO_3 with ZW, (e) EO_4 without ZW (f) EO_4 with ZW, (g) EO_5 without ZW (h) EO_5 with ZW.

ZW molecules not only dissociate Li^+-EO_x and Li^+-$[TFSI]^-$ associations but also weaken the stability of remaining associations. As shown in Figure 3.14a and 3.14b, *C(t)* for the Li^+-O(EO_2) associations remains 0.65 at *t*=800 ns in the electrolyte without ZW molecules, while its value becomes zero at *t*=600 ns in the electrolyte with ZW molecules. The values of *C(t)* show that around 65% of Li^+-O(EO_2) associations could maintain longer than 800 ns without ZW molecules. However, none of them could maintain longer than 600 ns with the presence of ZW molecules. The presence of ZW molecules also accelerates the decay of *C(t)* for the Li^+-O11($[TFSI]^-$) association in the EO_2 electrolyte. Its value is 0.8 at *t*=800 ns without ZW molecules, while only 0.2 at *t*=800 ns with ZW molecules. Similar phenomenon occurs in the EO_3, EO_4 and EO_5 electrolytes, as shown in Figure 3.14. The *C(t)* curves for the Li^+-O(EO_x) and Li^+-O11($[TFSI]^-$) associations also decrease faster with the presence of ZW molecules. Such acceleration in the decay rate indicates that ZW molecules decrease the stability of the remaining associations between Li^+, $[TFSI]^-$ and EO_x molecules.

The Li^+-O1(ZW) associations are very stable in all the four EO-based electrolytes. As shown in Figure 3.14b, 3.14d, 3.14f and 3.14h, the *C(t)* value for the Li^+-O1(ZW) associations remains around 0.8 in the EO_2, EO_3, EO_4 and EO_5 electrolytes. Around 80% of Li^+-O1(ZW) associations should maintain longer than 800 ns in the EO_2, EO_3, EO_4 and EO_5 electrolytes. This survival percentage is much higher than those of Li^+-O11($[TFSI]^-$) associations in the same electrolyte. The higher stability indicates that the Li^+-ZW association is stronger than the Li^+-$[TFSI]^-$ association. The residence curves also show that the stability of Li^+-O1(ZW) association is much better than that of Li^+-O(EO_2) and Li^+-O(EO_3) and similar to that of Li^+-O(EO_4) and Li^+-O(EO_5) associations. The stability comparison suggests that the Li^+-ZW association is stronger than the Li^+-EO_x association in EO_2 and EO_3 and is similar to the Li^+-EO_x association in EO_4 and EO_5 electrolytes. The Li^+-ZW associations not only account for most of the ionic associations in the electrolytes (Figure 3.9) but also are very stable. Therefore, adding ZW molecules has two

consequences. The presence of ZW molecules causes Li^+ not only to be released from associations with EO_x and $[TFSI]^-$ but also to engage in the strong Li^+-ZW associations.

The structural and dynamic features of ionic associations in the eight electrolytes suggest a plausible mechanism by which ZW molecules can accelerate the ionic transport in EO based electrolytes. ZW molecules can free Li^+ from the trapping effect by the multi-O associations of EO_x molecules (Figure 3.10). They weaken and dissociate the Li^+-EO_x and Li^+-$[TFSI]^-$ associations, which is suggested by RDF and association number analysis (Figures 3.6, 3.7 and 3.9). They also decrease the total average association number of Li^+ (N_{total}, shown in Figure 3.9). Moreover, they reduce the stability of remaining Li^+-EO_x and Li^+-$[TFSI]^-$ associations (Figure 3.14). These effects could help increase the diffusion ability of Li^+ in the EO-based electrolytes.

The overall influence of ZW molecules on Li^+ transport should be the synergistic consequence of the accelerating and decelerating effects. The accelerating effect is due to the ability of ZW molecules to dissociate Li^+-EO_x associations. The decelerating effect is due to Li^+-ZW associations. Indeed, the decelerating effect of ZW molecules may dominate in these four EO_x based electrolytes since D_{Li+} decreases with the presence of ZW molecules (Figure 3.3). However, as shown in Figure 3.4, the decrease of D_{Li+} narrows as the length of EO_x molecules increases. The ability of ZW molecules to accelerate Li^+ transport should enhance with longer EO_x chain length. This trend may be due to the ability of EO_x molecules to trap Li^+. The residence curves in Figure 3.14 indicate that the stability of the Li^+-O(EO_x) association enhances with the EO_x chain length increase. The more stable the Li^+-O(EO_x) associations are, the higher the impact is to dissociate them.

3.3.6 Conclusion

This work investigates the effect of ZW molecules on ionic associations and transport in EO-based electrolytes using MD simulations. We investigate the structural and

dynamic properties of ionic associations and diffusion of ions and molecules in 12 electrolytes composed of LiTFSI, EO_x (x=2,3,4 and 5) and ZW molecules possessing cationic imidazolium and anionic sulfonate groups. The simulation results show that the presence of ZW molecules dissociates the majority of Li^+-EO_x and Li^+-$[TFSI]^-$ associations and weakens those remaining. This effect is due to the strong ability of ZW molecules to associate with Li^+. It helps release Li^+ from the trapping effect due to the multiple-O associations of EO_x molecules and accelerates Li^+ transport. However, the strong Li^+-ZW associations could slow down Li^+ transport themselves. The competition between these two effects relates to the length of EO_x chains. The accelerating effect enhances as EO_x chain length increases, suggesting that ZW molecules may be able to contribute to increasing ionic conductivity of electrolytes composed of long PEO chains.

CHAPTER 4. DISTINCT EFFECT OF ZWITTERIONIC MOLECULES ON IONIC SOLVATION IN (ETHYLENE OXIDE)$_{10}$: A MOLECULAR DYNAMICS SIMULATION STUDY

4.1 Introduction

Ion-containing polymers refer to those composed of polymer chains and a salt. They serve as electrolytes or conducting materials in energy or sensing applications[118,119]. Ionic solvation plays a critical role in determining the performance of ion-containing polymers[120–126]. Thus, regulating ionic solvation turns out to be an efficient approach to manipulate polymer performance. ZW molecules have both cationic and anionic groups while staying charge-neutral[21,23,56,58,127]. This unique structure enables them to coordinate with cations, anions, and even among themselves[24–26,59]. Small zwitterionic (ZW) molecules have emerged as additives that can regulate the ionic solvation in ion-containing polymers[27,29,132–134,55–57,61,128–131].

One open question is how the chemical structures of ZW molecules affect their ability to regulate ionic solvation in polymers such as poly(ethylene oxide) (PEO). The solvation of Li^+ is the balance between Li^+-anion and Li^+-PEO coordination[135–139]. The presence of ZW molecules breaks the original balance and reformat a new balance among Li^+-anion, Li^+-PEO and Li^+-ZW coordination[135]. The chemical structure of ZW molecules affects their ability to break the original balance and form the new balance. We could optimize Li^+ solvation by selecting suitable ZW molecules if we understand the mechanisms governing the relationship between chemistry of zwitterionic molecules and their ability to regulate ionic solvation in polymers.

Simulation studies have been providing insights into the ability of ZW molecules to regulate ionic solvation. ZW molecules have strong interactions with Li^+[24,140,141]. These strong interactions weaken Li^+-anions coordination and enhance ionic mobilities in ionic liquid electrolytes[129,141]. ZW molecules can dissociate Li^+ from PEO polymer chains, which mitigates the low Li^+ transference number (t_{Li+}) (often in the range of 0.1–0.2[108,109]).

Our previous study[135] showed that ZW molecules containing cationic imidazolium and anionic sulfonate groups release Li^+ from the wrapping effect of EO chains and accelerate Li^+ transport in LiTFSI/EO_x (x=2-5) systems (LiTFSI: lithium bis(trifluoromethylsulfonyl)-imide). However, the ZW-Li^+ coordination decelerates the Li^+ transport if the coordination is too strong. The competition between the accelerating and decelerating effects was related to the length of EO chains: the accelerating effect enhanced as EO chain length increased.

Functional ZW molecules and ZW polymers have been synthesized from ionic liquids (ILs) as electrolyte materials[56]. As there are hundreds of commercially available ILs, the number of possible ZW structural designs is multitudinous. In addition, the polymerization of ZW monomers offers more space to design ZW materials[56]. There have been efforts to understand the relationship between ZW structures and their ability to affect ionic transport. Narita et al. [72] investigated the effect of ZW cationic groups on the ionic conductivity of the LiTFSI/ZW mixture. The ionic conductivity of ZW with the N-methylpyrrolidinium cationic group was lower than that of ZW with the N-ethylimidazolium cationic group. They also found that the design of ZW molecules with one carbon spacer was not effective in dissociating Li^+ from $[TFSI]^-$. Panzer group[30] studied the impact of different ZW chemical structures on Li^+ self-diffusion and conductivity in polyzwitterion-supported gels of LiTFSI/EO_5. Among the four ZW homopolymers, they found that poly(CBMA) scaffold resulted in the largest Li^+ self-diffusion coefficient and conductivity at room temperature (the four ZW homopolymers: poly(carboxybetaine methacrylate) (poly(CBMA)), poly(2-methacryloyloxyethylphosphorylcholine) (poly(MPC)), poly(sulfobetaine vinyl imidazole) (poly(SBVI)), and poly(sulfobetaine 2-vinylpyridine) (poly(SB2VP)). In another investigation on ZW structural design, Segalman and co-workers[31] reported ZW polymer electrolytes with the superionic conductivity behaviour (decoupling of ion motion and polymer segmental rearrangement) and $t_{Li+} \approx 0.5-0.7$ by using the pendant ZW

imidazolium-trifluoromethanesulfonamide for weaker Coulomic interactions. These promising results give rise to a quest for a general designing methodology of ZW electrolytes. To achieve that goal, it is crucial to have a better fundamental understanding of the relationship between different ZW structural designs and the effect on ionic coordination and transport in electrolytes.

We plan to investigate the influence of the chemical composition of ZW molecules on their ability to regulate Li^+ solvation in polymers using molecular dynamics (MD) simulations. This work will use the LiTFSI/EO_{10} mixtures as the model system. We select three ZW molecules: (1) 2-methacryloyloxyethyl phosphorylcholine (MPC), (2) sulfobetaine ethylimidazole (SB), and (3) carboxybetaine ethylimidazole (CB). MPC molecule has anionic phosphate and cationic trimethylazaniumyl groups with a carbon spacer of two methylene groups. SB and CB molecules have the same cationic imidazolium group and carbon spacer of three methylene groups while different anionic groups (carbonate group for CB and sulfonate group for SB). We study LiTFSI/EO_{10} and LiTFSI/EO_{10}/ZW systems at two Li^+:O(EO_{10}) molar ratios (r) = 1:6 (case-A) and 1:18 (case-B). These two molar ratios are used to model the systems at high and low Li^+ concentrations. The Li^+ concentration is 2.3 mol/L in case-A systems and 1.1 mol/L in case-B systems. In both cases, LiTFSI/EO_{10}/ZW systems have the ZW: Li^+ molar ratio of 1:5.

The reported research[135] has shown that it will need an extremely long molecular simulations to record Li^+ coordination formation and break at the room temperature. A practical approach is to increase system temperature[140,142]. Thus, we lift the simulation temperature up to 600 K during data collection to accelerate the mobility of ions and molecules in the system. This temperature increase enables us to observe the coordination formation and break during certain simulation times. The more simulation details are in section 4.2.2 The rest of the paper is as follows: Section 4.2 describes the molecular model

and simulation detail; Section 4.3 presents the results and discussion, and Section 4.4 presents the conclusion.

4.2 Methods

4.2.1 Molecular Models

This work uses the all-atom model to describe all ions and molecules. Figure 4.1 shows the structures of three ZW molecules, $[TFSI]^-$ ions and EO_{10} molecules used in this work. The nonbonded potential is a sum of the short-range Lennard-Jones 12-6 potential and long-range Coulomb potential (equation 4.1).

$$E = \sum_i \sum_{j<i} \left\{ \frac{1}{4\pi\varepsilon_0} \frac{q_i q_j e^2}{r_{ij}} + 4\varepsilon_{ij} \left[\left(\frac{\sigma_{ij}}{r_{ij}} \right)^{12} - \left(\frac{\sigma_{ij}}{r_{ij}} \right)^{6} \right] \right\} \tag{4.1}$$

where r_{ij} is the distance between atom i and j, q_i and q_j are the partial charges of atom i and j, ε_0 is the free space permittivity, and ε_{ij} and σ_{ij} are energetic and geometric parameters. The bonded potential is a sum of the bond, angle, and dihedral-angle potentials. The OPLSAA/MM force field was used to describe the bonded and nonbonded interactions in the system. The force field parameters were assigned using the Ligpargen web server[143]. Table C1 lists the nonbonded force field parameters used in this work.

This work prepares the initial simulation systems by randomly placing certain numbers of Li^+, $[TFSI]^-$, EO_{10} molecules and ZW molecules in a cubic box. Table C2 lists the details of the eight simulation systems. The initial configurations were prepared using Packmol[83]. Figure 4.2 shows the initial configuration of a simulation box containing 100 Li^+, 100 $[TFSI]^-$, 20 SB molecules and 180 EO_{10} molecules.

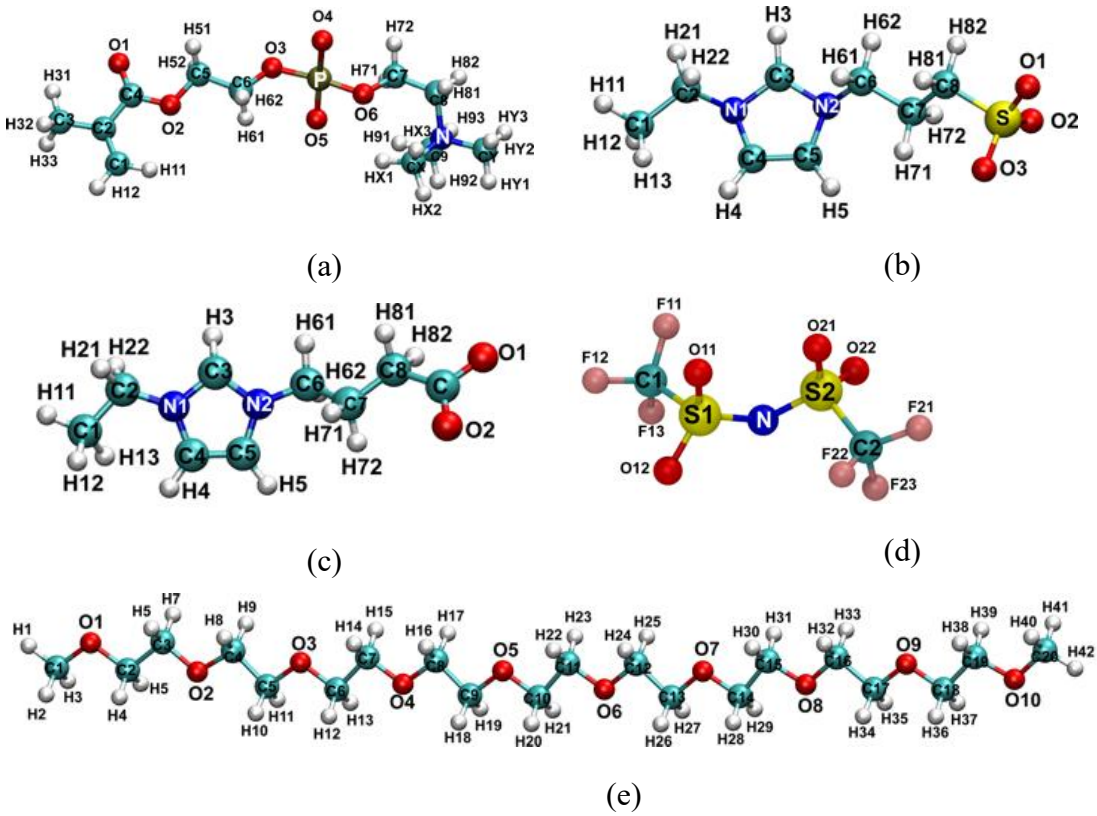

Figure 4.1. Molecular structures of (a) MPC, (b) SB, (c) CB, (d) $[TFSI]^-$, and (e) EO_{10}. Every atom is labeled with a unique name. Atom color code: hydrogen (silver), carbon (cyan), nitrogen (blue), oxygen (red), sulfur (yellow).

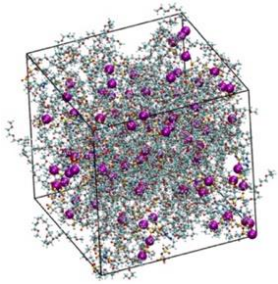

Figure 4.2. The initial configuration of a simulation box containing 100 Li^+, 100 $[TFSI]^-$, 20 SB molecules and 180 EO_{10} molecules. Li^+ ions are represented using the VDW model with purple color and the others are represented by the CPK model with the same color code in Figure 4.1. This figure was generated using VMD-1.9.1[84]

4.2.2 Simulation Details

The simulation process includes six steps. First, energy minimization was conducted to eliminate too close contacts between atoms. Second, a 100-ns isothermal-isobaric (NPT) MD simulation was conducted at 500 K and 100 kPa to relax the system fully. Third, a 200-ns NPT simulation was conducted at 353 K and 100 kPa followed by the fourth 1000-ns canonical (NVT) simulation at 353K. Fifth, a 200-ns NVT simulation was conducted at 600 K to let the system reach the desired temperature. Sixth, a 1000-ns canonical (NVT) MD simulation was conducted at 600 K for data collection at a frequency of 5-ps. The combination of step three to six ensures that the simulated ion-containing polymer systems approximate the desired density at 353K. Meanwhile, the mobility of ions and molecules in the systems are accelerated by a high temperature (600 K), enabling us to observe the structural and dynamic properties of the system better within a reasonable simulation time (1000 ns). The Berendsen method[88] was used to control the temperature and pressure in the second, third and fifth steps because it enables the system to reach the controlled temperature and pressure at a fast pace. The velocity-rescaling method[89] was used to control the system temperature in the fourth and sixth step. The short-range potential energies were calculated using a 1.0-nm cut-off, while the long-range electrostatic interaction energy was calculated using the particle mesh Ewald sum[90]. All bonds involving hydrogen atoms were constrained during the fourth step using the LINCS algorithm[91]. The energy minimization and MD simulations were conducted using Gromacs 2021[92]. We repeat the simulation process three times for each system with different initial configurations.

4.2.3 Sigma profile calculation

We follow the procedure provided by Mullins et al[144] to generate sigma (σ) profiles. First, we optimize molecular geometry and perform conductor-like screening

models (COSMO) calculation to generate surface charge densities at B3LYP/6-311++G(d,p) level of theory using Gaussian software[145]. The COSMO model conceptually places a molecule in a cavity and into a conducting medium, where the molecule draws charges from the conductor to the cavity surface to neutralize both the electric field within the conductor and tangential to the surface[144,146]. The cavity surface is divided into n segments. To generate σ profile, the surface-charge densities from the COSMO output are averaged using the equation 4.2:

$$\sigma_{\mathrm{m}} = \frac{\sum_n \sigma_n^* \frac{r_n^2 r_{\mathrm{av}}^2}{r_n^2 + r_{\mathrm{av}}^2} \exp\left(-\frac{d_{mn}^2}{r_n^2 + r_{\mathrm{av}}^2}\right)}{\sum_n \frac{r_n^2 r_{\mathrm{av}}^2}{r_n^2 + r_{\mathrm{av}}^2} \exp\left(-\frac{d_{mn}^2}{r_n^2 + r_{\mathrm{av}}^2}\right)} \qquad (4.2)$$

Where σ_m is the average surface-charge density on segment m, σ_n* is surface-charge density for segment n with the radius r_n from the COSMO output, d_{mn} is the distance between the two segments m and n, r_{av} is the averaging radius (0.818 Å), which makes the averaging segment surface area $A_{av} = \pi r^2_{av} = 2.100$ Å^2. [144,146,147]

The σ profile is defined as:

$$\rho(\sigma) = \frac{A(\sigma)}{A} \qquad (4.3)$$

$$\mathrm{A}(\sigma) = n(\sigma) A_{av} \qquad (4.4)$$

$$A = n A_{av} \qquad (4.5)$$

where A(σ) represents the total surface area of n(σ) segments with the charge density σ, A is the total cavity surface area of all surface segments n. [144,146]

4.3 Results and Discussion

4.3.1 Radial Distribution Functions (RDFs)

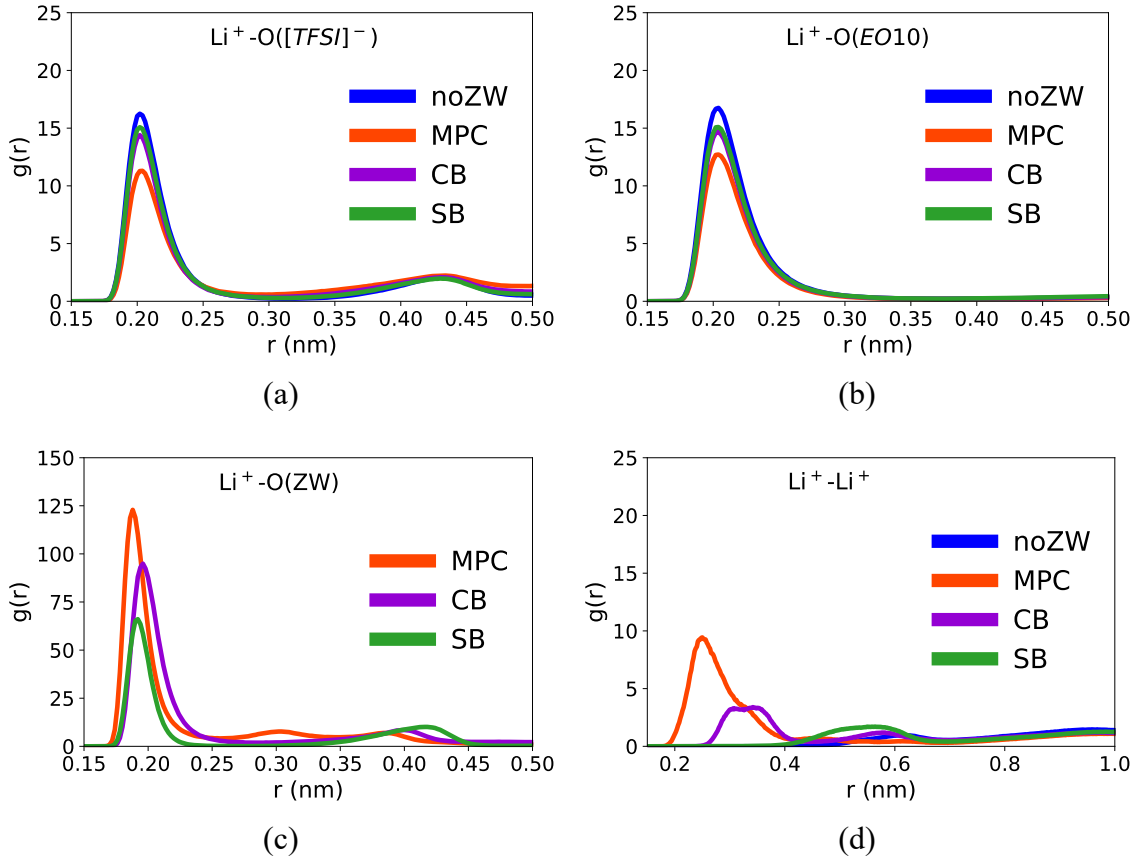

Figure 4.3. RDFs of (a) Li^+-O([TFSI]$^-$), (b) Li^+-O(EO_{10}), (c) Li^+-O(ZW) and (d) Li^+-Li^+ in case-A systems.

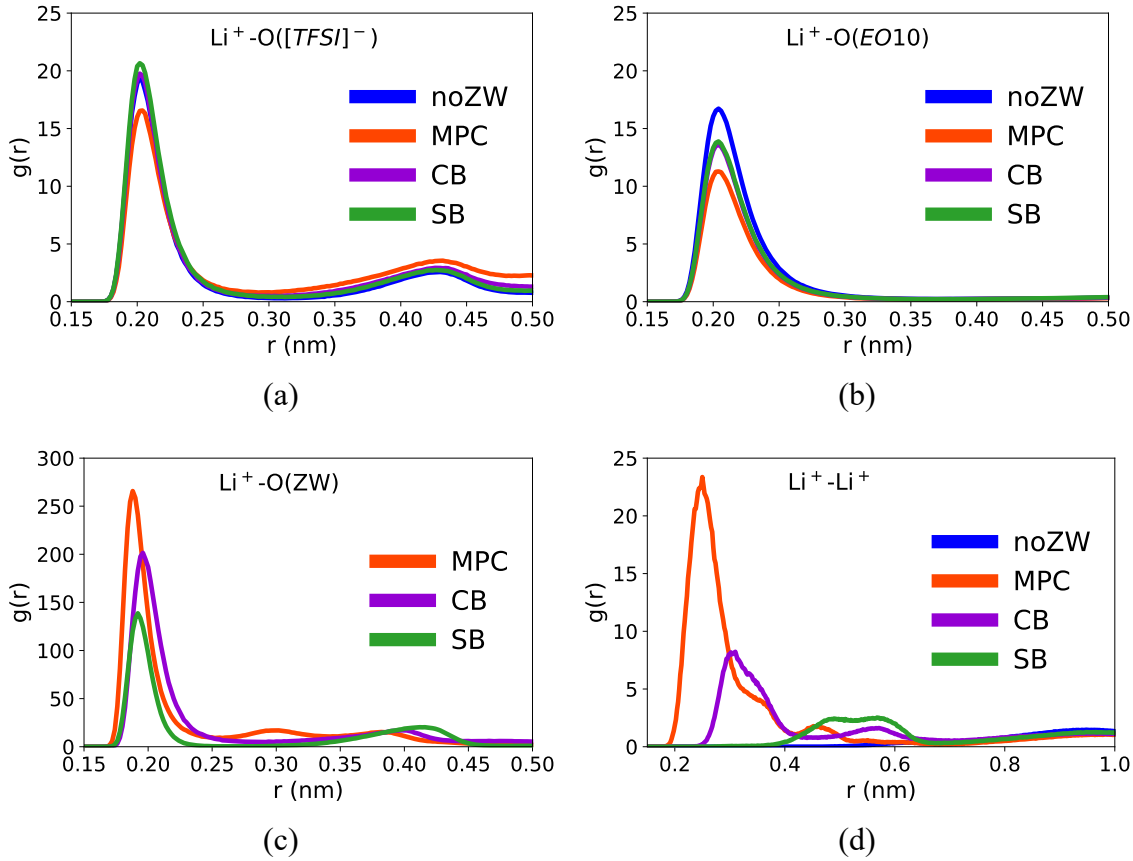

Figure 4.4. RDFs of (a) Li^+-O([TFSI]$^-$), (b) Li^+-O(EO_{10}), (c) Li^+-O(ZW) and (d) Li^+-Li^+ in case-B systems.

To investigate the effect of ZW molecules on Li^+ coordination preference, we analyze the radial distribution functions (RDFs) of Li^+-O([TFSI]$^-$), Li^+- O(EO_{10}), and Li^+-O(ZW) in the eight electrolyte systems. O([TFSI]$^-$) refers to all four O atoms on the [TFSI]$^-$ molecule. O(EO_{10}) refers to all ten O atoms on the EO_{10} molecule. O(ZW) refers to O3, O4, O5, and O6 atoms on the MPC molecule, O1 and O2 atoms on the CB molecule, and O1, O2, and O3 atoms on the SB molecule (Figure 4.1). Figures 4.3 and 4.4 show the Li^+-O([TFSI]$^-$), Li^+-O(EO_{10}), and Li^+-O(ZW) RDFs in the case-A and case-B electrolytes. All RDFs have a high peak located around 0.2 nm, consistent with literature[117,140,141]. The high RDF peaks indicate that Li^+ ions coordinate with [TFSI]$^-$, EO_{10} and ZW molecules.

Among the three ZW structures, MPC shows the strongest effect to decrease the preference of Li^+ to coordinate with $[TFSI]^-$ and EO_{10}. As shown in Figures 4.3a and 4.3b, the RDF peak heights of Li^+-O($[TFSI]^-$) and Li^+-O(EO_{10}) decrease from 16 to 11 with MPC, whereas to around 15 with SB and CB in the case-A systems. The case-B systems present similar phenomena. As shown in Figure 4a and 4b, MPC decreases the peak heights of Li^+-O($[TFSI]^-$) and Li^+-O(EO_{10}) RDFs by 15% and 35% respectively, while SB and CB leave Li^+-O($[TFSI]^-$) RDFs unaffected and only reduce the Li^+-O(EO_{10}) RDF peak heights by 18%. The effect of SB on Li^+ coordination preference is much less than what was previously reported[135]. We attribute this to the low ZW: Li^+ molar ratio. Our previous study[135] showed that SB caused RDF peak heights of Li^+-$[TFSI]^-$ and Li^+-EO_5 to drop less than half with SB: Li^+ molar ratio of 1:1 in SB/LiTFSI/EO_5 electrolytes at Li^+:O(EO_{10}) molar ratio of 1:6. The higher reduction of these RDF peak heights suggests the better ability of MPC to reduce Li^+ coordination with $[TFSI]^-$ and EO_{10}.

Li^+ prefers to coordinate with MPC more than CB and SB, allowing MPC to release Li^+ from the coordination with $[TFSI]^-$ and EO_{10} better. Figures 4.3c and 4.4c show that RDF peak heights of Li^+-O(ZW) follow the order: MPC > CB > SB. RDF peak heights of Li^+-O(MPC), Li^+-O(CB), and Li^+-O(SB) are 123, 95, and 66 in case-A systems and 266, 201, and 139 in case-B systems, respectively. This difference in Li^+-O(ZW) RDFs might be due to the partial charges and geometry of ZW molecules. Table C1 shows that O atoms of the phosphonate group on MPC have higher partial charges than those of the sulfonate group on SB and carbonate group on CB, consistent with literature[36]. The higher partial charges of O atoms may improve the coordination preference of Li^+ with MPC. Even though O(CB) has a partial charge similar to O(SB), the geometry of the carboxylate group on CB might make it easier for Li^+ to coordinate with CB.

ZW causes Li^+ ions to form indirect pairs. As shown in Figures 4.3d and 4.4d, the RDF Li^+-Li^+ peaks are enhanced when ZW is added in both case-A and case-B systems. The RDF peak heights are in the order: MPC > CB > SB. The order of Li^+-Li^+ RDF peak

heights is consistent with that of Li^+-ZW RDFs (Figures 4.3c and 4.4c). In addition, Li^+-Li^+ and Li^+-ZW RDF peaks are higher in case-B than case-A. The strong preference of Li^+ to coordinate with ZW might cause Li^+ to aggregate around ZW. ZW molecules act as "bridges" for Li^+ to indirectly pair with themselves. Such Li^+-Li^+ pairing was also reported in the literature[148–152].

4.3.2 Coordination Number

Tables 4.1 and 4.2 show the coordination numbers of Li^+-O(EO_{10}), Li^+-O($[TFSI]^-$), Li^+-O(ZW), and their sum in case-A and case-B systems. The coordination numbers were calculated by numerically integrating the corresponding RDFs within a threshold (Li^+-O(EO_{10}): 0.35 nm, Li^+-O($[TFSI]^-$): 0.29 nm, Li^+-O(ZW): 0.27 nm). The number of Li^+-O(EO_{10}) coordination is the highest. For example, Table 4.1 shows that a Li^+ ion coordinates with 2.8 O atoms from EO_{10}, 1.4 O atoms from $[TFSI]^-$], and 1.7 O atoms from MPC molecules on average in case-A electrolytes. The coordination numbers of Li^+-O also follow the same order in case-B electrolytes (Table 4.2). Even though Li^+ has the highest preference to coordinate with ZW (Figures 4.3 and 4.4), the coordination number of Li^+-O(ZW) is lower than that of Li^+-O(EO_{10}), which might be due to the low ZW: Li^+ molar ratio. In our previous report[135], the Li^+-O(SB) coordination number is the highest in the SB/LiTFSI/EO_5 electrolyte with SB: Li^+ molar ratio of 1:1 and Li^+:O(EO_{10}) molar ratio of 1:6.

Table 4.1. Coordination numbers of Li^+-O in case-A systems

	No ZW	MPC	CB	SB
Total	6.02 ± 0.02	5.87 ± 0.11	5.81 ± 0.01	5.71 ± 0.02
Li^+-O(ZW)	N/A	1.69 ± 0.02	0.82 ± 0.01	0.60 ± 0.01
Li^+-O($[TFSI]^-$)	1.94 ± 0.01	1.37 ± 0.04	1.61 ± 0.01	1.67 ± 0.01
Li^+-O(EO_{10})	4.07 ± 0.01	2.81 ± 0.04	3.38 ± 0.01	3.45 ± 0.01

Table 4.2. Coordination numbers of Li^+-O in case-B systems

	No ZW	MPC	CB	SB
Total	6.35 ± 0.01	6.07 ± 0.03	6.04 ± 0.01	5.95 ± 0.01
Li^+-O(ZW)	N/A	1.64 ± 0.05	0.80 ± 0.01	0.58 ± 0.01
Li^+-O($[TFSI]^-$)	0.98 ± 0.01	0.93 ± 0.06	1.00 ± 0.01	1.04 ± 0.01
Li^+-O(EO_{10})	5.37 ± 0.01	3.50 ± 0.13	4.24 ± 0.02	4.33 ± 0.01

Among three ZW structures, MPC reduces the Li^+-O($[TFSI]^-$) and Li^+-O(EO_{10}) coordination the most. Table 4.1 shows that the coordination number of Li^+-O(EO_{10}) decreases by 30% with MPC and only by around 16% with SB and CB addition in case-A systems. Similarly, the reduction in the Li^+-O($[TFSI]^-$) coordination number is highest with MPC addition at the same Li^+ concentration (MPC: -29%; CB: -17%; SB: -14%). The same trend was also observed in case-B electrolytes. Table 4.2 shows that both coordination numbers of Li^+-O(EO_{10}) and Li^+-O($[TFSI]^-$) also decrease the most with the presence of MPC. It is noted that while ZW:O(EO_{10}) ratio in case-B (5:18) is less than case-A (5:6), ZW remains effective in reducing Li^+-O(EO_{10}) coordination (MPC: -35%, CB: -21%, SB: -20%). However, due to the lower ratio of ZW:O(EO_{10}) in case-B (lower ZW concentration), ZW has a smaller effect on the coordination number of Li^+-O($[TFSI]^-$) (MPC: -5%, CB: +2%, SB: +6%). The reduction in the Li^+-O($[TFSI]^-$) and Li^+-O(EO_{10}) coordination numbers is consistent with the RDF results. MPC is more effective than SB and CB in reducing Li^+ coordination with $[TFSI]^-$ and EO_{10}, which is correlated with the higher preference of Li^+ to coordinate with MPC.

The Li^+-O(ZW) coordination numbers are ranked in the order: MPC > CB > SB. As shown in Tables 4.1 and 4.2, the coordination numbers of Li^+-O(MPC), Li^+-O(CB), and Li^+-O(SB) are 1.7, 0.8, and 0.6, respectively in case-A and case-B systems. This trend in Li^+-O(ZW) coordination numbers is consistent with the corresponding RDF peak heights. The higher number of Li^+-O(MPC) coordination explains the larger decrease of Li^+-O($[TFSI]^-$) and Li^+-O(EO_{10}) coordination numbers with MPC addition compared to CB

and SB. CB has slightly higher Li^+-O(ZW) coordination numbers than SB, correlated with CB's better dissociating effect on the Li^+-O($[TFSI]^-$) and Li^+-O(EO_{10}) coordination.

4.3.3 Percentage of Li^+ leaving the coordination with EO_{10} chains

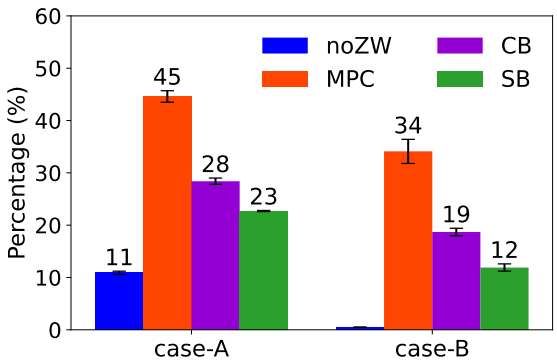

Figure 4.5. Percentage of Li^+ not coordinating with EO_{10}

MPC presents the strongest ability to fully release Li^+ from coordinating with EO_{10}. Our previous study[135] showed that the ability of ZW to release Li^+ from the wrapping of EO chains helps enhance Li^+ transport in PEOs. In this study, we investigate the effect of the three ZW molecules on this dissociation ability with Li^+-EO coordination. Tables 4.1 and 4.2 show that the average number of Li^+-O(EO_{10}) coordination decreases by 15-35% with the presence of ZW. Such decrease could be due to two aspects. First, Li^+ still coordinate with PEO chains but with less O atoms. Second, Li^+ do not coordinate with PEO chains anymore. The first scenario may just partially release Li^+ from the PEO chains while the second scenario fully releases Li^+ from the PEO chains. To analyze these two aspects, we calculate the percentage of Li^+ ions that do not coordinate with O(EO_{10}) in the eight systems (Figure 4.5). As shown in Figure 4.5, the percentage of Li^+ not coordinating with EO_{10} increases from 11% to 45% in the case-A system with MPC. The presence of MPC causes almost half of Li^+ not coordinate with the EO_{10} chains. The CB and SB also present a similar but weaker ability to fully release Li^+ from coordinating with EO_{10} chains. Around 30% of Li^+ do not coordinate with EO_{10} chains with the presence of CB. SB releases Li^+

from coordination with EO_{10} the least (only 23%). The case-B system presents a similar trend for the three ZW molecules regarding their ability to fully release Li^+ from EO_{10} chains.

MPC can exclude EO_{10} and $[TFSI]^-$ from the solvation shell of Li^+. Table 4.3 shows that the percentage of Li^+ only coordinating with ZW. The percentage is 9% and 13% for MPC in the case-A and case-B systems, respectively, whereas there is no exclusive Li^+-ZW coordination for SB and less than 5% for CB. This type of structural exclusion by ZW is also reported in simulations of Keith et al.[140] for LiTFSI salt-doped polymerized ZW composed of imidazolium cationic and triflate-like anionic moieties.

Table 4.3. Percentage of Li^+ only coordinating with ZW

ZW structures	Systems	
	Case-A	Case-B
MPC	9±1%	13±2%
SB	0%	0%
CB	2±1%	4±1%

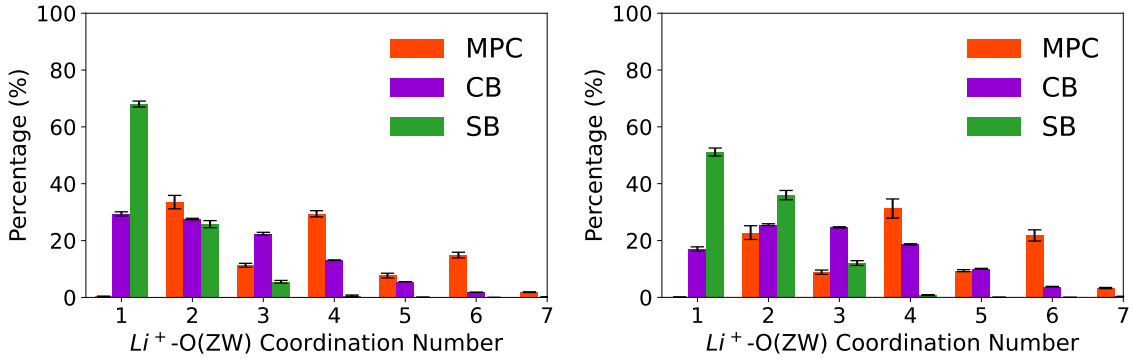

(a) (b)

Figure 4.6. Distribution of Li^+-O(ZW) coordination number in (a) case-A and (b) case-B systems.

Li^+ ions coordinate with multiple O atoms from MPC more than SB and CB. Figure 4.6 shows the distribution of Li^+-O(ZW) coordination number in case-A and case-B systems. The Li^+-O(ZW) coordination numbers are categorized by the number of O atoms

on ZW that a Li^+ ion coordinates with. As shown in Figure 4.6, MPC has the highest percentage of Li^+ coordinating with more than one O atom from ZW in both cases. For instance, 100% of Li^+ ions coordinate with more than one O from MPC, while that percentage is 70%, and 30% for CB and SB respectively in case-A electrolytes. The same trend is also observed in Case-B electrolytes (Figure 4.6b). In addition, this ranking order in Li^+ coordinating with multiple O(ZW) is reflected in the average Li^+-O(ZW) coordination number (MPC > CB > SB, as shown in Tables 4.1 and 4.2). The high preference of Li^+ to coordinate with multiple O atoms on MPC might be responsible for excluding EO_{10} and $[TFSI]^-$ from the solvation shell of Li^+ when MPC is present. Figure 4.7 shows simulation snapshots as examples of the different morphology of Li^+-ZW coordination for MPC, CB and SB.

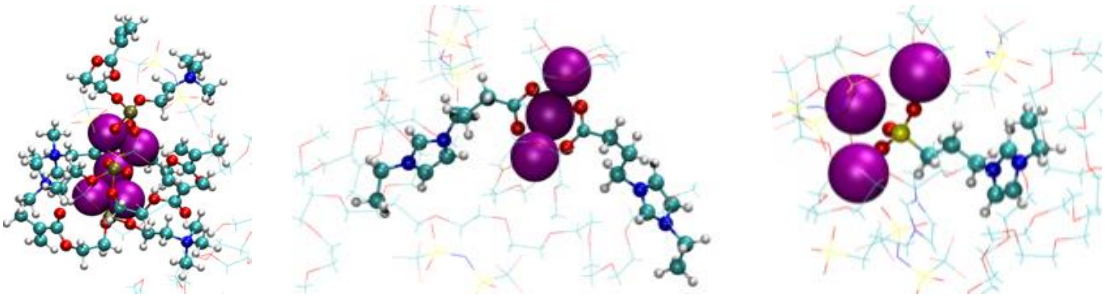

(a) (b) (c)

Figure 4.7. Snapshot of (a) 4 MPC coordinating with 5 Li^+, (b) 2 CB coordinating with 3 Li^+, and (c) 1 SB coordinating with 3 Li^+ in case-A system. (Li^+ ions are represented using the VDW model with purple color; ZW molecules are displayed with the CPK model; $[TFSI]^-$ and EO_{10} molecules are displayed using the line model with the same color code in Figure 4.1).

4.3.4 Li^+ coordination lifetime

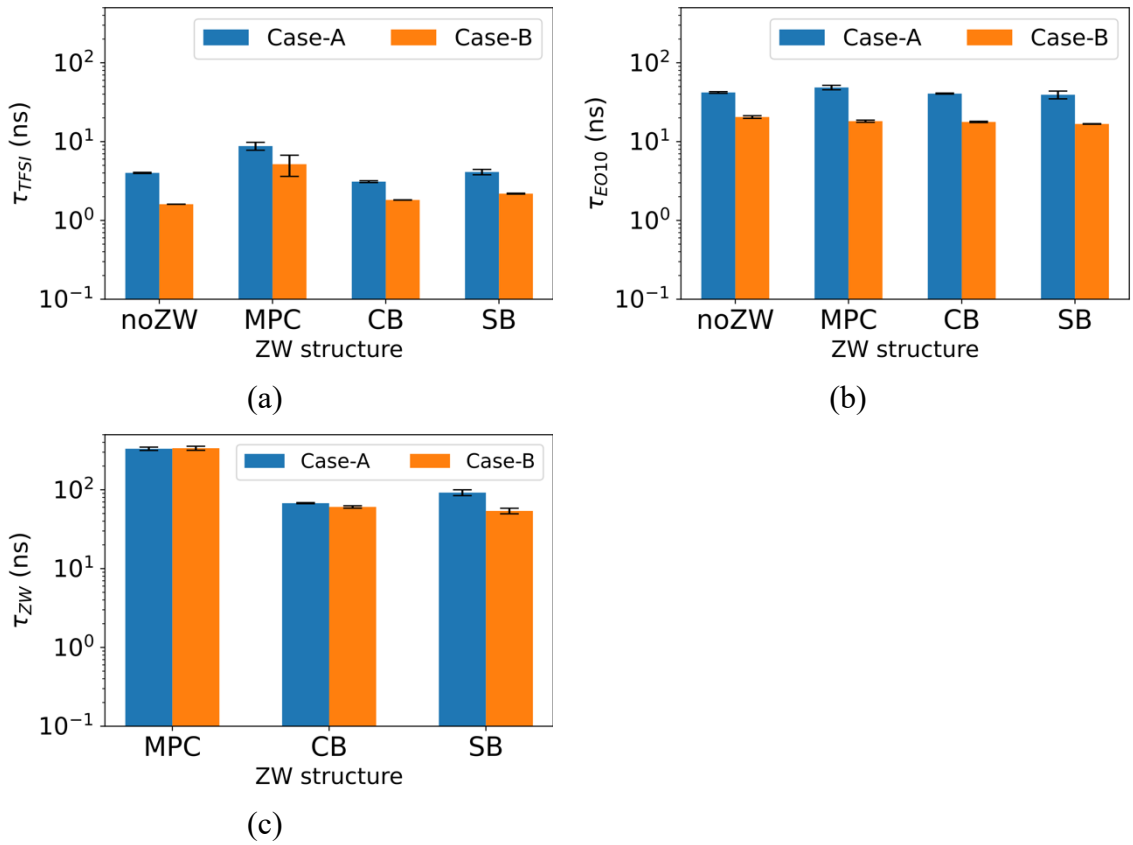

Figure 4.8. Lifetime of Li^+-O coordination in case-A and case-B systems: (a) Li^+-O([TFSI]$^-$), (b) Li^+-O(EO_{10}), and (c) Li^+-O(ZW).

We analyze the stability of the Li^+-O(EO_{10}), Li^+-O([TFSI]$^-$) and Li^+-O(ZW) coordination based on their lifetime (τ_{EO10}, τ_{TFSI}, and τ_{ZW} respectively). A coordination with higher τ is more stable. The values of τ were calculated by integrating the coordination residence curves (C(t)) (equation 4.6).

$$C(t) = \frac{1}{N_0}\sum_{j=0}^{N_0}\frac{\langle P_j(0)P_j(t)\rangle}{\langle P_j(0)\rangle^2} \qquad (4.6)$$

where N_0 is the total number of certain coordination at $t = 0$ and $P_j(0) = 1$. At time t, $P_j(t) = 1$ if the coordination j still exists and $P_j(t) = 0$ if the coordination j breaks. Figure 4.8

shows value of τ_{LEO10}, τ_{TFSI}, and τ_{ZW} in the eight electrolytes. τ_{MPC} are not actual lifetime since C(t) of Li^+-O(MPC) coordination does not decay to zero after 500-ns. The corresponding residence C(t) curves are shown in Figures C1 and C2.

MPC slightly enhances the stability of Li^+-$[TFSI]^-$ coordination and Li^+-EO_{10} coordination, whereas CB and SB have no effect on both Li^+-$[TFSI]^-$ and Li^+-EO_{10} coordination stability. For instance, Figure 4.8a shows that τ_{TFSI} increases from 4-ns to around 9-ns with the presence of MPC in Case-A electrolytes, whereas τ_{TFSI} remains unvaried with CB and SB addition. Figure 4.8b shows that τ_{EO10} remains around 42-ns in systems with and without ZW molecules. Case-B electrolytes present the same phenomenon. The increased coordination stability of Li^+-$[TFSI]^-$ might have adverse effect on Li^+ diffusion. However, τ_{TFSI} is less than τ_{EO10} and τ_{ZW} by more than one order of magnitude. Thus, the increase in Li^+-$[TFSI]^-$ lifetime might not affect Li^+ mobility significantly.

ZW-Li^+ coordination is the most stable among the three types of Li^+ coordination. Figure 4.8 shows that τ_{ZW} is higher than τ_{TFSI} and τ_{EO10} in both cases. For example, τ_{CB} is 67-ns, higher than τ_{EO10} (40-ns) and τ_{TFSI} (3-ns) with presence of CB in case-A. In case-B, the Li^+-O(CB) coordination is also more stable than the Li^+-O(EO_{10}) and Li^+-O($[TFSI]^-$) coordination (τ_{CB}: 61-ns; τ_{EO10}: 18-ns; τ_{TFSI}: 2-ns). Case-B also has the same phenomenon. The higher lifetime of Li^+-ZW compared to that of Li^+-EO_{10} and Li^+-$[TFSI]^-$ is correlated with the higher preference of Li^+-ZW coordination. Among the three ZW structures, the Li^+-MPC is the most stable, which is correlated with the strongest preference of Li^+ to coordinate with MPC. Li^+-CB is less stable than Li^+-SB in case-A but comparable to Li^+-SB in case-B. Figure 4.8c shows that τ_{CB} is 35% smaller than τ_{SB} in case-A but only ~10% larger than τ_{SB} in case-B systems. The introduction of strong and stable Li^+-ZW might lead to slowing down of Li^+ diffusion since ZW is larger than Li^+ in molecular size.

4.3.5 Diffusion coefficients

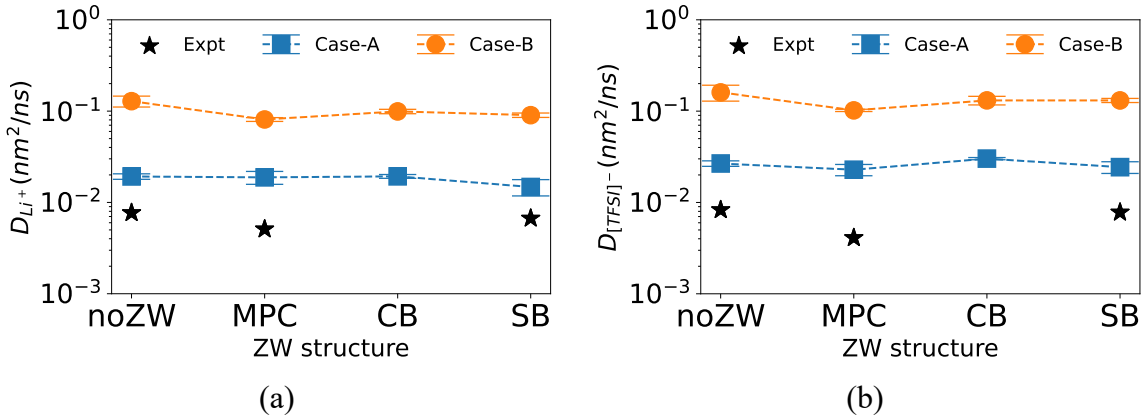

Figure 4.9. Diffusion coefficients of (a) Li^+, and (b) $[TFSI]^-$ at 600 K. Experimental values (Expt) of electrolytes comparable to case-A systems from the work of Panzer group at 293 K. [30]

Figure 4.9 shows the diffusion coefficients of Li^+ (D_{Li+}), and $[TFSI]^-$ ($D_{[TFSI]-}$) in the eight electrolytes. Details of diffusion coefficients of Li^+ (D_{Li+}), $[TFSI]^-$ ($D_{[TFSI]-}$) and ZW (D_{ZW}) are shown in Tables C3-5. The diffusion coefficients were calculated based on mean square displacement curves using the Einstein relation (equation 4.7).

$$D = \lim_{t\to\infty} \frac{1}{6t} \left\langle |\mathbf{r}(t) - \mathbf{r}(0)|^2 \right\rangle \qquad (4.7)$$

where $<|r(t) - r(0)|^2>$ is the mean square displacement of an atom or molecule species, r(t) is the position at time t and r(0) is the position at initial time 0. We also include the experimental values for D_{Li+}, and $D_{[TFSI]-}$ for electrolytes similar to our case-A systems from the work of Panzer group[30] LiTFSI/EO_5/polymeric ZW electrolytes with Li^+:O(EO_5) molar ratio of 1:5 and Li^+:ZW molar ratio of 1:6. We note that our simulation temperature of 600 K is much higher than the experimental temperature (293 K). Thus, we only make qualitive comparison between our results and experimental data.

SB decreases ionic diffusion, whereas the effect of MPC and CB is minute in case-A electrolytes. Figure 4.9a shows that D_{Li+} decreases by 25% from 0.019 to 0.015 nm^2/ns when SB is added while remains unvaried with the presence of MPC and CB in case-A

systems. Our result for SB system matches qualitatively with the experimental data. In the investigation conducted by Panzer group[30], D_{Li+} decreased by 13% and 34% with poly(SBVI) and poly(MPC) respectively, as shown in Figure 4.9a. ZW polymer scaffolds have slower dynamics than their small monomer molecules, which might be the reason of the higher decrease in the experimental data of D_{Li+} for poly(MPC) compared to our simulation result for MPC.

In case-B electrolytes, ZW slows the diffusion of Li^+ and $[TFSI]^-$ in the order: MPC > SB > CB. Figure 4.9a shows that D_{Li+} decreases from 0.129 to around 0.081, 0.090, 0.099 nm^2/ns when MPC, SB and CB are added respectively. At a similar Li^+ concentration to our case-B systems, a simulation study of C. Lourenço et al. [141] also observed a decrease in the Li^+ diffusivity in an IL electrolyte with 1M LiTFSI-[BMP][TFSI] due to the addition of MPC-co-SBVI oligomers ([BMP][TFSI]: N-butyl-N-methylpyrrolidinium bis(trifluoromethylsulfonyl)imide).

As ZW molecules release Li^+ from coordinating with EO_{10} by forming the more preferred Li^+-ZW coordination, we investigate the effect of this change in Li^+ coordination situation on Li^+ short-scale diffusion. We calculate the displacement distance travelled by the Li^+ cations that remain in a given coordination over a time period of 1-ns. Namely, we only consider the Li^+ cations that stay coordinated by a same number of O from ZW, EO_{10} or $[TFSI]^-$ between the selected time window. We estimate that only ~20% of Li^+ cations meet this criterion for the 1-ns time frame. Besides 1-ns time period, we also select 2-ns to show that the variation in time period still supports our conclusion about the effect of different Li^+ coordination on short-scale diffusion of Li^+ (Figure C3). Figure 4.10 shows the computed displacement by Li^+ ions as a function of Li^+-O coordination number (O from $[TFSI]^-$, EO_{10} and ZW) in Case-A electrolytes.

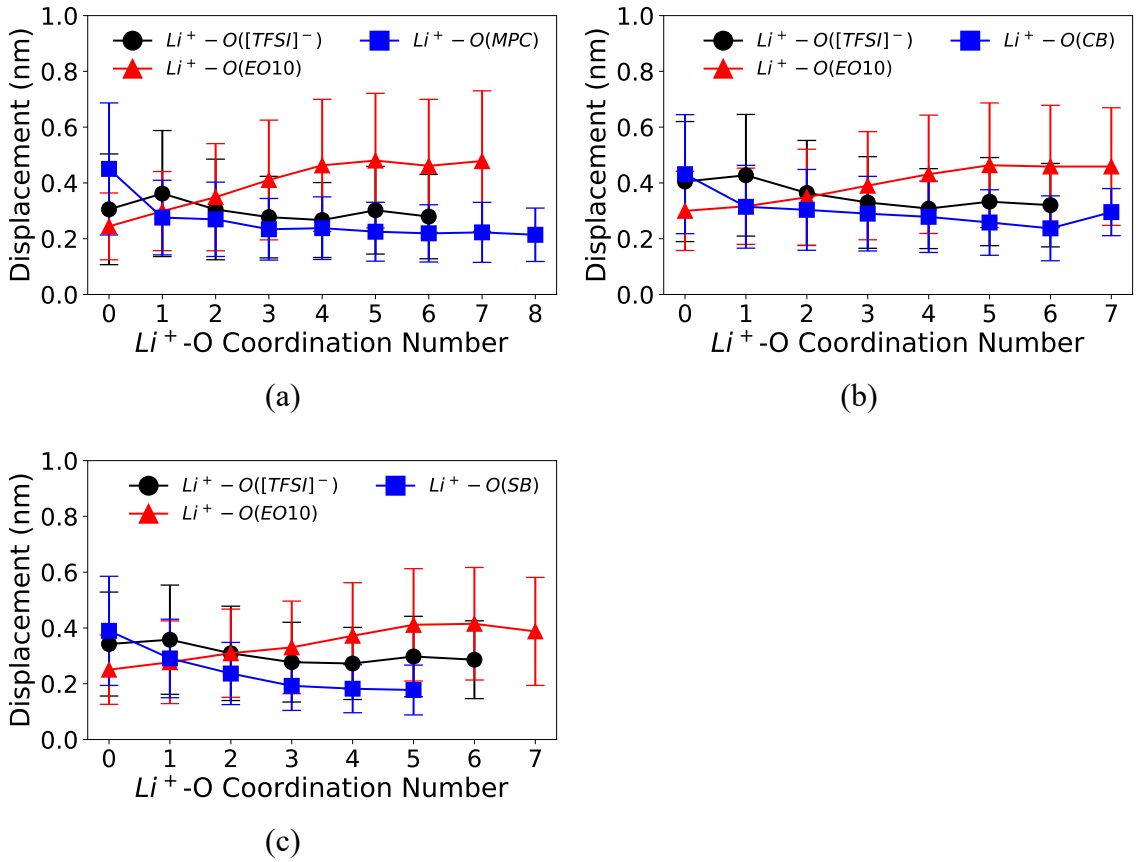

Figure 4.10. Distance travelled by Li^+ ions in a specific O coordination number over 1-ns for systems (a) with MPC, (b) with CB, and (c) with SB in case-A systems. The bars in the figures show the standard deviation.

Li^+-ZW interactions could slow down Li^+ mobility. As shown in Figure 4.10, the Li^+ displacement distance decreases sharply as soon as Li^+ coordinates with one O from ZW (Li^+-O(ZW) coordination number increases from zero to one). Li^+ also has slower short-scale motion with increased coordination with ZW or $[TFSI]^-$ than with EO_{10}. For example, Figure 4.10a shows that Li^+ coordinating with seven O(MPC) is ~100% slower than with seven O(EO_{10}). Likewise, Li^+ displacement distance decreases when Li^+ coordinates with O(CB) and O(SB) (Figures 4.10b and 4.10c). A similar finding was also reported in the computational work by Molinari et al. [153] for LiTFSI/EO_{100} at 4M Li^+ concentration: Li^+ coordinated by $[TFSI]^-$ has lower mobility by up to 40% than by EO_{100}. They found that the correlation of Li^+ displacement and Li^+-O($[TFSI]^-$) coordination number is due to LiTFSI clustering. In our study, ZW might form clusters with Li^+ and

thus decreases Li^+ short-time mobility. Case-B electrolyte also present the similar phenomenon (Figures C4 and C5). Figures C8-11 show the displacement distribution of Li^+ ions with specific Li^+-O coordination numbers.

The diffusion slowing effect of ZW might be offset by the Li^+-EO_{10} dissociation ability. Our previous study[135] on LiTFSI/ZW/EO_x (x = 2-5) systems found a competition of ZW's two effects. The first is the diffusion slowing effect due to the strong Li^+-ZW interactions. The second is the ability of ZW to dissociate Li^+ from PEO wrapping. This second effect decouples the mobility of Li^+ with that of polymers and may increase Li^+ ionic conductivity. The overall change in Li^+ conductivity should be the synergy of the two effects. Among the three ZW structures, MPC releases Li^+ from the Li^+-EO_{10} coordination the most (Figure 4.5 and Tables 4.1 - 4.2). However, the Li^+- MPC interaction is also the strongest (Figure 4.8). Further, only MPC can exclude other molecules from the coordination shell of Li^+ (Figure 4.3). The self-diffusion data shows that MPC has little effect on D_{Li+} in case-A, while decreasing D_{Li+} the most in case-B. In case-A, the diffusion-slowing effect of MPC might be offset by MPC's effective dissociation of Li^+-EO_{10}. Thus, the overall effect of MPC on Li^+ mobility is minute in case-A. Whereas, in case-B, MPC's slowing effect is the strongest. Similarly, it is plausible that the overall effect of CB on Li^+ diffusion is less than SB in both cases, where CB either has no effect (case-A) or lesser reduction of D_{Li+} than SB does (case-B). SB and CB have similar coordination numbers with Li^+ (Table 4.1 and 2). However, CB has better Li^+-EO_{10} dissociation effect than SB (Figure 4.5) and the stability of Li^+-CB is less than that of Li^+-SB in case-A or comparable to that of Li^+-SB in case-B (Figure 4.8), which might be the reason why CB has smaller overall effect on D_{Li+} than SB.

4.3.6 Radius of gyration of EO_{10}

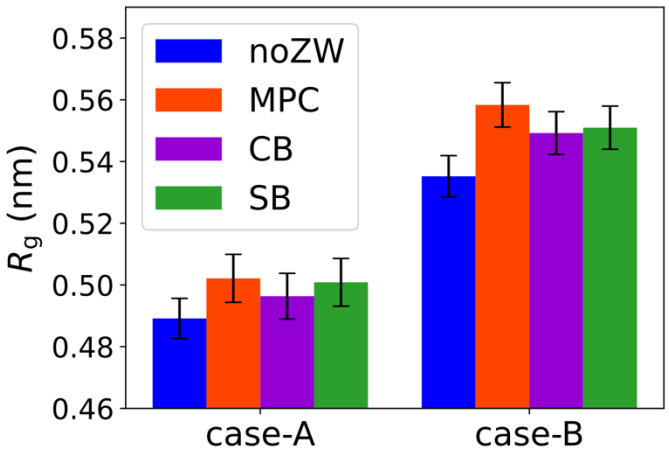

Figure 4.11. Radius of gyration (Rg) of EO_{10} chains in case-A and case-B systems.

ZW molecules can relax the coiling of EO_{10} chains. We analyze the EO_{10} conformation using radius of gyration (R_g), which characterizes the average coil size of EO_{10} chains. Figure 4.11 shows R_g of EO_{10} chains in the in case-A and case-B systems. As shown in Figure 4.11, R_g increases slightly due to addition of three ZW structures in both cases. The higher R_g correlates with the increased percentage of Li^+ ions leaving the coordination with EO_{10} chains (Figure 4.5). EO units in PEO wrap around Li^+, resulting in contraction of the chain[154–156]. ZW breaks the Li^+-EO_{10} coordination and reduces the wrapping of EO_{10} chains around Li^+, which in turn increases R_g of EO_{10} chains. It is also noted that R_g of EO_{10} chains is about 10% smaller in case-A than in case-B systems, which is consistent with literature[155,157]. Experimental work of Loo et al. [155] showed that R_g decreases by 20% as Li^+:O(PEO) molar ratio increases from 1:20 to 1:7 in LiTFSI/PEO electrolytes at 90 °C (PEO molecular weight: 35000 g/mol). PEO forms local coordination cages for Li^+ and becomes more compact as the Li^+:O(PEO) molar ratio increases until reaching the critical value, at which all O from PEO are in coordination with Li^+ ions. The critical Li^+:O(PEO) molar ratio equals the maximum Li^+-O coordination number of around six[157]. In PEO-based electrolytes, Li^+ transport depends directly on PEO conformational

dynamics[107,158]. ZW molecules might affect the mobility of Li^+ through changing the conformation of PEO chains.

4.3.7 Sigma profiles

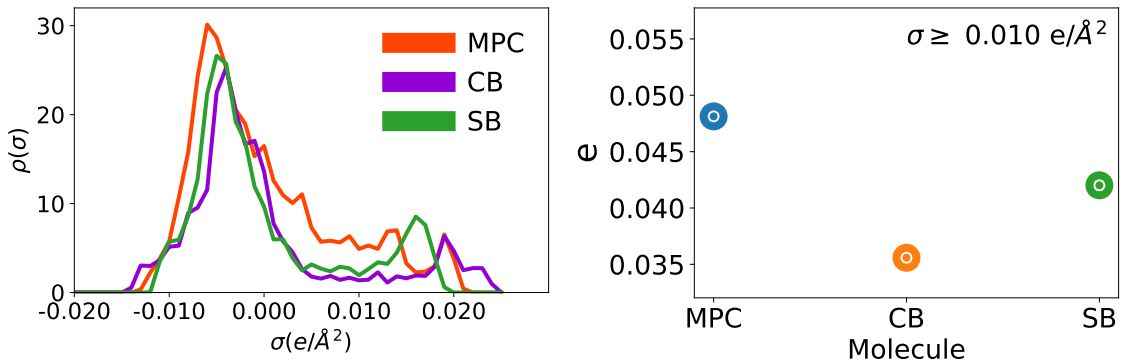

(a) (b)

Figure 4.12. (a) Sigma profiles and (b) integral of H-bond acceptor region for three ZW structures

Sigma (σ) profiles have been used as a descriptor for predictive solvation thermodynamic models such as COSMO-RS (Real Solvent) and COSMO-SAC (Segment Activity Coefficient) [144,146,159]. A sigma profile is the probability distribution of a molecular surface segment having a specific charge density[146]. The electronegativity of a molecule can be quantified by the area of H-bond acceptor region (σ>=0.01 e/Å^2) in sigma profiles[160–163]. Figure 4.12 shows the sigma profiles and the area of H-bond acceptor of three ZW structures. MPC has two peaks at around 0.013 and 0.020 e/Å^2, which corresponds to the two single-bonded O atoms and the two double-bonded O atoms from $–PO_4$ group. Figure 4.12b shows that the integrated area follows the order: MPC > SB > CB. MPC has the highest electronegativity, which explains the highest RDF peak height of cation-MPC and the highest dissociation effect on Li^+-O([TFSI]-) and Li^+-O(EO10) (Figures 4.3 - 4.5 and Tables 4.1 - 4.2). Meanwhile, CB has a peak at the furthest position on the right side of the sigma profiles, as shown in Figure 4.12a. The more far right the

peak position, the higher charge density the anionic group has. This might be the reason why CB is the second in the dissociation effect on Li^+-O([TFSI]-) and Li^+-O(EO10) among three ZW structures (Figures 4.3 - 4.5 and Tables 4.1 - 4.2).

4.3.8 Effect of simulation temperature

The distinct effect of three ZW structures on ionic solvation remains when increasing the system temperature from 353K to 600K. We include the simulation results at 353K to show that our elevation of temperature to 600K only enhances the dynamics of ions and molecules. The enhancement is necessary for probing the mobility of ions and molecules within reasonable simulation time. Figures C12-13 and Tables C6-7 show that among the three ZW structures, MPC has the strongest effect to decrease the RDF peak heights and coordination numbers of Li^+-O($[TFSI]^-$) and Li^+-O(EO_{10}) for systems at 353K. These phenomena are also observed in systems at 600K. Likewise, the RDF peak heights and coordination number of Li^+-O(ZW) rank in the order: MPC>CB>SB at 353K. The Li^+-Li^+ pairing preference is also present with ZW addition in the order MPC>CB>SB at 353K, as shown in Figure C14. Similarly, Table C8 shows that MPC fully releases Li^+ from coordinating with EO_{10} the most among the three ZW structures at 353K. Figures C16-18 show that ions and molecules have slower dynamics in systems at 353K than at 600K. For example, the C(t) curves of Li^+-O($[TFSI]^-$) and Li^+-O(EO10) coordination decay to more than 40% after 400-ns in case-A system at 353K (Figure C16), while to 0% after less than 300-ns at 600K (Figure C1). In addition, Figure C18 the diffusion coefficients of Li^+, $[TFSI]^-$ and ZW at 353K are 10^{-5} -10^{-4} nm^2/ns, which are two orders of magnitude less than at 600K in case-A systems (Figure 4.9). Likewise, in case-B systems, diffusion coefficients of ions and molecules increase by around 20 times. The ionic diffusion in case-B is less impacted by the temperature elevation than in case-A. The phenomenon is also observed in the computational work of Brooks et al. [164] When temperature changes from 360K to

480K, Li^+ diffusion coefficient increased by 55 times with Li^+:O(EO)=1:13 while 36 times with Li^+:O(EO)=1:17[164]. It appears that as the temperature becomes higher, the diffusion of ions in high and low concentrations will start to become similar. Therefore, the magnitude of the diffusion increase is lesser for a lower concentration than for a higher concentration.

4.4 Conclusion

This work investigates the effect of three ZW molecules (MPC, CB, and SB) on Li^+ coordination in LiTFSI/EO_{10} systems using MD simulations. We analyze the structural and dynamic properties of ionic solvation and diffusion of ions and molecules in the eight electrolytes composed of LiTFSI/EO_{10} without ZW and with ZW addition (ZW: Li^+ = 1:5) at two Li^+: O(EO_{10}) molar ratios r = 1:6 (case-A) and 1:18 (case-B). The simulation results show that the common and distinct effect of the three ZW molecules on Li^+ solvation in LiTFSI/EO_{10} systems. All MPC, SB, and CB can detach Li^+ from EO_{10} chains by forming strong Li^+-ZW coordination. The order is MPC>CB>SB. The distinct effect of the three ZW molecules relates to their anionic group. MPC has the highest electronegativity among the three ZW structures, leading to forming the most stable Li^+-ZW coordination and the highest dissociation effect on Li^+-EO_{10}. Further, MPC can exclusively coordinate with around 10% Li^+. CB has the highest charge density, making it the second in dissociation effect on Li^+-EO_{10}. CB molecules can also exclusively coordinate with 2-4% Li^+. SB molecules do not present any coordination exclusion effect in our simulations. In the 1:18 molar ratio, all three ZW molecules reduce the diffusion of Li^+. The Li^+ diffusion slows down the most with MPC and the least with CB addition. However, only SB molecules reduce the diffusion coefficient of Li^+ by 25% when shifting to the 1:6 molar ratio systems. The ZW effect on Li^+ diffusion suggests that MPC is beneficial in a high concentration such as case-A, where Li^+ are released from EO_{10} and $[TFSI]^-$ the most with minute

diffusion slowing. CB is effective in dissociation of Li^+-EO_{10} coordination while inducing the least Li^+ diffusion reduction in a low concentration as case-B. Our simulations imply designing different ZW molecular structures as additives is a promising route to control Li^+ ionic solvation in polymer systems. However, we must be very careful about the potential effect of ZW additives on the ionic conductivity. ZW molecules may perform their functions better in a polymer system with a high ionic concentration.

CHAPTER 5. DESCRIPTION OF REACTION AND VIBRATIONAL ENERGETICS OF CO_2-NH_3 INTERACTION USING QUANTUM COMPUTING ALGORITHMS

5.1 Introduction

Quantum computing will play an important role in future innovations in computational chemistry. Quantum computers offer exponential speed-up to solve certain problems that are intractable for classical computers. For example, quantum computers in principle can reduce the simulation complexity for quantum many-body systems from exponential down to just polynomial[40,41,165].

The variational quantum eigensolver (VQE) is one of the most promising quantum computing tools for applications in computational chemistry of near-term quantum computers[42,166–168]. VQE is a hybrid quantum-classical algorithm which allows the eigenvalues of the Hamiltonian of fermionic or bosonic systems to be quantified. [42] It relies on a quantum simulator or computer to estimate an energy expectation value, while relying on a classical optimizer to suggest improvements of the ansatz. [42,43]

For calculating the electronic energies of molecules, the combination of VQE algorithm with chemistry-inspired ansatz has been applied to evaluate the electronic ground and excited states of simple molecules with up to a few atoms. [44,169–171] A typical VQE setup for the electronic energies of a reaction system with CO_2 and NH_3 molecules requires 46 qubits even for the minimal Slater-type Orbital-3G (STO-3G) basis set (the number of qubits used is equal to the number of spin-orbitals of the specified basis set), making the algorithm computationally challenging on available quantum simulators or devices. A quantum embedding scheme known as Hartree-Fock (HF) embedding has been proposed to circumvent the difficulty in simulating such large system. In this framework, the electronic structures of the full system are broken into fragments consisting of the active space (AS) which defines a subset of active frontier orbitals and the environment. Each part is described quantum mechanically with the environment treated with the HF method

while employing a high-level quantum mechanical description for the AS. The time-independent Schrödinger equation of the AS is connected to the exchange-correlation embedding potential of the environment such that a new Hamiltonian is defined for the full system. Reduction of qubit resources is achieved since the VQE computation is restricted to the AS while the environment is treated with the HF classical solver. The algorithm was previously validated for the symmetric dissociation of H_2O, which involves non-equilibrium geometry structures, yielding an energy profile in close agreement with the reference full configuration interaction (FCI) calculations when a sufficiently large AS was used. [172] The dissociation of N_2 and O_2 were also chosen as additional systems to benchmark the algorithm since both molecules show strong correlation character when the bond is stretched. The HF embedding simulated potential energy curves were found to reach near FCI accuracy.

For assessing vibrational energies of the molecules, quantum computing algorithms can also be utilized to enhance the calculations of vibrational properties[45,47,173]. Molecular vibrational properties are important in understanding the mechanisms and kinetics of chemical reactions. The anharmonicity or couplings of molecular vibrational modes are critical for polyatomic molecules. For example, full infrared (IR) and Raman spectra can be computed by including anharmonic corrections[174,175]. The thermodynamic quantities such as entropy and heat capacity are greatly affected by anharmonicity[176]. The larger the molecule, the stronger the effect of anharmonicity on vibrational properties[177,178]. However, the significant anharmonicity makes determining the vibrational structure classically intractable for large molecules[39]. Based on the second quantization representation of the molecular Hamiltonian[179], the VQE calculation of vibrational structures has qubit encoding of vibrational levels and enables the expansion of the potential energy surface to contain n-body coupling terms[45,180]. The VQE algorithm has been demonstrated to solve the vibrational Hamiltonian with the effect of anharmonic vibrations for triatomic molecules such as CO_2, H_2O, SO_2, and NO_2[45–47]. In addition, the

vibrational excitation energies can also be calculated with the quantum Equation Of Motion (qEOM) [180] approach.

For simulating reaction systems, both the electronic and vibrational energies of the molecules need to be assessed to obtain the chemical reaction energies. Here, we benchmark the performance of quantum computing in the study of chemical reactions for CO_2 capture application. CO_2 capture research is one of the low hanging fruits for the application of quantum computing, and is considered to be one of the near-term opportunities[165]. Given the urgent need to address global warming, CO_2 capture is considered a key pathway to reduce emissions from burning fossil fuels. [4] Amine-based solvents are often used to capture CO_2 by simple chemical reactions. [181] To simplify the calculation, we use NH_3 as a model solvent for the CO_2 capture reaction. The reaction is as follows: $NH_3 + CO_2 = NH_2COOH$. This work aims to utilize the VQE algorithm to calculate ground-state vibrational energies and construct the reaction energy profile of the reaction between CO_2 and NH_3 in the gas phase. We also compute vibrational excited energies with qEOM approach for CO_2 and NH_3. We evaluate the performance of HF embedding in the calculation of potential energies along the reaction pathway. In addition to computing vibrational energies, we also compare the performance of two ansatzes with different circuit depths on a quantum simulator: Unitary Vibrational Coupled Cluster (UVCC) and Compact Heuristic for Chemistry (CHC) ansatzes. Current noisy intermediate-scale quantum (NISQ) computers require quantum algorithms with shallow circuit depths to mitigate hardware noise. Hence, we compared the performance of both ansatzes in quantum noise simulations. We also investigated the effectiveness of the "Zero Noise Extrapolation" (ZNE) error-mitigation method[28]. CHC has a shallower circuit depth than UVCC and thus higher accuracy in the presence of simulated quantum errors with and without error mitigation.

5.2 Calculation Methods

5.2.1 Reaction profile construction

The HF embedding calculations for electronic energies were performed using the Qiskit Nature platform[182], a Python package that interfaces a quantum computing framework with existing classical quantum chemistry software PySCF[183,184] to generate classical data such as electronic integrals in the atomic orbital basis. [182] For the AS portion, we used a Unitary Coupled Cluster Ansatz with single and double excitations (UCCSD) to represent the electronic wavefunction, and the Jordan-Wigner scheme for fermion to qubit mapping. [185] VQE simulations were carried out on the Qiskit statevector simulator and the minimal STO-3G basis set was employed to further reduce the quantum requirement. [185] The gradient-based Broyden-Fletcher-Goldfarb-Shanno (BFGS) minimization method was used for the optimization of the VQE parameters.[186,187] The reaction coordinate was computed using plane-wave DFT with the Perdew-Burke-Enzerhoff (PBE) functional and the all-electron, frozen core, projected augmented wave (PAW) method in VASP. [188] The self-consistently simulated valence electrons were H 1*s* electron, and C, N, O 2*s* and 2*p* electrons. The minimum-energy pathway across a DFT potential energy surface was obtained from a Climbing Image Nudged Elastic Band (CI-NEB) calculation using 7 movable images[189]. HF embedding energies are compared with those obtained from HF and CCSD calculations. Our approach for ascertaining the performance of quantum algorithm for simple concerted reactions and more complex ones that involve bond rupture and formation follows previous works[190,191].

5.2.2 Ground state vibrational energy calculation

Figure 5.1 shows the steps to compute ground state energy using variational quantum eigensolver (VQE) algorithm[192].

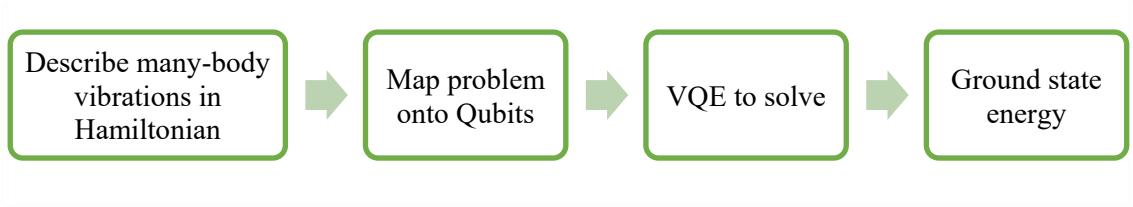

Figure 5.1. Ground state energy calculation flowchart using variational quantum eigensolver algorithm.

The ground state vibrational energy is obtained by solving the nuclear Schrödinger equation under the Born-Oppenheimer approximation:

$$\mathcal{H}_{\text{vib}}|\Psi_n\rangle = E_n|\Psi_n\rangle \tag{5.1}$$

The anharmonicity effect can be included in our calculation by adding higher-order potential energy terms in the so-called Watson Hamiltonian (neglecting vibro-rotational couplings):

$$\mathcal{H}_{\text{vib}}(Q_1,\ldots,Q_L) = -\frac{1}{2}\sum_{l=1}^{L}\frac{\partial^2}{\partial Q_l^2} + V(Q_1,\ldots,Q_L) \tag{5.2}$$

We describe the many-body vibrational potential using Vibrational Self-Consistent Field (VSCF) method[45,193]:

$$V\left(Q_1,\ \ldots,\ Q_L\right) = \frac{1}{2}\sum_{ij}k_{ij}Q_iQ_j + \frac{1}{6}\sum_{ijk}k_{ijk}Q_iQ_jQ_k + \frac{1}{24}\sum_{ijkl}k_{ijkl}Q_iQ_j\,Q_kQ_l \tag{5.3}$$

where V is potential energy, and Q_i is vibrational internal coordinate. In this study, we describe many-body potential energy with expansion to the 4th order as shown in the equation. Four-body expansion can obtain an accuracy of about 1–2 cm^{-1}. The terms k_{ij}, k_{ijk}, and k_{ijkl} are anharmonic force field constants. These constants are calculated by semi-numerical differentiation of the analytical Hessian as implemented in Gaussian software[145].

Molecular geometries are first optimized based on quantum mechanics at the B3LYP/cc-pVTZ level of theory using Gaussian software[145].

In second quantization, nuclear Hamiltonian is described as:

$$\mathscr{H}_{\text{vib}}^{\text{SQ}} = \sum_{l=1}^{L} \sum_{k_l,h_l}^{N_l} \langle \phi_{k_l} | T(Q_l) + V^{[l]}(Q_l) | \phi_{h_l} \rangle a_{k_l}^{+} a_{h_l} + \sum_{l<m}^{L} \sum_{k_l,h_l}^{N_l} \sum_{k_m,h_m}^{N_m} \langle \phi_{k_l}\phi_{k_m} | V^{[l,m]}(Q_l, Q_m) | \phi_{h_l}\phi_{h_m} \rangle a_{k_l}^{+} a_{k_m}^{+} a_{h_l} a_{h_m} + \ldots \tag{5.4}$$

Where $V^{[l]}(Q_l)$ and $V^{[l,m]}(Q_l, Q_m)$ represent the variation of the potential energy upon displacements along one *l*-th normal coordinate (Q_l) and both *l*-th and *m*-th coordinates (Q_l, Q_m) from the equilibrium position correspondingly[45,194].

$$V^{[l]}(Q_l) = V(Q_1^{\text{eq}}, \ldots, Q_{l-1}^{\text{eq}}, Q_l, \ldots, Q_L^{\text{eq}}) \tag{5.5}$$

$$V^{[l,m]}(Q_l, Q_m) = V(Q_1^{eq}, \ldots, Q_l, Q_m, \ldots, Q_L^{eq}) - V^{[l]}(Q_l) - V^{[m]}(Q_m) \tag{5.6}$$

The many-body basis functions are encoded within the n-mode second quantization as occupation-number vectors (ONVs) as follows[45,179]:

$$\phi_{k_1}(Q_1) \cdots \phi_{k_L}(Q_L) \equiv |0_1 \cdots 1_{k_1} \cdots 0_{N_1}, 0_1 \cdots 1_{k_2} \cdots 0_{N_2}, \cdots, 0_1 \cdots 1_{k_L} \cdots 0_{N_L}\rangle \tag{5.7}$$

The nuclear wavefunction can be expressed as[179]:

$$|\Psi\rangle = \sum_{k_1=1}^{N_1} \cdots \sum_{k_L=1}^{N_L} C_{k_1,\ldots,k_L} \phi_{k_1}^{(1)}(Q_1) \cdots \phi_{k_L}^{(L)}(Q_L) \tag{5.8}$$

where each mode *l* is described by a basis of N_l modals (basis functions).

Creation and annihilation operators per mode l and per basis function k_l are defined as:

$$\begin{aligned} a_{k_l}^{\dagger} |\ldots, 0_1 \ldots 0_{k_l} \ldots 0_{N_l}, \ldots\rangle &= |\ldots, 0_1 \ldots 1_{k_l} \ldots 0_{N_l}, \ldots\rangle \\ a_{k_l}^{\dagger} |\ldots, 0_1 \ldots 1_{k_l} \ldots 0_{N_l}, \ldots\rangle &= 0 \\ a_{k_l} |\ldots, 0_1 \ldots 1_{k_l} \ldots 0_{N_l}, \ldots\rangle &= |\ldots, 0_1 \ldots 0_{k_l} \ldots 0_{N_l}, \ldots\rangle \\ a_{k_l} |\ldots, 0_1 \ldots 0_{k_l} \ldots 0_{N_l}, \ldots\rangle &= 0 \end{aligned} \tag{5.9}$$

The Hamiltonian is encoded onto qubits using the "direct mapping" method[47,173]. The number of modals N_l for a given vibrational mode *l* are represented by a N_l-qubit

register. We note that a more compact mapping such as binary mapping can reduce the number of qubits to encode the vibrational Hamiltonian[45,47,195]. Vibrational wavefunction can be represented with $L \times N$ (direct mapping) or $L \times log(N)$ (compact mapping) qubits for molecules with L vibrational modes[195]. However, such compact mapping has a higher circuit depth and number of terms in the Hamiltonian than direct mapping due to the more complex representation of the elementary raising and lowering operators[45,47]. For example, the Hamiltonian contains $O(L^k N^k)$ (direct mapping) or $O(L^k N^{2k})$ (compact mapping) terms (k: potential energy expansion order) [47]. The increased circuit depth will result in larger hardware errors in NISQ devices. Thus, we use direct mapping method for quantum computing of vibrational energies. The qubit numbers for CO_2, NH_3, and NH_2COOH molecules are listed in Table 5.1. Figure 5.2 shows the molecular structures of CO_2, NH_3, and NH_2COOH.

Table 5.1. Quantum circuit resource estimation for the calculation of the ground-state vibrational energy of CO_2, NH_3, and NH_2COOH with the UVCC and CHC approaches with single excitation. The number of CNOT gates (CX) is given for both approaches.

Molecule	Modes	Modals	Qubit Number	CX UVCC	CX CHC
CO_2	4	2	8	16	8
NH_3	6	2	12	24	12
NH_2COOH	15	2	30	60	30

We use the VQE algorithm to find the ground state of vibrational Hamiltonians. The accuracy of VQE algorithms is susceptible to quantum errors in noisy intermediate-scale quantum (NISQ) devices. Algorithms with shallow circuit depths can alleviate the effect of hardware noise by allowing quantum operations within the limited coherence time of the NISQ devices. Hardware-efficient ansatzes are thus developed to reduce the circuit depth needed to prepare the initial vibrational wavefunction[45,169]. In this study, we use two

ansatzes with different circuit depths: Unitary Vibrational Coupled Cluster (UVCC[47]) and Compact Heuristic for Chemistry (CHC[45]) ansatzes. The number of CNOT gates in the CHC ansatz circuit is one order of magnitude less than that of UVCC with double excitations[45]. Thus, CHC with shallower circuit depth can help lessen the sensitivity to noise for better performance of VQE calculation in noisy simulations. To access the benefit of CHC, we compare the accuracy of VQE calculations against the classical diagonalization result with and without gate errors. Additionally, we apply the "Zero Noise Extrapolation" (ZNE) error mitigation technique[196] to reduce the simulated noise effect. With the ZNE approach, the expectation values are computed with amplified noises by different factors (1, 3, and 5), and then the noiseless results are extrapolated using linear extrapolation based on the measured expectation values. CHC and UVCC are implemented with single excitation. The ansatzes' CNOT gate numbers are shown in Table 5.1. The constrained optimization by linear approximation (COBYLA) optimizer is utilized. All VQE calculations are performed by Qiskit[182].

The vibrational excitation energies are calculated with the quantum Equation Of Motion (qEOM) [180] approach by solving the pseudo-eigenvalue problem (Equation 10). We use the qEOM operators with single and double excitations.

$$\begin{pmatrix} M & Q \\ Q^* & M^* \end{pmatrix}\begin{pmatrix} X_n \\ Y_n \end{pmatrix} = E_{0n}\begin{pmatrix} V & W \\ -W^* & -V^* \end{pmatrix}\begin{pmatrix} X_n \\ Y_n \end{pmatrix} \tag{5.10}$$

where:

$$M_{\mu_\alpha \nu_\beta} = \langle 0|[(\hat{\mathrm{E}}^{(\alpha)}_{\mu_\alpha})^\dagger, \hat{\mathrm{H}}, \hat{\mathrm{E}}^{(\beta)}_{\nu_\beta}]|0\rangle$$

$$Q_{\mu_\alpha \nu_\beta} = -\langle 0|[(\hat{\mathrm{E}}^{(\alpha)}_{\mu_\alpha})^\dagger, \hat{\mathrm{H}}, (\hat{\mathrm{E}}^{(\beta)}_{\nu_\beta})^\dagger]|0\rangle$$

$$V_{\mu_\alpha \nu_\beta} = \langle 0|[(\hat{\mathrm{E}}^{(\alpha)}_{\mu_\alpha})^\dagger, \hat{\mathrm{E}}^{(\beta)}_{\nu_\beta}]|0\rangle$$

$$W_{\mu_\alpha \nu_\beta} = -\langle 0|[(\hat{\mathrm{E}}^{(\alpha)}_{\mu_\alpha})^\dagger, (\hat{\mathrm{E}}^{(\beta)}_{\nu_\beta})^\dagger]|0\rangle$$

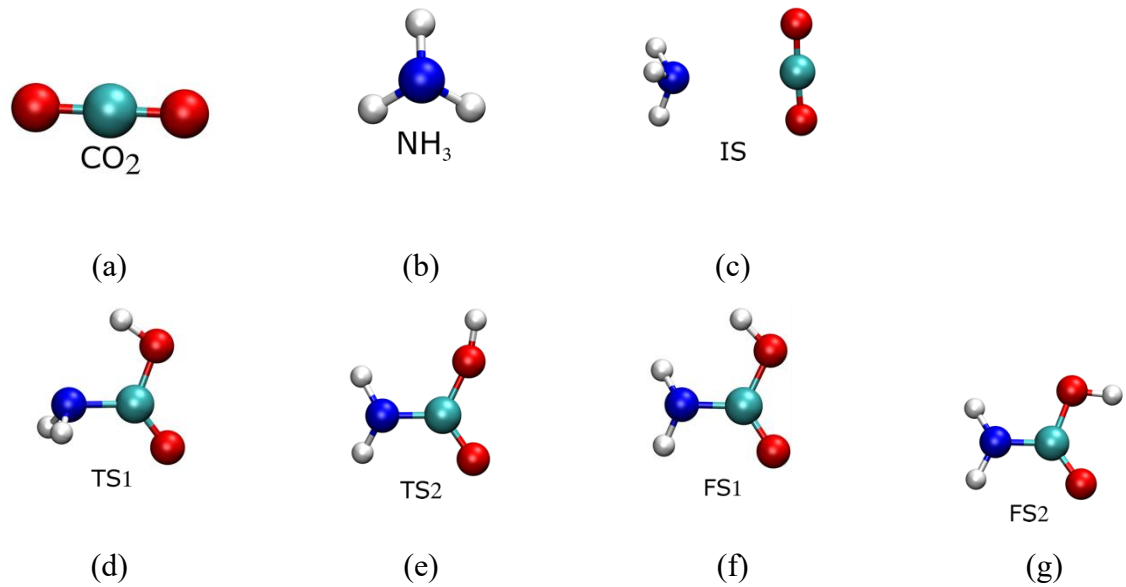

Figure 5.2. Molecular representations of (a) CO_2, (b) NH_3, (c) NH_2COOH initial state (IS: NH_3+CO_2), (d) NH_2COOH transitional state 1 (TS1), (e) NH_2COOH transitional state 2 (TS2), (f) NH_2COOH final state 1 (FS1), and (g) NH_2COOH final state 2 (FS2). Atom color code: hydrogen (silver), carbon (cyan), nitrogen (blue), and oxygen (red).

5.3 Results and Discussions

5.3.1 Reaction profile based on the electronic energy calculations

Figure 5.3 depicts the HF embedding predicted reaction profile using six spatial orbitals in the AS. We plotted the relative energy $E - E_i$ along the reaction pathway, where the latter term is the initial state energy. The preliminary step occurs through a hydrogen transfer from NH_3 to CO_2 resulting in an O-H bond. Moreover, an N-C bond is formed as the molecules approach each other to produce a NH_2-COOH pair. HF embedding found the energy of reaction to be uphill with an activation barrier of 0.031 Hartree (Ha). A bent CO_2 molecule with significant interaction with both the transferring H atom and the remaining NH_2 is observed for the transition state. Once the intermediate forms, the NH_2-COOH pair reorients towards a more stable structure as the transferred H then flips away from the NH_2 fragment. While this path is energetically downhill, it is found to be more highly activated with a barrier of 0.071 Ha.

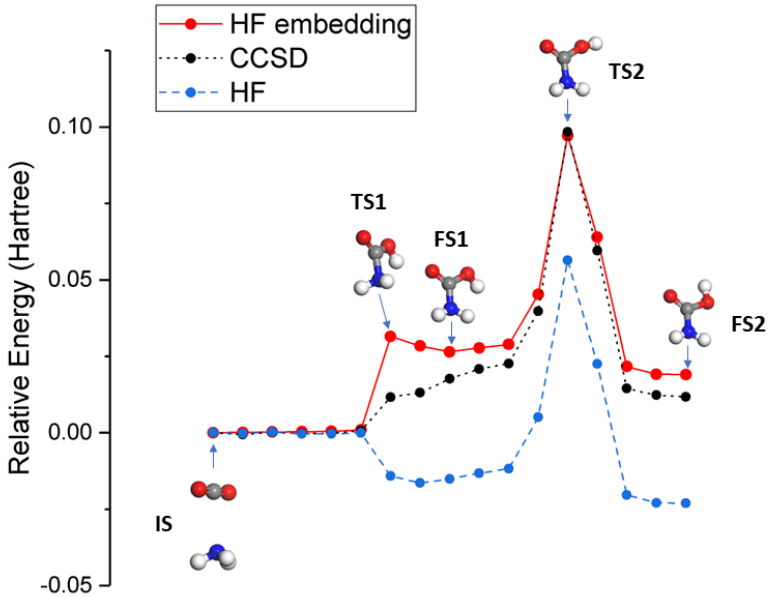

Figure 5.3. Potential energy curve for addition reaction between CO_2 and NH_3 calculated by HF embedding, CCSD and HF.Atom colors: H: white, N: blue, C: gray, O: red.

The results obtained with HF embedding were compared with standard HF and post-HF Coupled Cluster Singles and Doubles (CCSD) (Figure 5.3). Comparison of HF embedding and post-HF CCSD calculations does not yield large discrepancies with the former within a few 10^{-2} Ha from the reference CCSD curve. Both methods predicts that the initial NH_2-COOH pair formation and its subsequent rearrangement are thermodynamically uphill and downhill, respectively. Additionally, the embedding scheme agrees with CCSD that the flipping process is the kinetically limiting step. Though CCSD yields an initial step that is transition-state-free, the positive reaction energy indicates that this process has an activation barrier. With reference to the CCSD results, the embedding scheme performs better than the conventional HF despite the drastic reduction of the number of qubits. In particular, the discrepancy is pronounced in the energy profile of the initial addition step. HF predicts this process to be transition-state-free but with a negative reaction energy, and thus a barrierless downhill process. By contrast, both CCSD and HF embedding predict this route as an activated process.

5.3.2 Assessment of molecular ground state vibrational energies in noiseless simulations

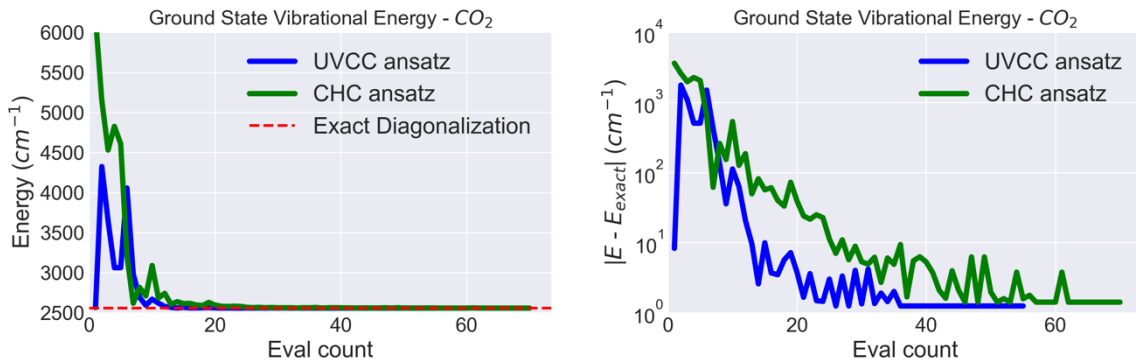

(a) (b)

Figure 5.4. (a) Ground state vibrational energy and (b) accuracy convergence with number of iterations (eval count) for CO_2 molecule. E_{exact} values are obtained by diagonalization of the vibrational Hamiltonian.

Figure 5.4 shows the evaluation result of ground state vibrational energies for CO_2 in the energy unit of cm^{-1} (1 eV = 0.0367502 Hartree = 8065.73 cm^{-1}) calculated by the VQE simulations. The performances of the UVCC and CHC ansatzes are similar for the ground state vibrational energy calculation of CO_2. Convergence is reached after ~40 iterations for UVCC and ~65 iterations for CHC, as shown in Figure 5.4. The calculated energies are compared with the exact solutions (E_{exact}) obtained by diagonalizing the vibrational Hamiltonian. Figure 5.4b shows that both ansatzes converge to the accuracy of 1 cm^{-1}.

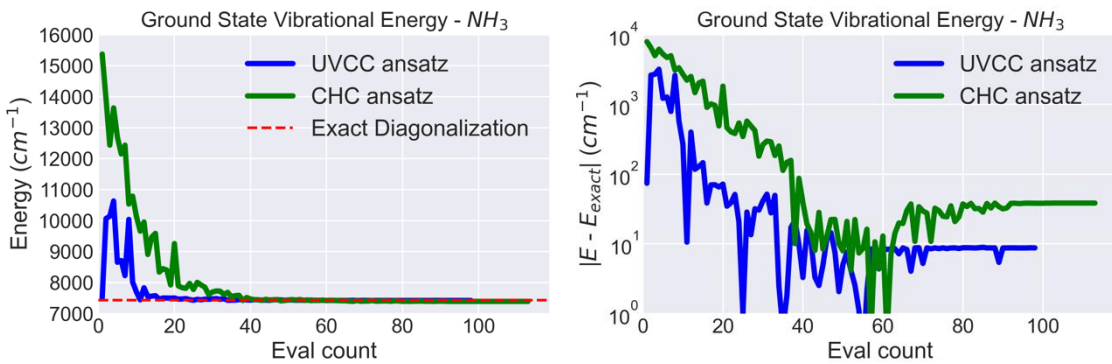

(a) (b)

Figure 5.5. (a) Ground state energy and (b) accuracy convergence with number of iterations (eval count) for NH_3 molecule. Reference values (E_{exact}) are obtained by diagonalization of the vibrational Hamiltonian.

As the molecule gets larger with an increasing number of atoms, VQE calculations with UVCC have higher accuracy than CHC. Figure 5.5 shows the result of ground state vibrational energies for NH_3. UVCC converged to a higher accuracy of 9 cm^{-1} compared to that of CHC with 38 cm^{-1} after about 100 iterations. It is noted that the accuracy of the VQE calculations becomes less for NH_3 compared to CO_2. The difference between converged energy and exact diagonalization result is 1 cm^{-1} for CO_2 (Figure 5.3b) but increases to 9 cm^{-1} for NH_3 (Figure 5.5b) with the same UVCC ansatz. This decrease in accuracy might indicate that the VQE algorithm becomes less accurate for larger molecules such as NH_3 compared to CO_2.

For the NH_2COOH molecule, the VQE simulation with the UVCC ansatz converges to a lower energy than that with the CHC ansatz, as shown in Figure 5.6. However, the classical diagonalization result for NH_2COOH is not obtainable due to the large memory requirement on a classical computer[45]. The size of the vibrational Hamiltonian matrix is $k^{3N-6} \times k^{3N-6}$ for a nonlinear molecule of N atoms with 3N – 6 degrees of freedom and a basis set of size k for each degree of freedom. Due to the exponential increase in matrix size with N atoms, classical diagonalization is only viable up to N=5[197–

[199]. The unfeasibility of the classical solution suggests the advantage of quantum computing over classical computing for the vibrational simulation of large molecules with atoms larger than five.

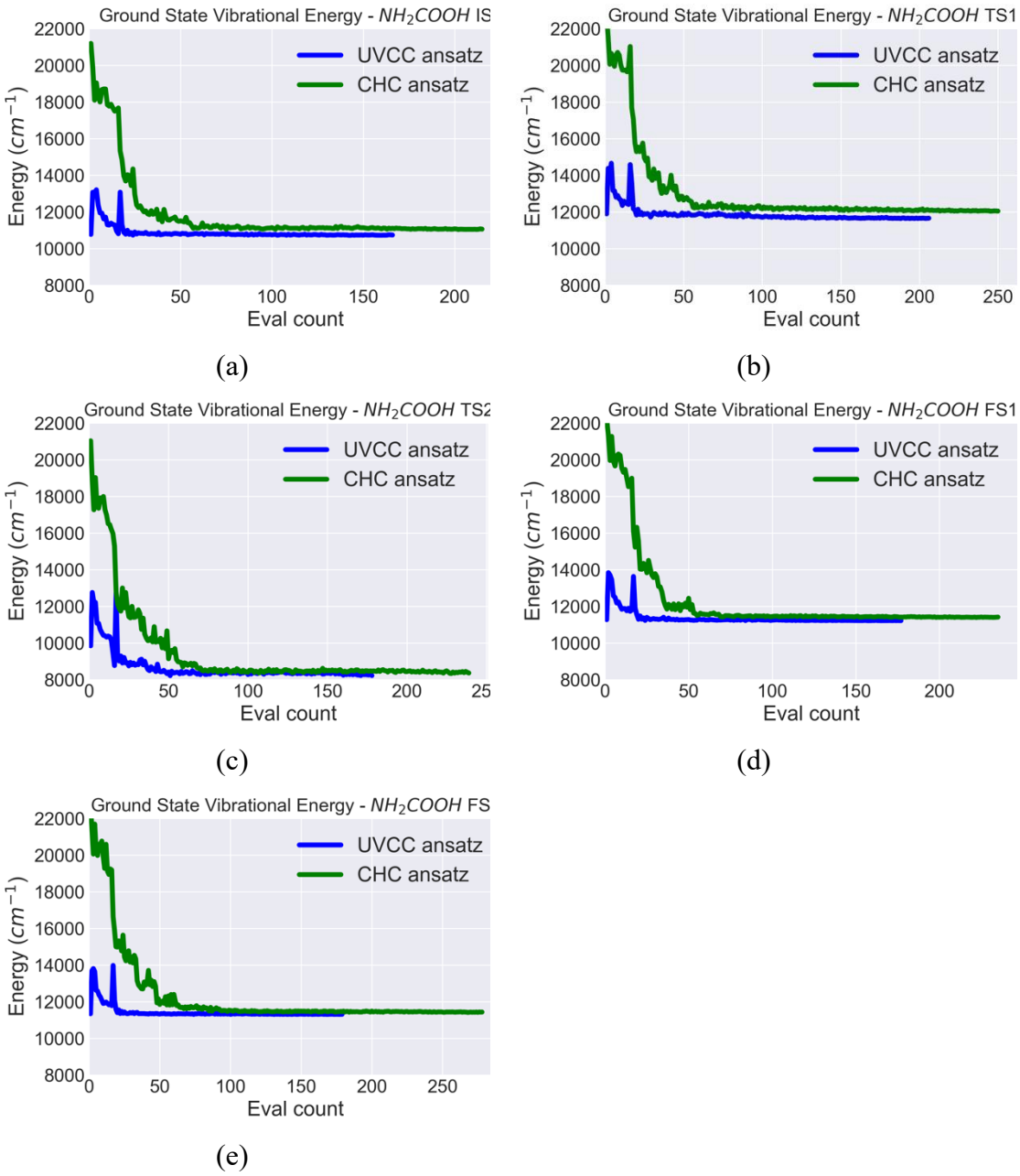

Figure 5.6. Ground state energy convergence with number of iterations (eval count) for NH_2COOH molecule in its (a) initial state (IS), (b) transition state 1 (TS1), (c) transitional state 2 (TS2), (d) final state 1 (FS1), and (e) final state 2 (FS2).

5.3.3 Quantum computation of vibrational structures in noise simulations

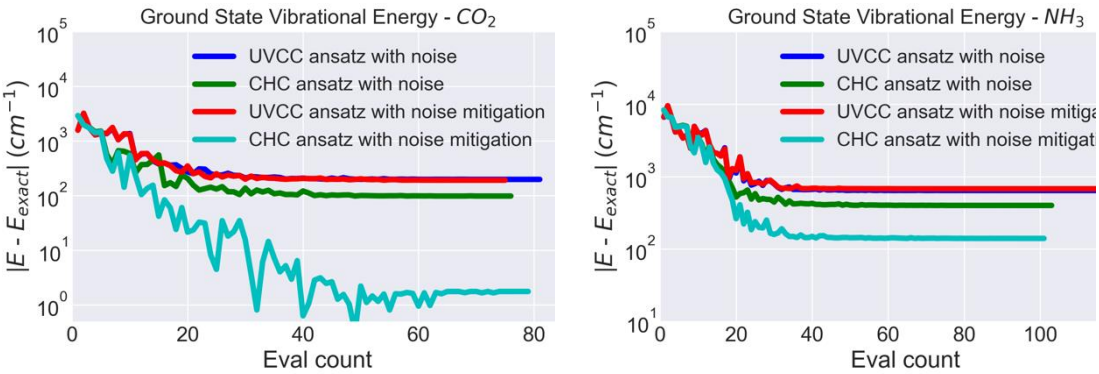

(a) (b)

Figure 5.7. Ground state energy convergence with number of iterations (eval count) for (a) CO_2 and (b) NH_3 molecules in the presence of simulated hardware noise and ZNE error-mitigation technique.

The CHC ansatz with a shallower circuit depth has higher accuracy than the UVCC ansatz in the quantum simulator with the presence of hardware noise. We use a noise model to simulate the realistic condition of the quantum computer. The noise model includes depolarization error rates which are based on the average gate depolarization errors in the ibmq_almaden 20-qubit device ($7x10^{-4}$, $1.4x10^{-3}$ and $2.2x10^{-2}$ for U2, U3 and CNOT gates, respectively) [45]. Figure 5.7 shows the ground state vibrational energy results in the presence of simulated hardware noise for CO_2 and NH_3 molecules. The CHC circuit converges to better accuracy than the UVCC circuit for the CO_2 molecule, with accuracies of 99 and 199 cm^{-1}, respectively, as shown in Figure 5.7a. The same phenomenon is also present in the NH_3 case. Figure 5.7b shows that the accuracy for CHC is 401 $cm^{-1,}$ which is higher than that of UVCC (644 cm^{-1}) for the NH_3 molecule. As CHC circuit has a smaller number of CNOT gates than UVCC (Table 5.1), VQE calculations with CHC have lesser gate error and thus result in better accuracy. The higher accuracy of CHC compared to UVCC suggests the benefit of shallower depth circuits for near-term quantum computers where

hardware noise is inevitable. It is noted that the noise model is not successful for larger molecules such as NH_2COOH, which require a higher number of qubits in the simulations.

The VQE accuracy with CHC ansatz can increase by applying ZNE error-mitigation technique. Figure 5.7 shows that this ZNE approach improves the accuracy from 99 to 2 cm^{-1} for CO_2 molecule, and from 401 to 141 cm^{-1} for NH_3 molecule in vibrational ground state energy calculation by VQE algorithm with CHC ansatz. The ZNE method has little effect on the accuracy of VQE calculation with UVCC ansatz (from 199 to 192 cm^{-1} for CO_2 and from 644 to 680 cm^{-1} for NH_3). Our results suggest the combination of shallow circuit depth and an effective error mitigation approach can help reduce the noise effect in real NISQ devices.

5.3.4 Quantum computation of the vibrational excited states

We use qEOM[180] approach to calculate the vibrational excitation energies for CO_2 and NH_3 in noiseless simulations. The reference values are obtained by the classical diagonalization of the system Hamiltonian. The calculated results of vibrational energies are presented in Table 5.2. At low-level excited states (1st and 2nd), the energies are computed with accuracy ~4-6 cm^{-1} for CO_2 with both CHC and UVCC ansatzes. For NH_3, the accuracy is lower for CHC compared to UVCC. For example, at the 1st and 2nd excited states, the accuracy for CHC is 87 and 117 cm^{-1}, whereas the accuracy for UVCC is 57 and 38 cm^{-1} respectively. The better performance of UVCC on vibrational excited state assessment is also present in ground state calculation in noise-less simulation.

Table 5.2. Results of vibrational energy calculations for CO2, NH3, and NH2COOH molecules.

Molecule	Qubit Number	Vibrational Energy (cm^{-1})			
		Quantum computing			Classical computing
		Noiseless model	Hardware noise model	Error mitigation	
CO_2 Ground state	8	2556 (CHC) 2556 (UVCC)	2654 (CHC) 2754 (UVCC)	2553 (CHC) 2747 (UVCC)	2552 (DFT) 2555 (Exact)
CO_2 Excited states	8	3220/3220 (CHC/UVCC) 3905/3905 (CHC/UVCC) 3931/3931 (CHC/UVCC)	N/A	N/A	3224 (Exact) 3910 (Exact) 3947 (Exact)
NH_3 Ground state	12	7394 (CHC) 7423 (UVCC)	7806 (CHC) 8103 (UVCC)	7573 (CHC) 8112 (UVCC)	7390 (DFT) 7432 (Exact)
NH_3 Excited states	12	8357/8387 (CHC/UVCC) 8982/9011 (CHC/UVCC) 8983/9012 (CHC/UVCC) 9963/9991 (CHC/UVCC)	N/A	N/A	8444 (Exact) 9049 (Exact) 9051 (Exact) 10056 (Exact)
NH_2COOH IS	30	11057 (CHC) 10738 (UVCC)	N/A	N/A	10416 (DFT)

Table 5.3 (continued). Results of vibrational energy calculations for CO2, NH3, and NH2COOH molecules.

Molecule	Qubit Number	Vibrational Energy (cm^{-1})			
		Quantum computing			Classical computing
		Noiseless model	Hardware noise model	Error mitigation	
NH_2COOH TS1	30	12043 (CHC) 11656 (UVCC)	N/A	N/A	10906 (DFT)
NH_2COOH TS2	30	8360 (CHC) 8219 (UVCC)	N/A	N/A	10225 (DFT)
NH_2COOH FS1	30	11412 (CHC) 11218 (UVCC)	N/A	N/A	11023 (DFT)
NH_2COOH FS2	30	11433 (CHC) 11311 (UVCC)	N/A	N/A	11091 (DFT)

5.4 Conclusion

We used the VQE quantum computing algorithm to construct the reaction energy profile and calculate ground-state vibrational energies for the CO_2 reaction with NH_3. In the electronic energy calculations, the HF embedding predicted reaction profile is found to be in good agreement with CCSD and performs better than the conventional HF. In the molecular vibrational calculations, the quantum computing algorithm also helps enhance the calculation of vibrational energies by considering vibrational coupling or anharmonicity effects. We demonstrated that quantum-computed ground state energies had similar accuracy for CO_2 and NH_3 molecules compared to classically computed results using the traditional diagonalization method. The excited states for CO_2 and NH_3 are also evaluated with qEOM method. In noiseless simulations, the VQE algorithm with UVCC ansatz has higher accuracy than with CHC ansatz. However, we found that CHC performed better than UVCC ansatz circuit in the presence of hardware noise due to CHC's shallower

circuit depth. In addition, the ZNE error-mitigation approach is more effective to increase the accuracy for VQE with CHC ansatz. For larger molecules such as NH_2COOH, more qubits, and different ansatzes/circuits are needed to improve the accuracy of vibrational energy calculations. Moreover, the quantum computing calculations were able to solve for the ground state energy of NH_2COOH while the exact diagonalization solution was not obtainable, which suggests the advantage of quantum computing over classical computing for the vibrational energy calculation of large molecules.

CHAPTER 6. CONCLUSIONS AND PERSPECTIVE

6.1 Conclusions

This dissertation aimed to investigate the use of zwitterions (ZW) and quantum computing algorithms for sustainable applications. We focused on studying how ZW can adjust the solvation and transport of ions in Li^+ electrolytes, which are essential for developing safe and efficient solid-state polymer electrolytes. We examined the impact of ZW on ionic interactions and transport under electric fields, as well as their dissociation effects in EO-based electrolytes with different chain lengths, and how ZW chemical structures affect their dissociation ability. Additionally, we explored how quantum computing can be applied to study CO_2 capture reactions. By utilizing quantum computing algorithms, we can uncover insights into the complex mechanisms involved in CO_2 capture, with the goal of optimizing the process efficiency and capacity.

In the first study, we examined the effect of ZW molecules on ionic associations and transport in 1:1 Li salt electrolytes (with anions [TFSI]- and [BETI]-). Through molecular dynamics (MD) simulations under electric fields of 0-1.1 V/nm, we observed a close relationship between ionic association and transport. Small Li^+ ions and large anions exhibited similar diffusion rates with the presence of ZW molecules, suggesting that ZW molecules indirectly facilitated the connection between Li^+ and anions. Furthermore, we found that the electric field needed to surpass a certain threshold to influence the diffusion and associations of ions and ZW molecules.

In. the second study, we investigated the impact of ZW molecules on ionic association in (EO)-based electrolytes using MD simulations. Specifically, we focused on electrolytes composed of oligo(EO) (EO_x, x=2, 3, 4, and 5), LiTFSI and ZW molecules containing cationic imidazole and anionic sulfonate groups. The simulation results revealed two distinct effects of ZW molecules on ionic associations in the electrolytes. First, they could release Li^+ from the wrapping effect of EO_x chains and accelerate Li^+

transport. Second, they can associate with Li^+ themselves and slow down the Li^+ transport. The competition between these two effects relates to the length of the EO_x chains. Overall, our simulations suggest that ZW molecules could help manipulate the ionic conductivity of polyethylene oxide electrolytes.

In the third study, we investigated the solvation structure and dynamics of ions in LiTFSI/(ethylene oxide)$_{10}$ (EO_{10}) with the presence of three distinct ZW molecules (MPC, SB, and CB) using MD simulations. The simulation systems included two Li^+: O(EO_{10}) molar ratios: 1:6 and 1:18. The simulation results demonstrated that all three ZW molecules reduce the Li^+-EO_{10} coordination number and the order is MCP>CB>SB. In addition, nearly 10% of Li^+ exclusively coordinate with MPC molecules, only 2-4% of Li^+ exclusively coordinate with CB molecules, while no Li^+ exclusively coordinates with SB molecules. MPC molecules also present the most stable Li^+ coordination among the three ZW molecules. Our simulations indicated that ZW molecule additives may benefit a high Li^+ concentration environment. At the low Li^+ concentration, all three ZW molecules reduce the diffusion coefficient of Li^+. However, at the high Li^+ concentration, only SB molecules reduce the diffusion coefficient of Li^+.

Finally, in the fourth study, we employed quantum computing algorithms to quantify molecular vibrational energies and reaction pathways between CO_2 and a simplified amine-based solvent model - NH_3. We implemented a variational quantum eigensolver (VQE) algorithm in a quantum simulator to calculate ground state vibrational energies of reactants and products of the CO_2 and NH_3 reaction. The VQE calculations yield ground vibrational energies of CO_2 and NH_3 with similar accuracy to classical computing. In the presence of hardware noise, CHC ansatz with shallower circuit depth performs better than UVCC. The "Zero Noise Extrapolation" error-mitigation approach in combination with CHC ansatz improves the vibrational calculation accuracy. Excited vibrational states were accessed with quantum Equation Of Motion method for CO_2 and NH_3. Using quantum HF embedding algorithm to calculate electronic energies, the

corresponding reaction profile compares favorably with CCSD method while being more accurate than HF.

In summary, this dissertation contributes to the exploration of ZW for enhancing the performance of solid-state polymer electrolytes and the application of quantum computing in optimizing CO_2 capture processes for sustainability purposes.

6.2 Perspective

To continue the study, the following suggestions are proposed:

1. While we investigated three different ZW structures with distinct effect on ionic solvation and transport, the potential ZW structural designs are vast due to their synthesis from ionic liquids. Thus, it is crucial to develop a comprehensive library of ZW structures, encompassing a broader range of designs and their associated properties.
2. ZW polymer electrolytes can exhibit superior conductivity behavior and robust mechanical properties due to their unique structures. Conducting a study on ZW polymers would provide valuable insights into their mechanisms, and potential applications.
3. Sodium and potassium ion batteries have garnered attention as promising alternatives to Li^+ batteries due to the abundance and affordability. Investigating the effect of ZW structures on the solvation and transport of sodium and potassium ions would be beneficial for advancing these battery technologies.
4. In this study, calculations by quantum computing algorithms were done on a simulator. However, it is important to note that the classical simulator utilized in our facility has limitations, allowing for electronic calculations with a maximum of 16 qubits and vibrational calculations with a maximum of 30

qubits. Thus, to explore more complex CO_2 reaction systems, it is imperative to access quantum computing algorithms on real quantum computers, enabling more advanced and accurate simulations.

5. The simulation of CO_2 capture reactions using solvents can be challenging, especially when considering reactions occurring at the air-solvent interfaces and solvation effects. To address these challenges and advance our understanding of CO_2 reactions, one approach is to employ deep learning potential-based molecular dynamics (DPMD). DPMD overcomes the limitations of conventional methods such as molecular dynamics (MD) force fields and ab Initio MD. Unlike MD force fields, DPMD effectively captures bond breaking and forming. Additionally, while ab Initio MD can simulate reactions, its applicability is confined to short simulations and small systems. DPMD, on the other hand, extends beyond these limitations, enabling comprehensive simulations of reactions in larger systems at longer timescales. Hence, the proposed research is developing a DP model to investigate the reaction pathways of CO_2 at the air-solvent interface, with a particular focus on deep eutectic solvents (DESs). DESs have garnered interest due to their low cost, non-toxicity, biodegradability and the ability to capture CO_2 at low partial pressure. The study will provide a detailed mechanistic understanding of CO_2 chemisorption. This understanding will aid in the development of innovative CO_2 capture technologies using DESs.

APPENDICES

APPENDIX 1. SUPPORTING INFORMATION FOR CHAPTER 2

Table A1. Force field parameters for zwitterionic molecules and anions. The labels are shown in Figure 2.1(full charge).

Label	σ (nm)	ε (kJ/mol)	q (e)
Z2C/Z3C			
C1	0.35	0.276144	-0.24
H11, H12 and H13	0.25	0.12552	0.08
C2	0.35	0.276144	-0.17
H21 and H22	0.25	0.12552	0.18
N1	0.325	0.71128	0.22
C3	0.355	0.29288	-0.09
H3	0.242	0.12552	0.21
N2	0.325	0.71128	0.22
C5	0.355	0.29288	-0.24
H5	0.242	0.12552	0.27
C6	0.355	0.29288	-0.24
H6	0.242	0.12552	0.27
C7	0.35	0.276144	-0.17
H71 and H72	0.25	0.12552	0.18
C8	0.350	0.276144	-0.24
H81 and H82	0.250	0.125520	0.1
S	0.355	1.046000	1.32
O1, O2 and O3	0.296	0.711280	-0.76
$[TFSI]^-$			
N	0.325	0.71128	-0.66
S1 and S2	0.355	1.046	1.02
O11, O12, O21 and O22	0.296	0.87864	-0.53
C1 and C2	0.35	0.27614	0.35
F11, F12 and F13	0.295	0.22175	-0.16
F21, F22 and F23	0.295	0.22175	-0.16
[BETI]-			
N	0.325	0.71128	-0.66
S1 and S2	0.355	1.046	1.09
O11, O12, O21 and O22	0.296	0.87864	-0.56
C1	0.35	0.27614	0.12
F11 and F12	0.295	0.22175	-0.13
C3	0.35	0.27614	0.51

Table A1 (continued). Force field parameters for zwitterionic molecules and anions. The labels are shown in Figure 2.1(full charge).

Label	σ (nm)	ε (kJ/mol)	q (e)
F31, F32 and F33	0.295	0.22175	-0.17
C2	0.35	0.27614	0.12
F21 and F22	0.295	0.22175	-0.13
C4	0.35	0.27614	0.51
F41, F42 and F43	0.295	0.22175	-0.17

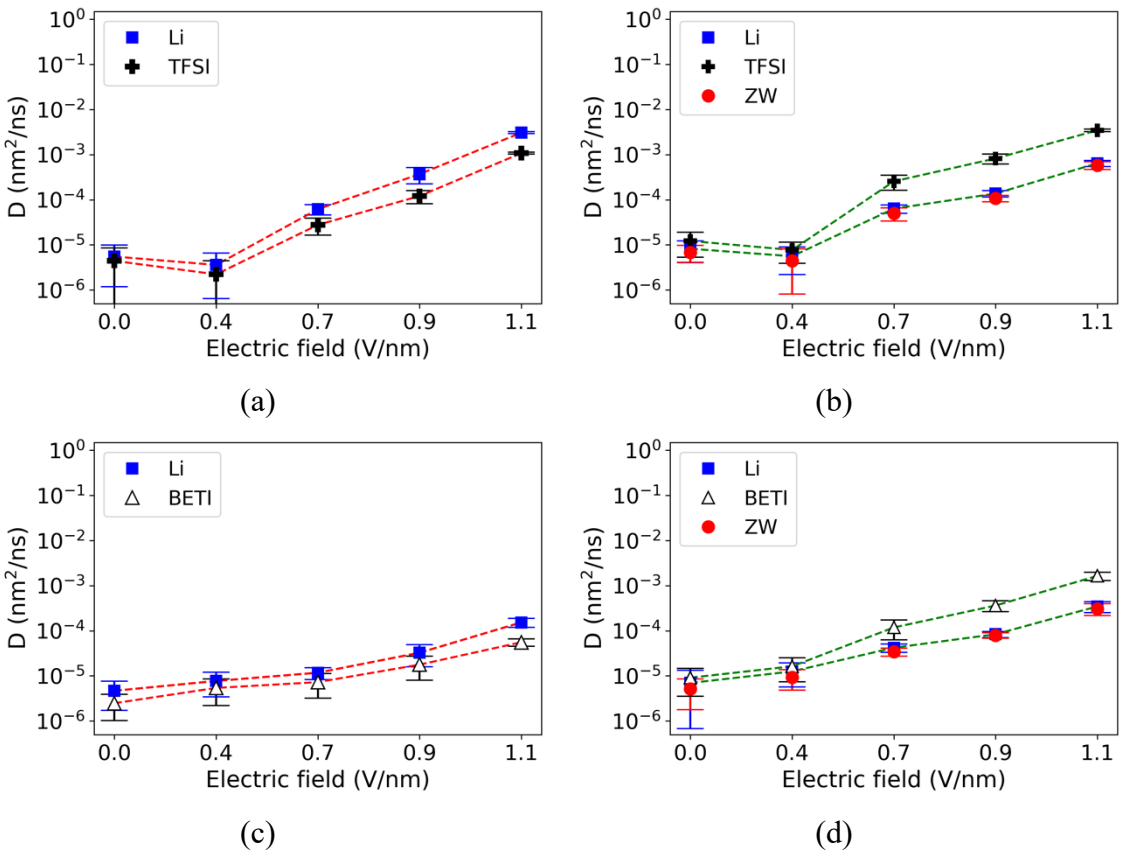

Figure A1. Diffusion coefficients of molecules and ions in electrolytes on the *xy* plane under electric fields (scaled charge) (a) LiTFSI, (b) Z2C/LiTFSI, (c) LiBETI and (d) Z2C/LiBETI

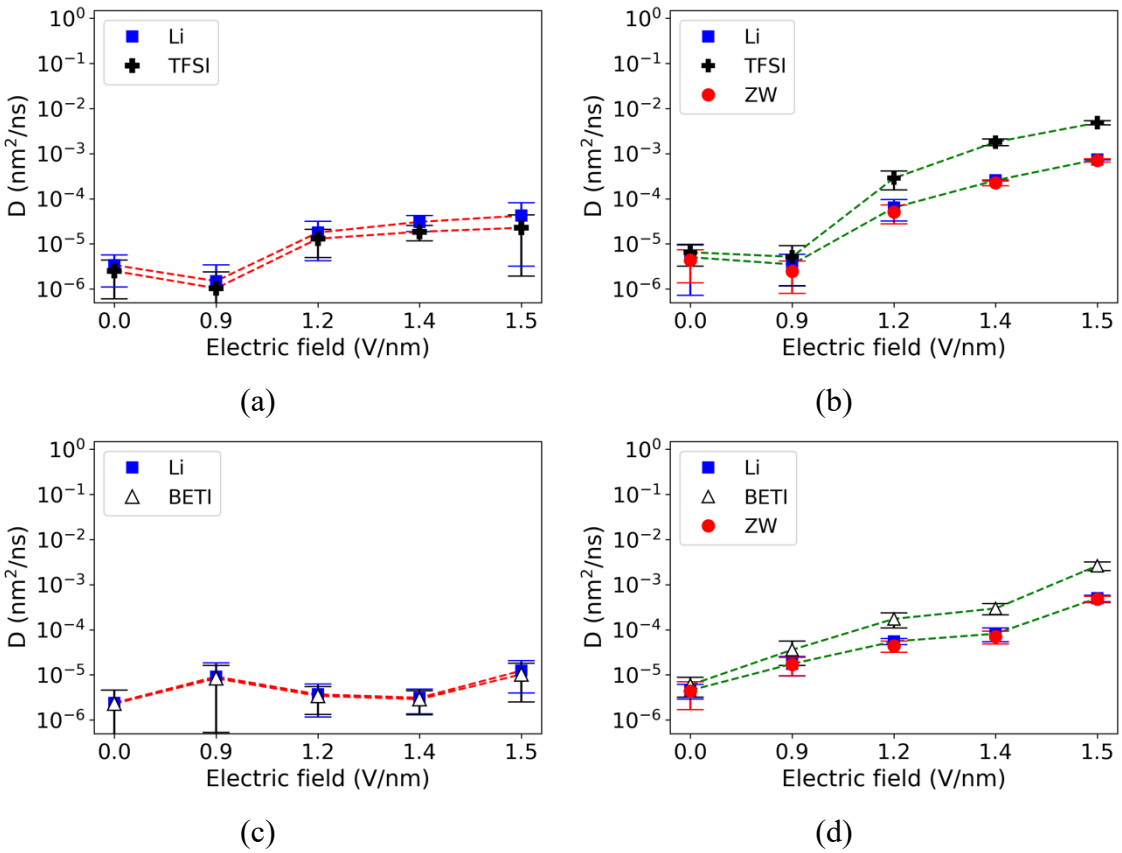

Figure A2. Diffusion coefficients of molecules and ions in electrolytes on the *xy* plane under electric fields (full charge) (a) LiTFSI, (b) Z2C/LiTFSI, (c) LiBETI and (d) Z2C/LiBETI

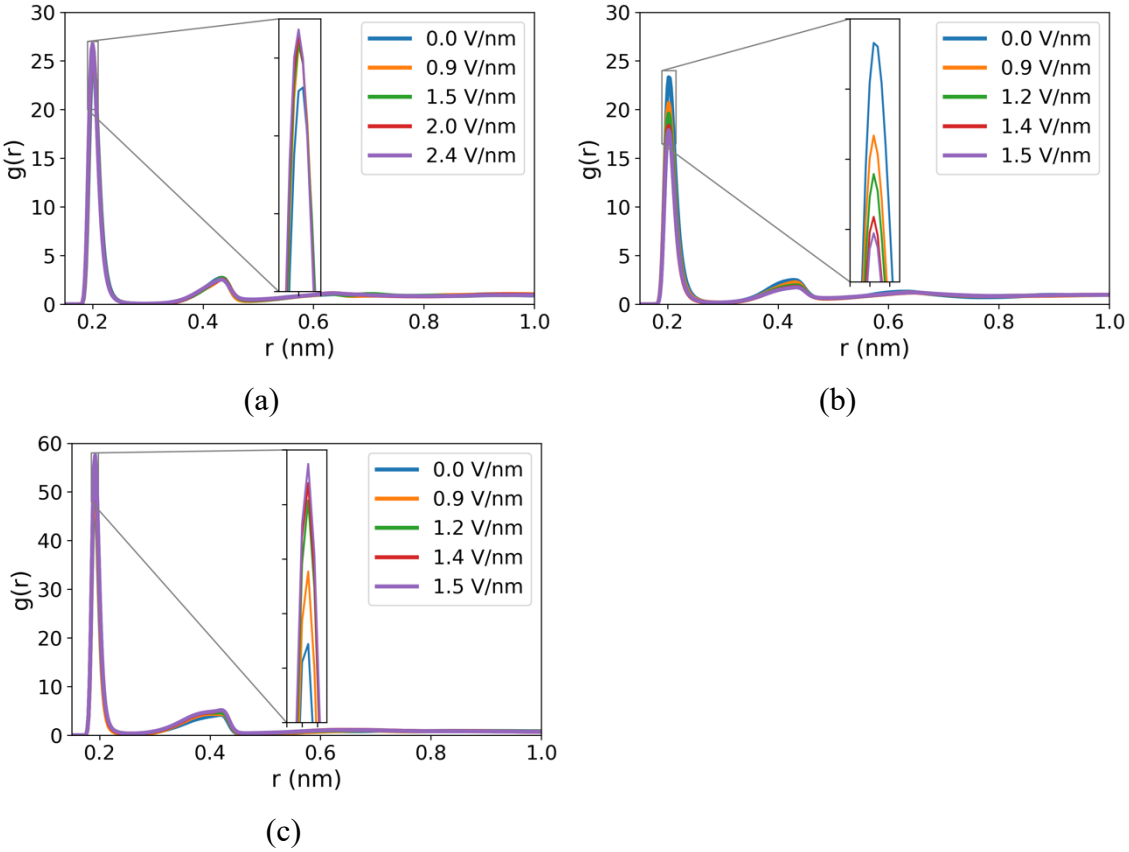

Figure A3. Radial distribution functions in electrolyte solutions (full charge). (a) Li^+-O[BETI]$^-$ in LiBETI solution, (b) Li^+-O[BETI]$^-$ and (c) Li^+-O1(ZW) in Z2C/LiBETI solution.

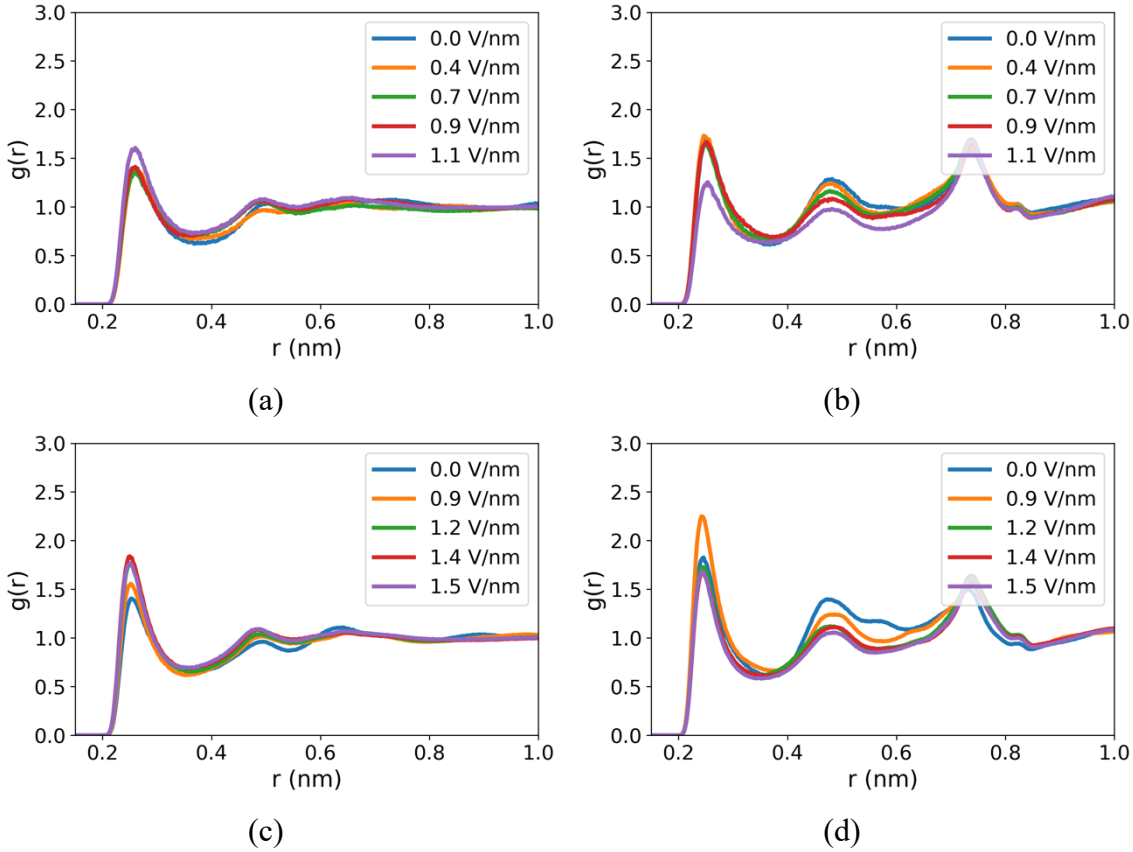

Figure A4. Radial distribution functions among ZW and ions. (a) ZW-[BETI]$^-$ (scaled charge) and (b) ZW-ZW (scaled charge); (c) ZW-[BETI]$^-$ (full charge) and (d) ZW-ZW (full charge)

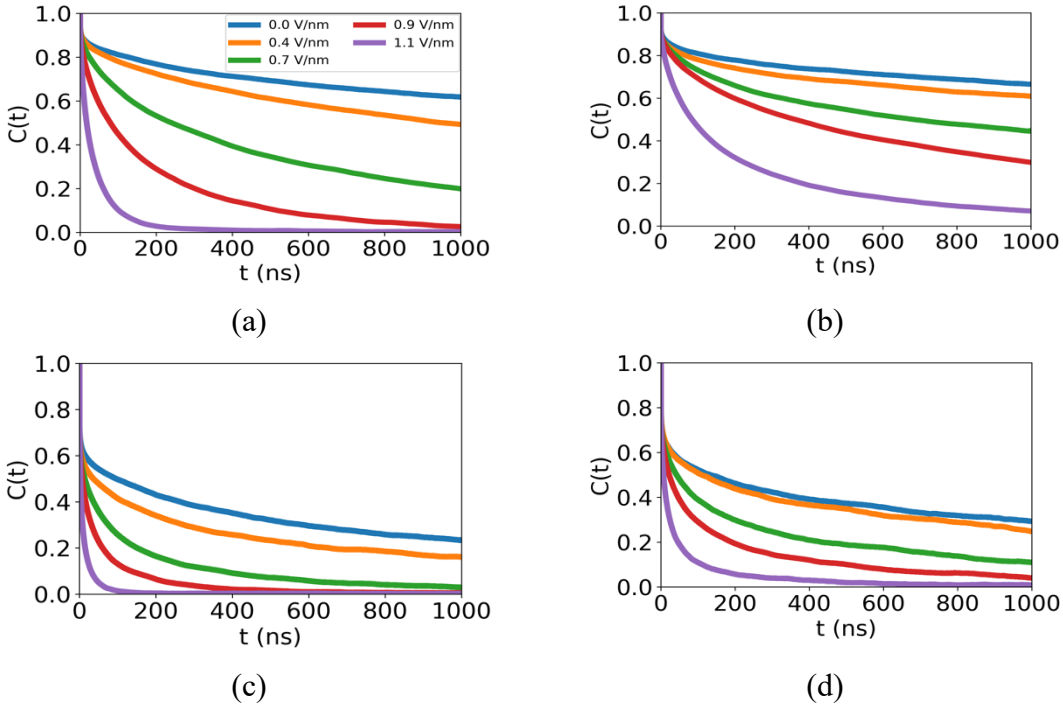

Figure A5. Residence curves C(t) for associations in Z2C/LiBETI systems (scaled charge). (a) Li^+ and $[BETI]^-$, (b) Li^+ and ZW, (c) ZW and $[BETI]^-$; (d) ZW and ZW

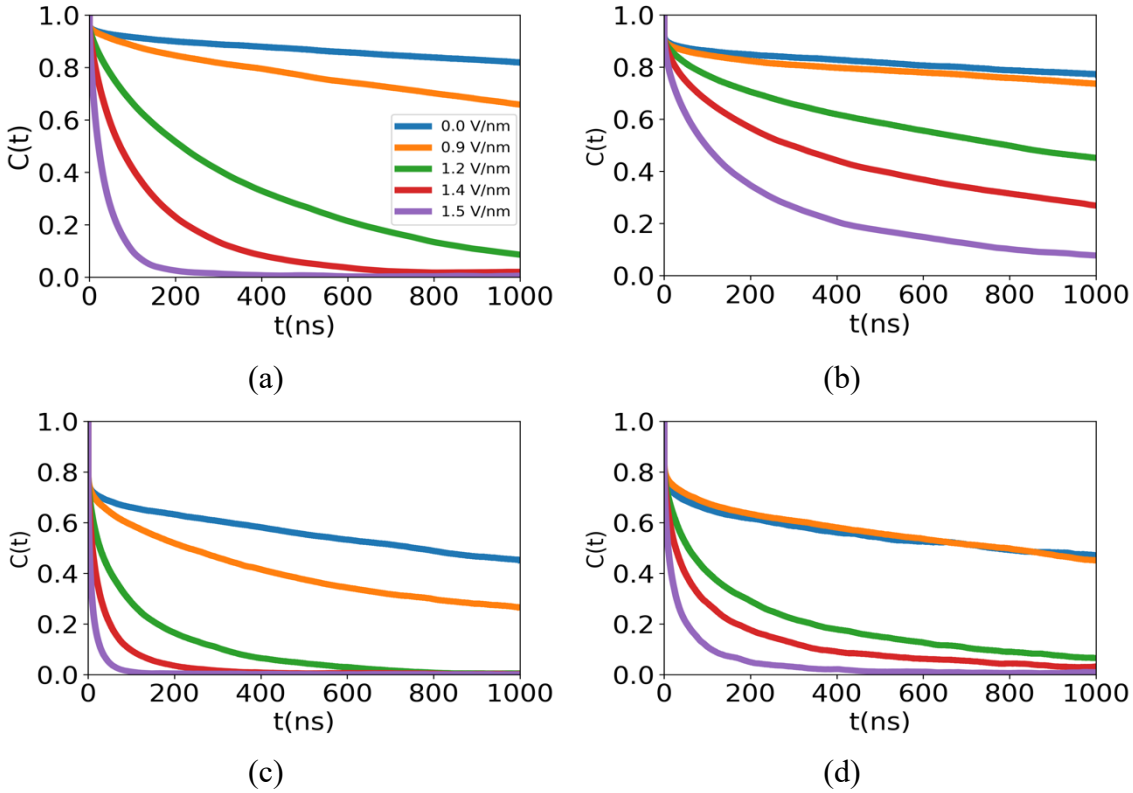

Figure A6. Residence curves C(t) for associations in Z2C/LiBETI systems (full charge). (a) Li^+ and $[BETI]^-$, (b) Li^+ and ZW, (c) ZW and $[BETI]^-$; (d) ZW and ZW

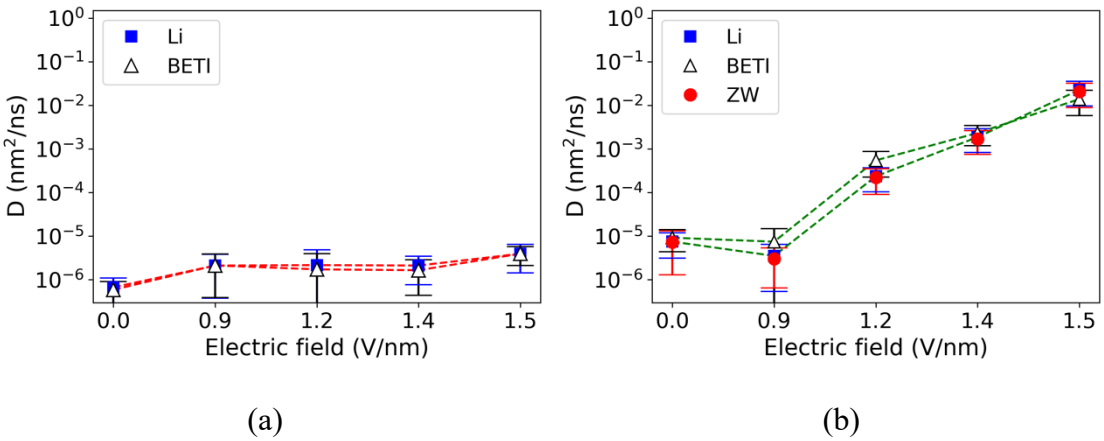

Figure A7. Diffusion coefficients of Li^+, $[BETI]^-$ and zwitterionic Z2C molecules in the z direction as a function of electric field (full charge) (a) LiBETI (b) Z2C/LiBETI

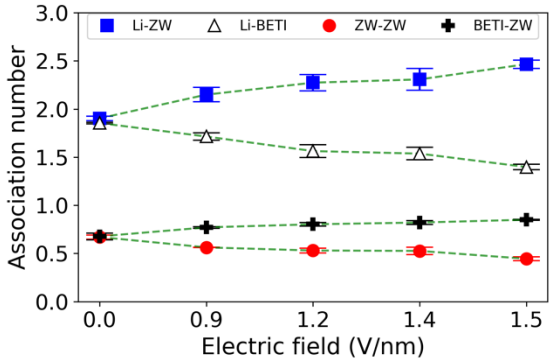

Figure A8. Association numbers in Z2C/LiBETI electrolytes as a function of the electric field (full charge)

APPENDIX 2. SUPPORTING INFORMATION FOR CHAPTER 3

Table B1. Force field parameters for zwitterionic molecules and anions. The labels are shown in Figure 2.1(full charge).

Label	σ (nm)	ε (kJ/mol)	q (e)
ZW			
C1	0.35	0.276144	-0.24
H11, H12 and H13	0.25	0.12552	0.08
C2	0.35	0.276144	-0.17
H21 and H22	0.25	0.12552	0.18
N1	0.325	0.71128	0.22
C3	0.355	0.29288	-0.09
H3	0.242	0.12552	0.21
N2	0.325	0.71128	0.22
C5	0.355	0.29288	-0.24
H5	0.242	0.12552	0.27
C6	0.355	0.29288	-0.24
H6	0.242	0.12552	0.27
C7	0.35	0.276144	-0.17
H71 and H72	0.25	0.12552	0.18
C8	0.350	0.276144	-0.24
H81 and H82	0.250	0.125520	0.1
S	0.355	1.046000	1.32
O1, O2 and O3	0.296	0.711280	-0.76
$[TFSI]^-$			
N	0.325	0.71128	-0.66
S1 and S2	0.355	1.046	1.02
O11, O12, O21 and O22	0.296	0.87864	-0.53

Table B1 (continued). Force field parameters for zwitterionic molecules and anions. The labels are shown in Figure 2.1(full charge).

Label	σ (nm)	ε (kJ/mol)	q (e)
C1 and C2	0.35	0.27614	0.35
F11, F12 and F13	0.295	0.22175	-0.16
F21, F22 and F23	0.295	0.22175	-0.16
EO2/EO3/EO4/EO5			
C1	0.35	0.276144	0.11
H1, H2 and H3	0.25	0.12552	0.03
O4	0.29	0.58576	-0.4
C2	0.35	0.276144	0.14
H4 and H5	0.25	0.12552	0.03
C3	0.35	0.276144	0.14
H6 and H7	0.25	0.12552	0.03
O5	0.29	0.58576	-0.4
C4	0.35	0.276144	0.14
H8 and H9	0.25	0.12552	0.03
C5	0.35	0.276144	0.14
H10 and H11	0.25	0.12552	0.03
O6	0.29	0.58576	-0.4
C6	0.35	0.276144	0.14
H12 and H13	0.25	0.12552	0.03
C7	0.35	0.276144	0.14
H14 and H15	0.25	0.12552	0.03
O7	0.29	0.58576	-0.4
C8	0.35	0.276144	0.14
H16 and H17	0.25	0.12552	0.03
C9	0.35	0.276144	0.14

Table B1 (continued). Force field parameters for zwitterionic molecules and anions. The labels are shown in Figure 2.1(full charge).

Label	σ (nm)	ε (kJ/mol)	q (e)
H18 and H19	0.25	0.12552	0.03
O8	0.29	0.58576	-0.4
C10	0.35	0.276144	0.11
H20, H21 and H22	0.25	0.12552	0.03

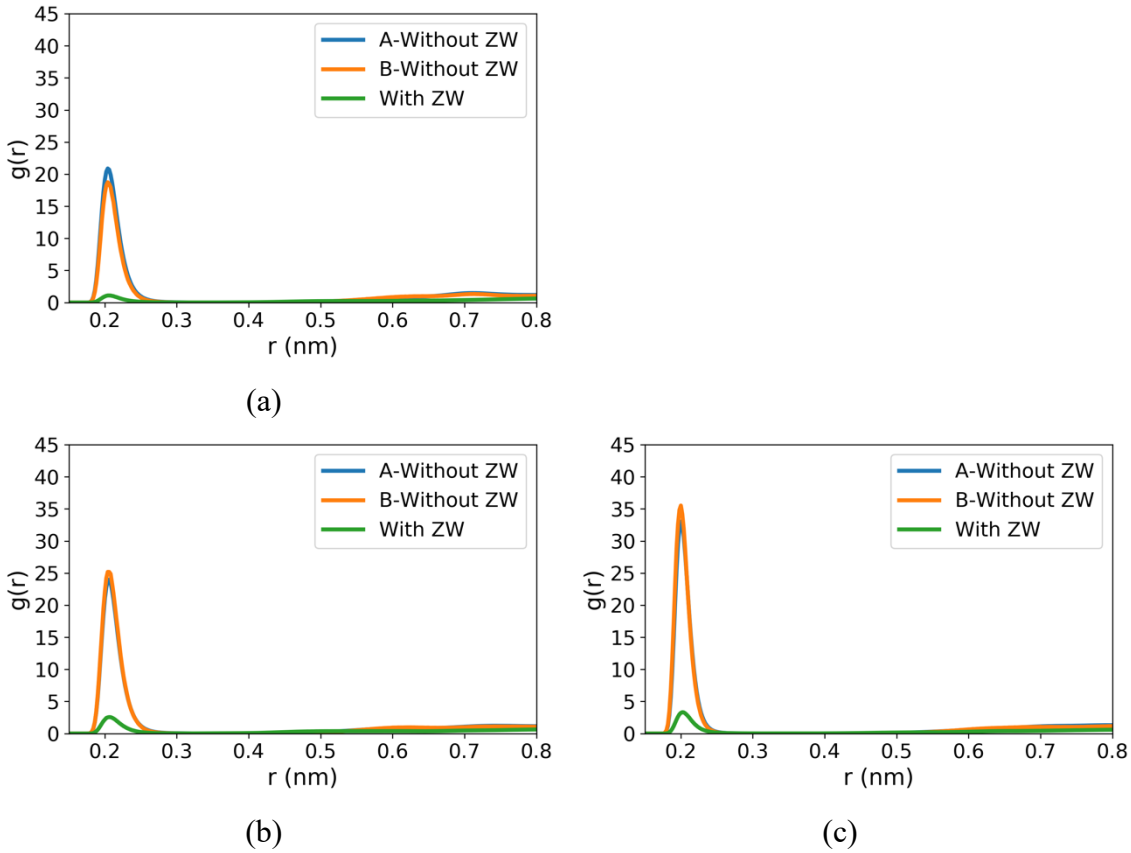

Figure B1. Radial distribution functions (RDFs) of Li^+-O(EOx) with and without ZW(A/B). (a) Li^+-O(EO_x, ter) in EO_2, (b) Li^+-O(EO_x, ter) and (c) Li^+-O(EO_x, mid) in EO_3, (d) Li^+-O(EO_x, ter) and (e) Li^+-O(EO_x, mid) in EO_4, (f) Li^+-O(EO_x, ter) and (g) Li^+-O(EO_x, mid) in EO_5.

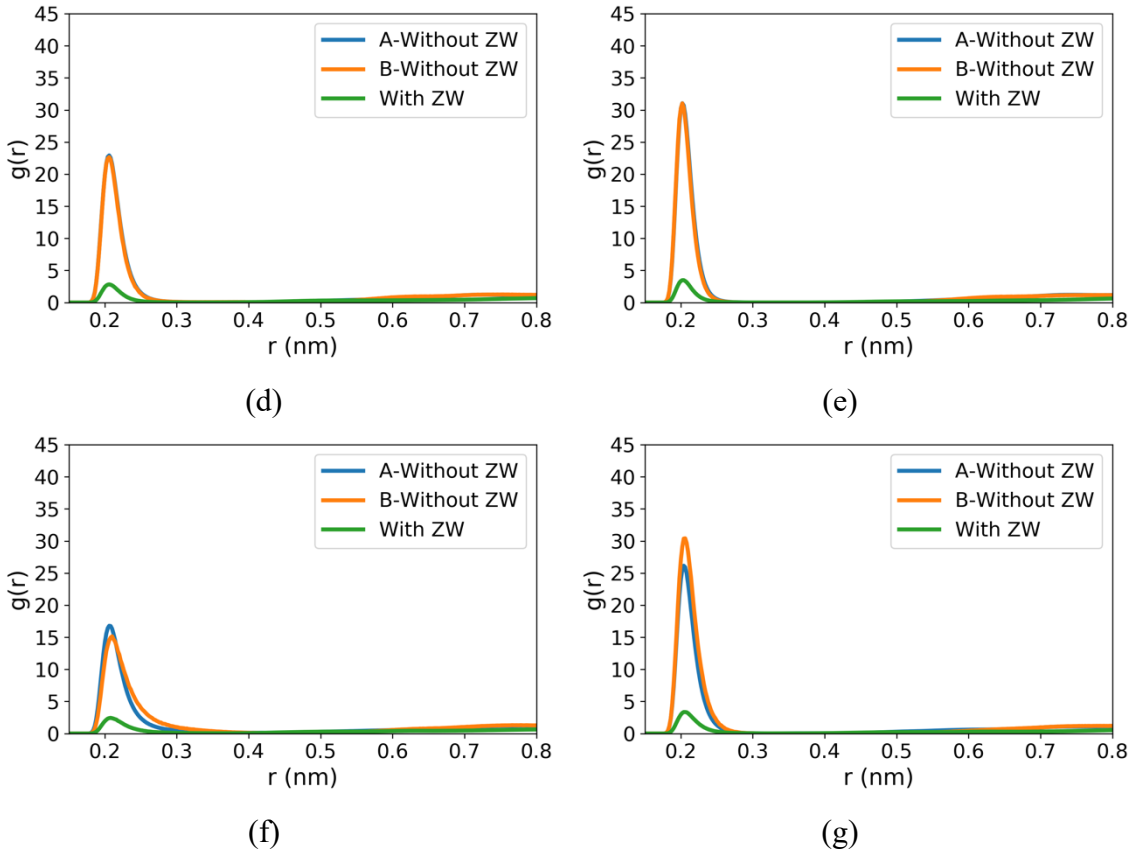

Figure B1 (continued). Radial distribution functions (RDFs) of Li^+-O(EOx) with and without ZW(A/B). (a) Li^+-O(EO_x, ter) in EO_2, (b) Li^+-O(EO_x, ter) and (c) Li^+-O(EO_x, mid) in EO_3, (d) Li^+-O(EO_x, ter) and (e) Li^+-O(EO_x, mid) in EO_4, (f) Li^+-O(EO_x, ter) and (g) Li^+-O(EO_x, mid) in EO_5.

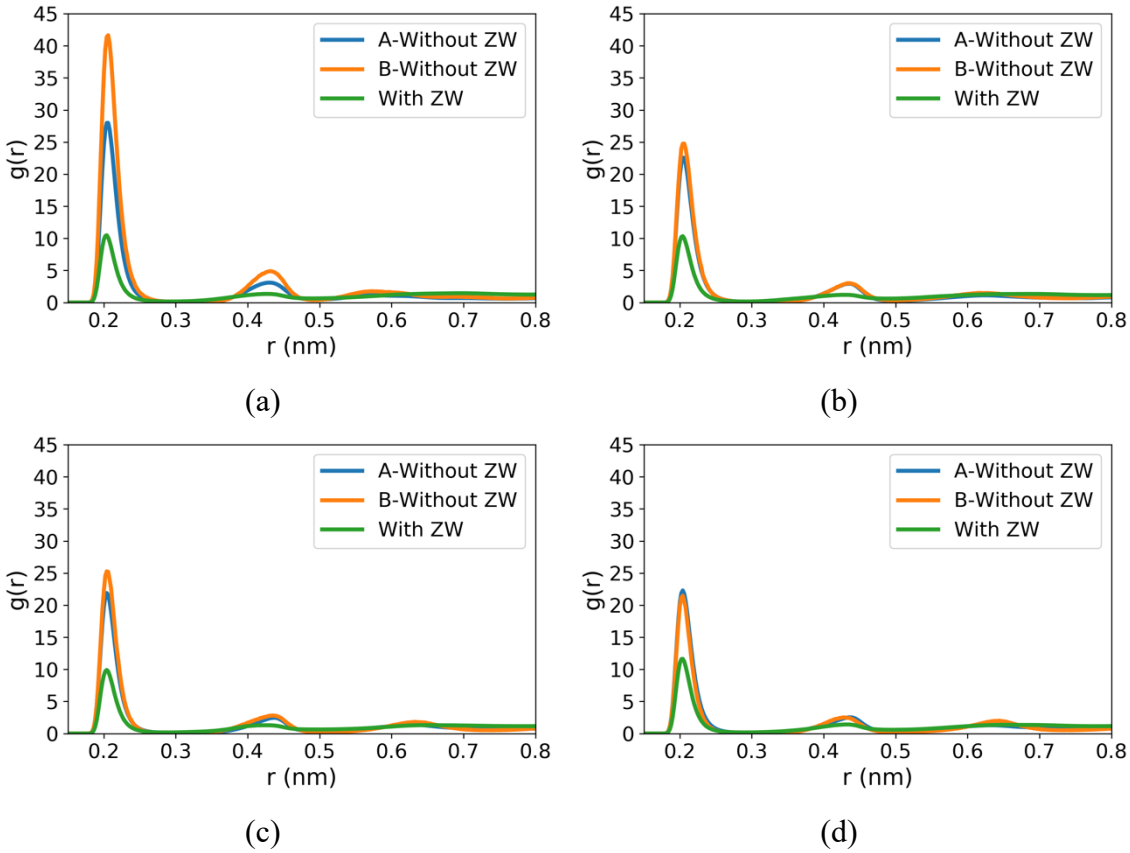

Figure B2. Radial distribution functions (RDFs) of Li^{+}-O11[TFSI]$^{-}$ in the 12 systems with and without ZW (A/B). (a) EO_2, (b) EO_3, (c) EO_4, (d) EO_5

APPENDIX 3. SUPPORTING INFORMATION FOR CHAPTER 4

Table C1. Force field parameters. Labels as shown in Figure 4.1.

Label	σ (nm)	ε (kJ/mol)	q (e)
MPC			
C1	0.355	0.317984	-0.1723
C2	0.355	0.317984	-0.1605
C3	0.35	0.276144	-0.2016
C4	0.355	0.29288	0.4866
C5	0.35	0.276144	-0.0058
C6	0.35	0.276144	0.0849
C7	0.35	0.276144	-0.002
C8	0.35	0.276144	-0.0943
C9	0.35	0.276144	-0.1506
CX	0.35	0.276144	-0.1822
CY	0.35	0.276144	-0.1863
H11, and H12	0.25	0.12552	0.1428
H31, H32, and H33	0.25	0.12552	0.0983
H51, and H52	0.25	0.12552	0.1025
H61, and H62	0.25	0.12552	0.0971
H71, and H72	0.25	0.12552	0.0811
H81, and H82	0.25	0.12552	0.1306
H91, H92, and H93	0.25	0.12552	0.1608
HX1, HX2, and HX3	0.25	0.12552	0.1519
HY1, HY2, and HY3	0.25	0.12552	0.139
N	0.325	0.71128	-0.0123
O1	0.296	0.87864	-0.4613
O2	0.29	0.58576	-0.3565
O3	0.29	0.58576	-0.9069
O4, and O5	0.296	0.87864	-1.1686
O6	0.29	0.58576	-0.8125
P	0.374	0.8368	2.7126
CB			
C	0.355	0.29288	0.486
C1	0.35	0.276144	-0.276
C2	0.35	0.276144	0.023
C3	0.355	0.29288	0.198
C4	0.355	0.29288	-0.074
C5	0.355	0.29288	-0.077
C6	0.35	0.276144	0.002
C7	0.35	0.276144	-0.171
C8	0.35	0.276144	-0.29
H11, H12, and H13	0.25	0.12552	0.119
H21, and H22	0.25	0.12552	0.135
H3	0.242	0.12552	0.347

Table C1 (continued). Force field parameters. Labels as shown in Figure 4.1.

Label	σ (nm)	ε (kJ/mol)	q (e)
H4	0.242	0.12552	0.234
H5	0.242	0.12552	0.242
H61, and H62	0.25	0.12552	0.145
H71, and H72	0.25	0.12552	0.107
H81, and H82	0.25	0.12552	0.088
N1	0.325	0.71128	-0.324
N2	0.325	0.71128	-0.213
O1, and O2	0.296	0.87864	-0.707
SB			
C1	0.35	0.276144	-0.2595
C2	0.35	0.276144	-0.0352
C3	0.355	0.29288	0.0914
C4	0.355	0.29288	-0.1274
C5	0.355	0.29288	-0.08
C6	0.35	0.276144	-0.066
C7	0.35	0.276144	-0.133
C8	0.35	0.276144	-0.6807
H11, H12, and H13	0.25	0.12552	0.1196
H21, and H22	0.25	0.12552	0.1324
H3	0.242	0.12552	0.2719
H4	0.242	0.12552	0.25
H5	0.242	0.12552	0.2744
H61, and H62	0.25	0.12552	0.1318
H71, and H72	0.25	0.12552	0.1279
H81, and H82	0.25	0.12552	0.1329
N1	0.325	0.71128	-0.1837
N2	0.325	0.71128	-0.087
O1, O2, and O3	0.296	0.71128	-0.7122
S	0.355	1.046	1.4926
$[TFSI]^-$			
N	0.325	0.71128	-0.66
S1 and S2	0.355	1.046	1.02
O11, O12, O21 and O22	0.296	0.87864	-0.53
C1 and C2	0.35	0.27614	0.35
F11, F12 and F13	0.295	0.22175	-0.16
F21, F22 and F23	0.295	0.22175	-0.16
EO_{10}			
C1, and C20	0.35	0.276144	0.11
H1-3, and H40-42	0.25	0.12552	0.03
O1-10	0.29	0.58576	-0.4
C2-19	0.35	0.276144	0.14
H4-39	0.25	0.12552	0.03

Table C2. Details of the simulation systems

#	Li^+	$[TFSI]^-$	EO_{10}	ZW	Li^+: $O(EO_{10})$	Mol. conc. (mol/L)	Total number of atoms
Case A:							
1	200	200	120		1:6	2.3	11840
2	200	200	120	40 MPC	1:6	2.3	13480
3	200	200	120	40 CB	1:6	2.4	12920
4	200	200	120	40 SB	1:6	2.4	12960
Case B:							
5	100	100	180		1:18	1.1	14560
6	100	100	180	20 MPC	1:18	1.1	15380
7	100	100	180	20 CB	1:18	1.1	15100
8	100	100	180	20 SB	1:18	1.1	15120

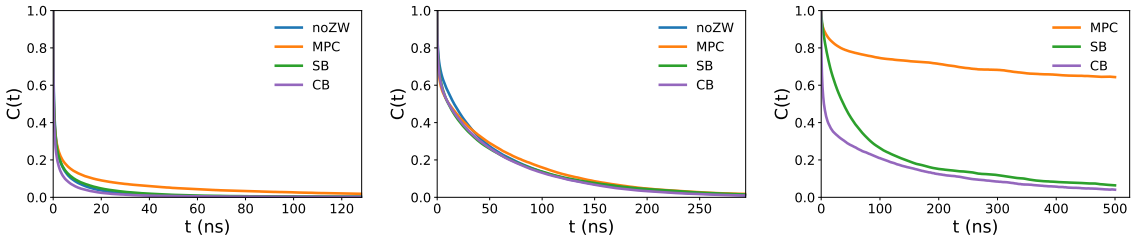

(a) (b) (c)

Figure C1. Residence C(t) curves of (a) Li+-O([TFSI]-) in, (b) Li+-O(EO10) and (c) Li+-O(ZW) in case-A systems at 600K. Colors correspond to the presence of ZW molecules, as shown in the legends in Figure 4.1.

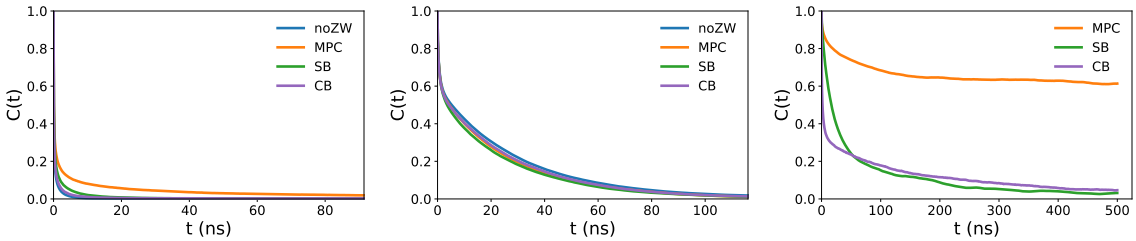

(a) (b) (c)

Figure C2. Residence C(t) curves of (a) Li^+-O($[TFSI]^-$), (b) Li^+-O(EO_{10}) and (c) Li^+-O(ZW) in case-B systems at 600K. Colors correspond to the presence of ZW molecules, as shown in the legends in Figure C2a.

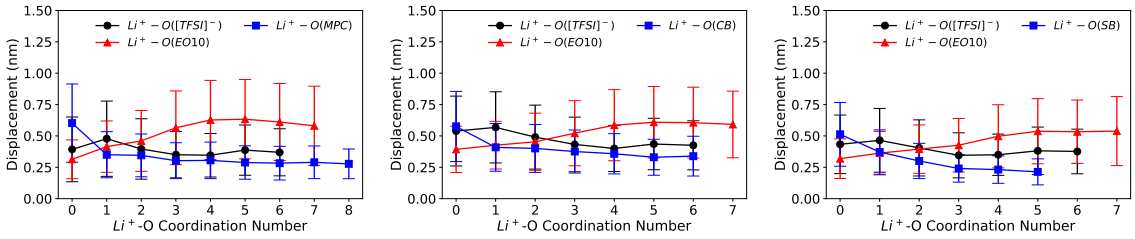

(a) (b) (c)

Figure C3. Distance travelled by Li^+ ions in a specific O coordination number over 2-ns for case-A systems (a) with MPC, (b) with CB, and (c) with SB at 600K.

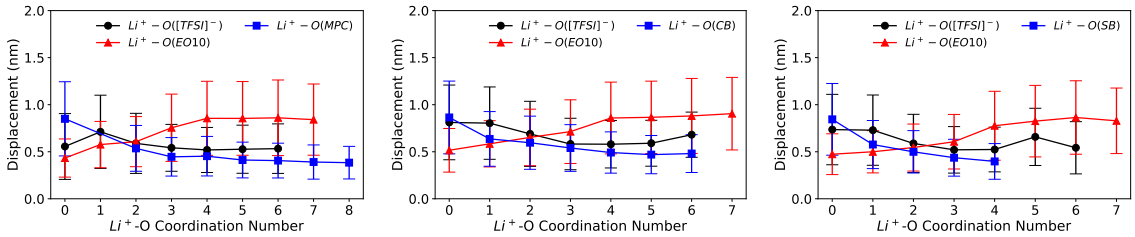

(a) (b) (c)

Figure C4. Distance travelled by Li^+ ions in a specific O coordination number over 1-ns for case-B systems (a) with MPC, (b) with CB, and (c) with SB at 600K.

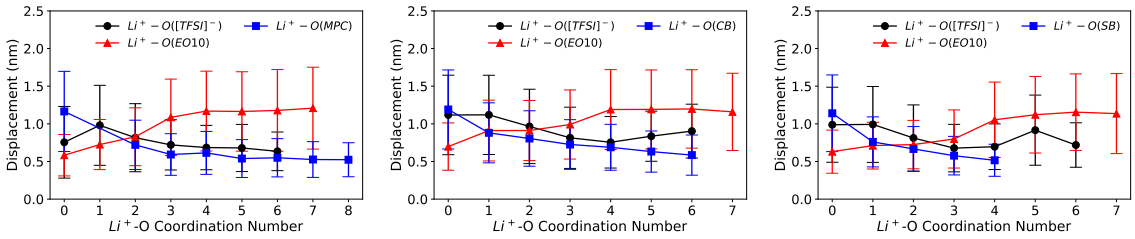

(a) (b) (c)

Figure C5. Distance travelled by Li^+ ions in a specific O coordination number over 2-ns for case-B systems (a) with MPC, (b) with CB, and (c) with SB at 600K.

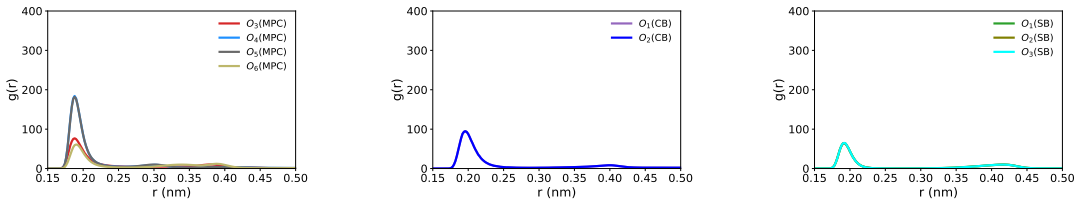

(a) (b) (c)

Figure C6. Radial distribution functions of (a) Li^+-O(MPC), (b) Li^+-O(CB) , and (c) Li^+-O(SB) in case-A systems at 600K. Atom names are the same as in Figure 4.1.

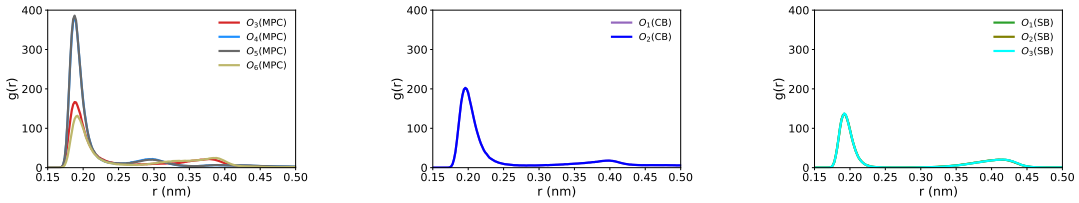

(a) (b) (c)

Figure C7. Radial distribution functions of (a) Li^+-O(MPC), (b) Li^+-O(CB), and (c) Li^+-O(SB) in case-B systems at 600K. Atom names are the same as in Figure 4.1.

Table C3. Diffusion coefficient of Li^+ at 600K (nm^2/ns)

System	noZW	MPC	CB	SB
A	0.019± 0.001	0.019 ± 0.003	0.019 ± 0.001	0.015 ± 0.003
B	0.128 ± 0.018	0.081 ± 0.004	0.099 ± 0.006	0.090 ± 0.005

Table C4. Diffusion coefficient of $[TFSI]^-$ at 600K (nm^2/ns)

System	noZW	MPC	CB	SB
A	0.027 ± 0.002	0.023 ± 0.003	0.030 ± 0.001	0.024 ± 0.004
B	0.161 ± 0.032	0.102 ± 0.003	0.131 ± 0.014	0.131 ± 0.007

Table C5. Diffusion coefficients of ZW at 600K (nm^2/ns)

System	MPC	CB	SB
A	0.007 ± 0.002	0.007 ± 0.001	0.006 ± 0.001
B	0.025 ± 0.008	0.048 ± 0.009	0.045 ± 0.006

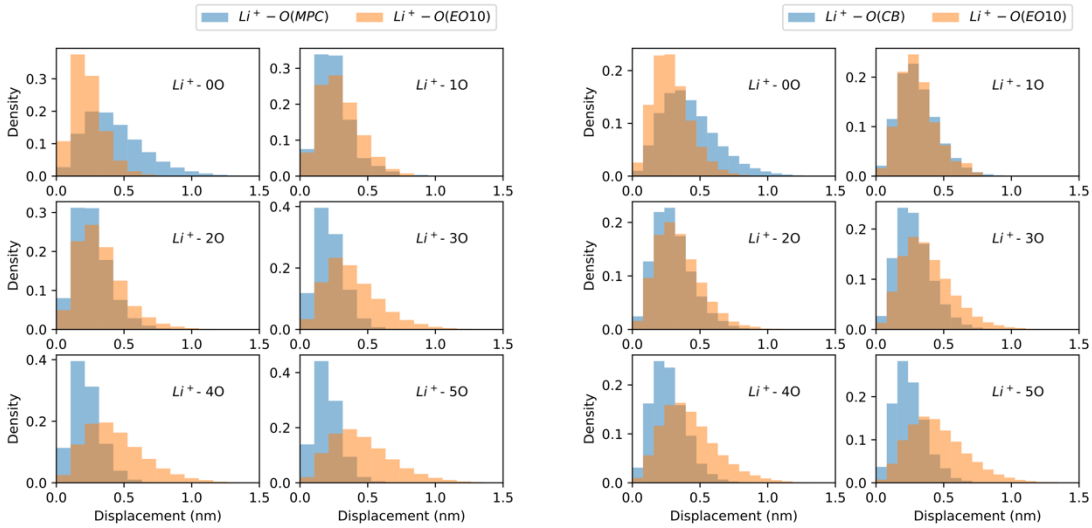

(a)

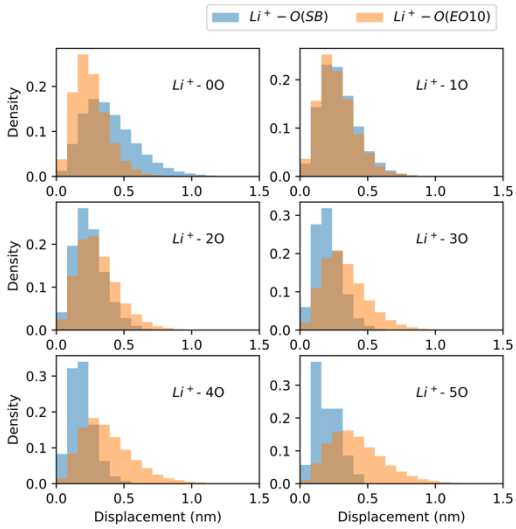

(b)

(c)

Figure C8. Distribution of distance traveled by Li+ ions in a specific O coordination number over 1-ns for systems (a) with MPC, (b) with CB, and (c) with SB in case-A systems at 600K.

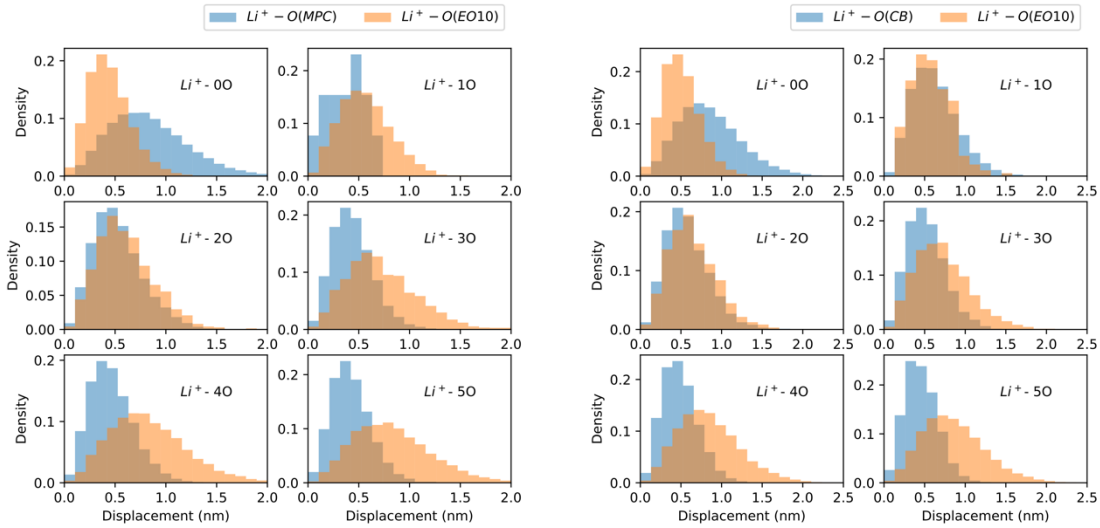

(a)

(b)

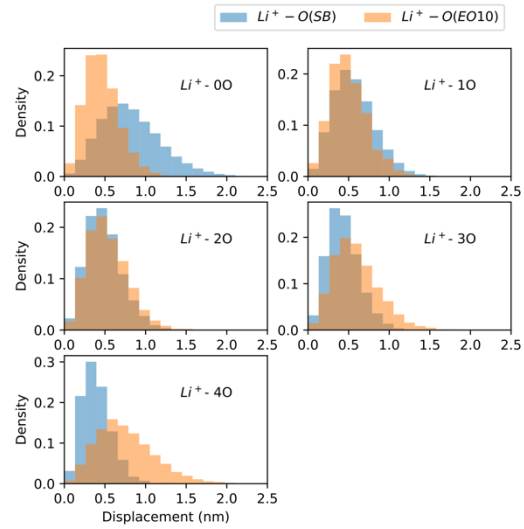

(c)

Figure C9. Distribution of distance traveled by Li^+ ions in a specific O coordination number over 1-ns for systems (a) with MPC, (b) with CB, and (c) with SB in case-B systems at 600K.

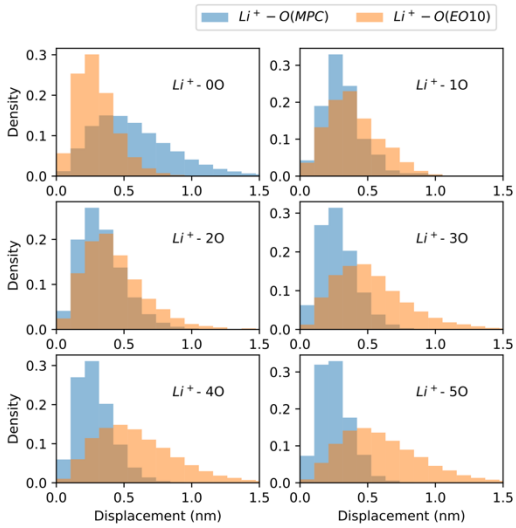

(a)

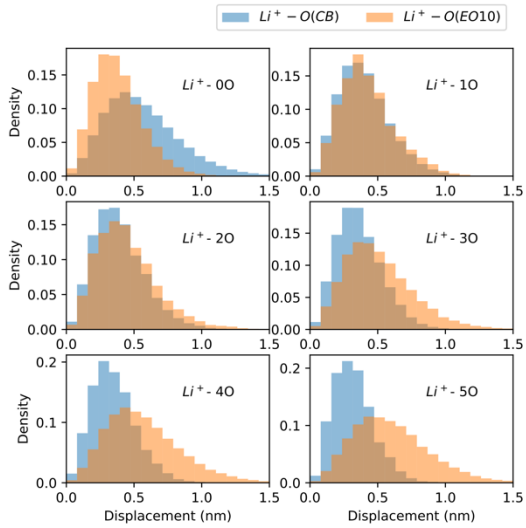

(b)

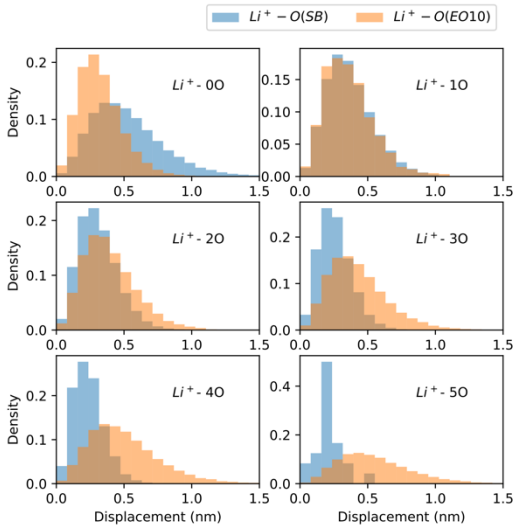

(c)

Figure C10. Distribution of distance traveled by Li^+ ions in a specific O coordination number over 2-ns for systems (a) with MPC, (b) with CB, and (c) with SB in case-A systems at 600K.

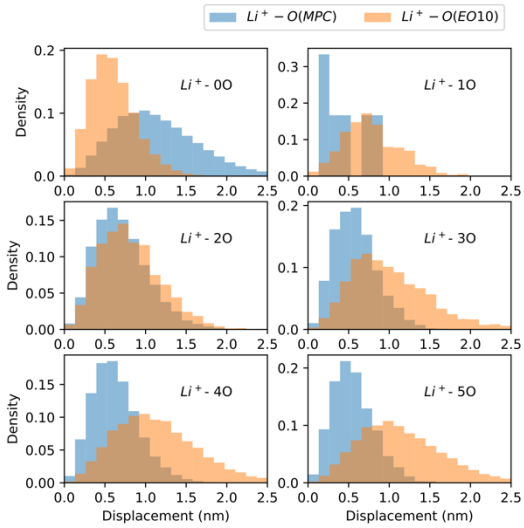

(a)

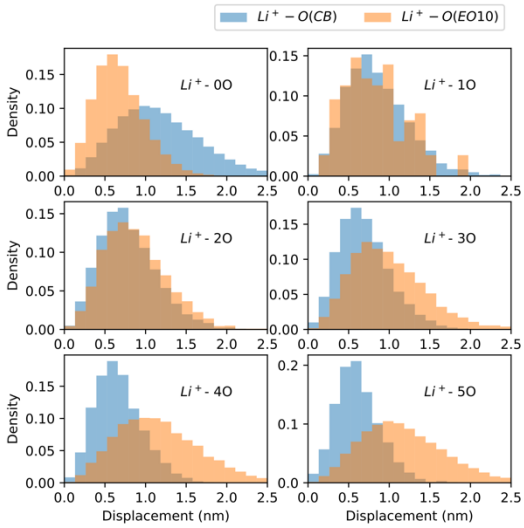

(b)

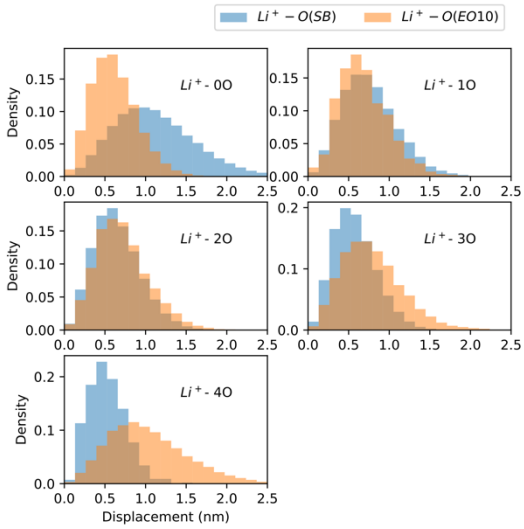

(c)

Figure C11. Distribution of distance traveled by Li+ ions in a specific O coordination number over 2-ns for systems (a) with MPC, (b) with CB, and (c) with SB in case-B systems at 600K.

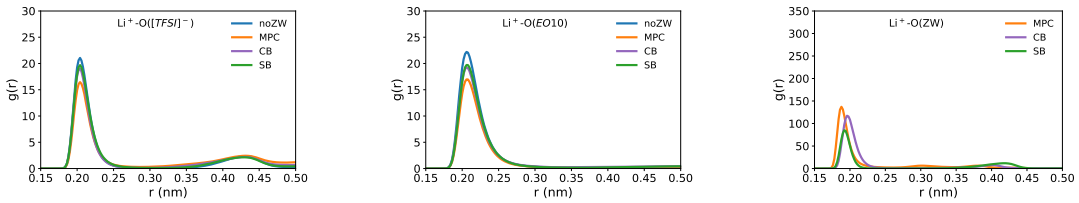

(a) (b) (c)

Figure C12. Radial distribution functions of (a) Li^+-O([TFSI]$^-$), (b) Li^+-O(EO_{10}) and (c) Li^+-O(ZW) in case-A systems at 353K.

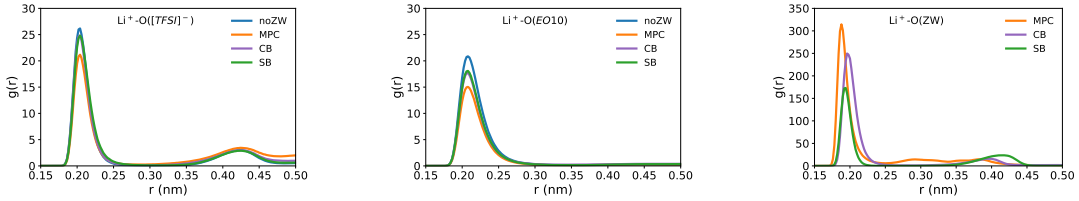

(a) (b) (c)

Figure C13. Radial distribution functions of (a) Li^+-O([TFSI]$^-$), (b) Li^+-O(EO_{10}) and (c) Li^+-O(ZW) in case-B systems at 353K.

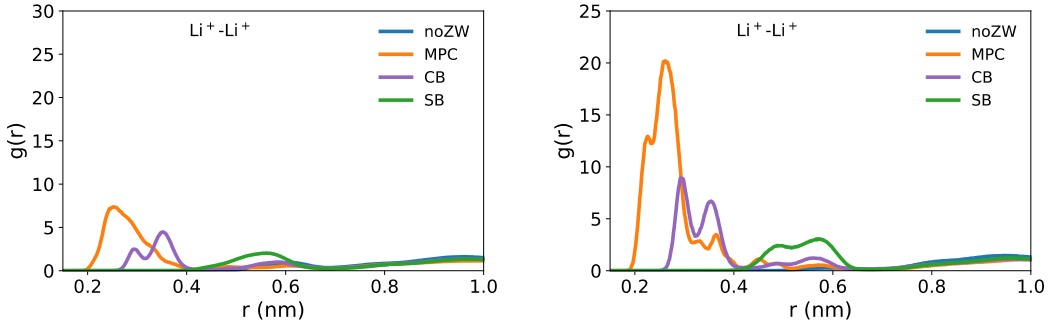

(a) (b)

Figure C14. Radial distribution functions of Li^+-Li^+ in (a) case-A and (b) case-B systems at 353K.

Table C6. Association numbers of Li^+-O in case-A systems at 353K

	No ZW	MPC	SB	CB
Total	6.42 ± 0.01	6.18 ± 0.03	6.09 ± 0.01	6.17 ± 0.02
Li^+-O(ZW)	N/A	1.51 ± 0.05	0.60 ± 0.01	0.78 ± 0.03
Li^+-O([TFSI]$^-$)	1.94 ± 0.03	1.42 ± 0.03	1.72 ± 0.04	1.64 ± 0.02
Li^+-O(EO_{10})	4.47 ± 0.03	3.24 ± 0.02	3.77 ± 0.05	3.75 ± 0.05

Table C7. Association numbers of Li^+-O in case-B systems at 353K

	No ZW	MPC	SB	CB
Total	6.75 ± 0.01	6.42 ± 0.08	6.37 ± 0.01	6.47 ± 0.03
Li^+-O(ZW)	N/A	1.46 ± 0.09	0.58 ± 0.01	0.76 ± 0.03
Li^+-O([TFSI]$^-$)	0.95 ± 0.02	0.74 ± 0.04	0.98 ± 0.04	0.95 ± 0.04
Li^+-O(EO_{10})	5.80 ± 0.03	4.22 ± 0.19	4.81 ± 0.04	4.76 ± 0.08

Table C8. Percentage of Li^+ not coordinating with EO_{10} for systems at 353K

System	CB	MPC	noZW	SB
A	21 ± 3 %	35 ± 1 %	8 ± 1 %	20 ± 2 %
B	10 ± 3 %	23 ± 5 %	0	7 ± 1 %

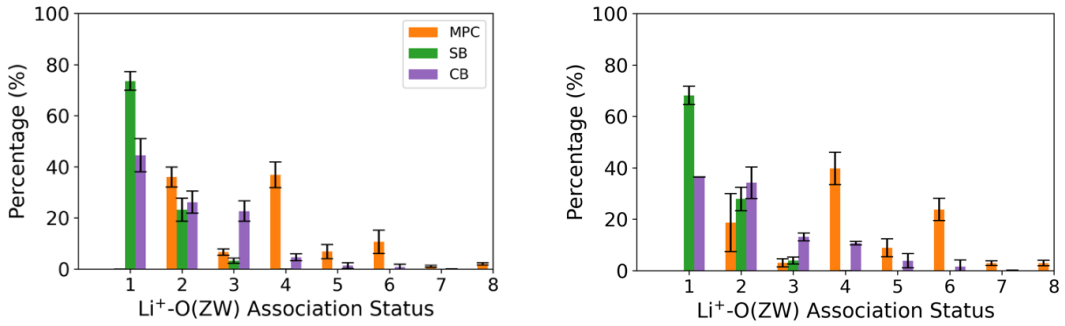

(a) (b)

Figure C15. Association statuses of Li^+-O(ZW) in (a) case-A, and (b) case-B systems 353K. Colors correspond to the presence of ZW molecules, as shown in the legends in Figure C15a.

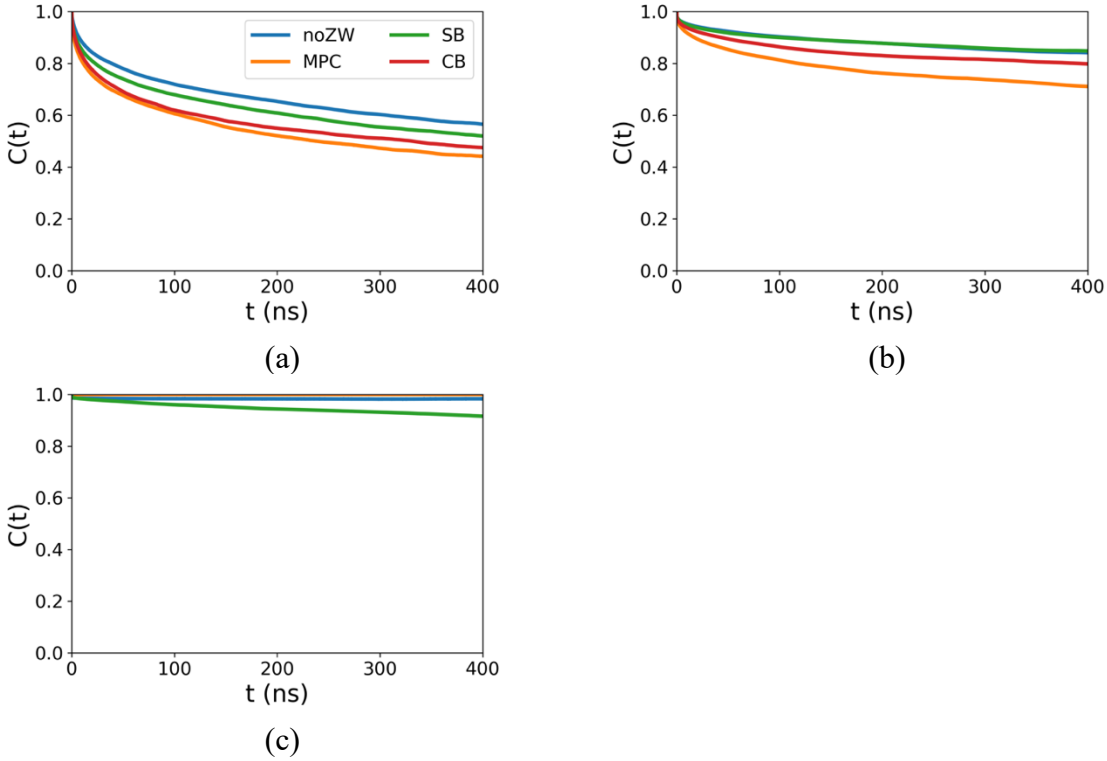

Figure C16. Residence C(t) curves of (a) Li^+-O([TFSI]$^-$) in, (b) Li^+-O(EO_{10}) and (c) Li^+-O(ZW) in case-A systems at 353K. Colors correspond to the presence of ZW molecules, as shown in the legends in Figure C16a.

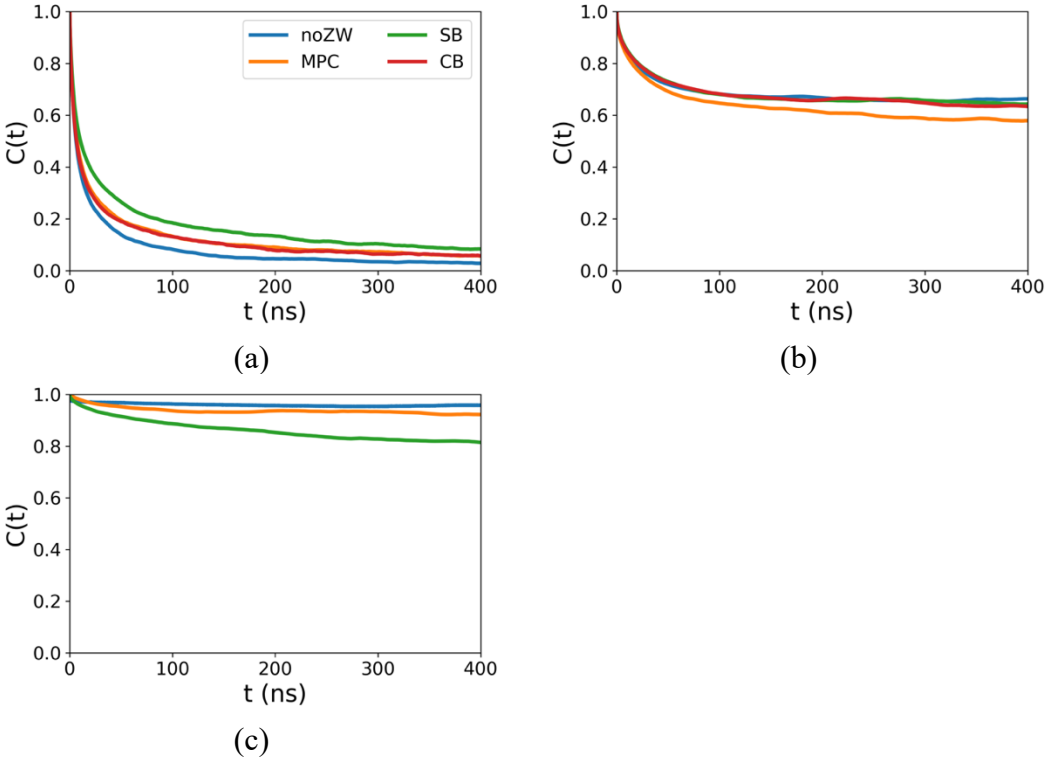

Figure C17. Residence C(t) curves of (a) Li^+-O([TFSI]$^-$), (b) Li^+-O(EO_{10}) and (c) Li^+-O(ZW) in case-B systems at 353K. Colors correspond to the presence of ZW molecules, as shown in the legends in Figure C17a.

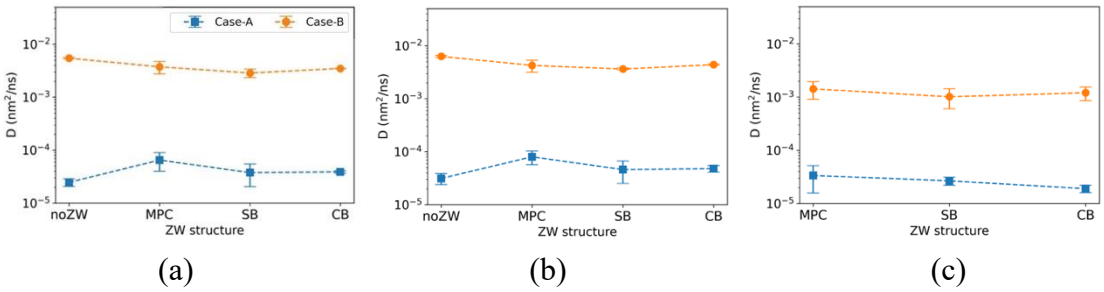

Figure C18. Diffusion coefficients of (a) Li^+, (b) [TFSI]$^-$, and (c) ZW for systems at 353K. Colors correspond to the Li^+:O(EO_{10}) molar ratios - r, as shown in the legends in Figure C18a.

REFERENCES

1 M. Armand and J.-M. Tarascon, Building better batteries, *Nature*, 2008, **451**, 652–657.

2 Z. Gao, H. Sun, L. Fu, F. Ye, Y. Zhang, W. Luo and Y. Huang, Promises, Challenges, and Recent Progress of Inorganic Solid-State Electrolytes for All-Solid-State Lithium Batteries, *Adv. Mater.*, 2018, **30**, 1705702.

3 A. Manthiram, An outlook on lithium ion battery technology, *ACS Cent. Sci.*, 2017, **3**, 1063–1069.

4 J. Gibbins and H. Chalmers, Carbon capture and storage, *Energy Policy*, 2008, **36**, 4317–4322.

5 Q. Zhao, S. Stalin, C.-Z. Zhao and L. A. Archer, Designing solid-state electrolytes for safe, energy-dense batteries, *Nat. Rev. Mater.*, 2020, **5**, 229–252.

6 A. Manthiram, X. Yu and S. Wang, Lithium battery chemistries enabled by solid-state electrolytes, *Nat. Rev. Mater.*, , DOI:10.1038/natrevmats.2016.103.

7 K. Murata, S. Izuchi and Y. Yoshihisa, Overview of the research and development of solid polymer electrolyte batteries, *Electrochim. Acta*, 2000, **45**, 1501–1508.

8 J.-C. Daigle, A. Vijh, P. Hovington, C. Gagnon, J. Hamel-Pâquet, S. Verreault, N. Turcotte, D. Clément, A. Guerfi and K. Zaghib, Lithium battery with solid polymer electrolyte based on comb-like copolymers, *J. Power Sources*, 2015, **279**, 372–383.

9 X.-X. Zeng, Y.-X. Yin, N.-W. Li, W.-C. Du, Y.-G. Guo and L.-J. Wan, Reshaping lithium plating/stripping behavior via bifunctional polymer electrolyte for room-temperature solid Li metal batteries, *J. Am. Chem. Soc.*, 2016, **138**, 15825–15828.

10 M. S. Whittingham, Lithium batteries and cathode materials, *Chem. Rev.*, 2004, **104**, 4271–4301.

11 B. Kumar and L. G. Scanlon, Polymer-ceramic composite electrolytes, *J. Power Sources*, 1994, **52**, 261–268.

12 R. Chen, W. Qu, X. Guo, L. Li and F. Wu, The pursuit of solid-state electrolytes for lithium batteries: From comprehensive insight to emerging horizons, *Mater. Horizons*, 2016, **3**, 487–516.

13 W. Liu, S. W. Lee, D. Lin, F. Shi, S. Wang, A. D. Sendek and Y. Cui, Enhancing ionic conductivity in composite polymer electrolytes with well-aligned ceramic nanowires, *Nat. energy*, 2017, **2**, 1–7.

14 M. Dirican, C. Yan, P. Zhu and X. Zhang, Composite solid electrolytes for all-solid-state lithium batteries, *Mater. Sci. Eng. R Reports*, 2019, **136**, 27–46.

15 M. S. Michael, M. M. E. Jacob, S. R. S. Prabaharan and S. Radhakrishna, Enhanced lithium ion transport in PEO-based solid polymer electrolytes employing a novel class of plasticizers, *Solid State Ionics*, 1997, **98**, 167–174.

16 J. Y. Song, Y. Y. Wang and C. C. Wan, Review of gel-type polymer electrolytes for lithium-ion batteries, *J. Power Sources*, 1999, **77**, 183–197.

17 W. Young, W. Kuan and T. H. Epps III, Block copolymer electrolytes for rechargeable lithium batteries, *J. Polym. Sci. Part B Polym. Phys.*, 2014, **52**, 1–16.

18 L. Long, S. Wang, M. Xiao and Y. Meng, Polymer electrolytes for lithium polymer batteries, *J. Mater. Chem. A*, 2016, **4**, 10038–10039.

19 M. L. Lehmann, G. Yang, J. Nanda and T. Saito, Well-designed crosslinked polymer electrolyte enables high ionic conductivity and enhanced salt solvation, *J. Electrochem. Soc.*, 2020, **167**, 70539.

20 Z. Lin, X. Guo, Y. Yang, M. Tang, Q. Wei and H. Yu, Block copolymer electrolyte with adjustable functional units for solid polymer lithium metal battery, *J. Energy Chem.*, 2021, **52**, 67–74.

21 A. B. Lowe and C. L. McCormick, Synthesis and Solution Properties of Zwitterionic Polymers, *Chem. Rev.*, 2002, **102**, 4177–4190.

22 Y. Liu, D. Zhang, B. Ren, X. Gong, L. Xu, Z. Q. Feng, Y. Chang, Y. He and J. Zheng, Molecular simulations and understanding of antifouling zwitterionic polymer brushes, *J. Mater. Chem. B*, 2020, **8**, 3814–3828.

23 Q. Shao, A computational avenue towards understanding and design of zwitterionic anti-biofouling materials, *Mol. Simul.*, 2019, **45**, 1211–1222.

24 Q. Shao, Y. He and S. Jiang, Molecular Dynamics Simulation Study of Ion Interactions with Zwitterions, *J. Phys. Chem. B*, 2011, **115**, 8358–8363.

25 Q. Shao and S. Jiang, Effect of carbon spacer length on zwitterionic carboxybetaines, *J. Phys. Chem. B*, 2013, **117**, 1357–1366.

26 Q. Shao, L. Mi, X. Han, T. Bai, S. Liu, Y. Li and S. Jiang, Differences in cationic and anionic charge densities dictate zwitterionic associations and stimuli responses, *J. Phys. Chem. B*, 2014, **118**, 6956–6962.

27 A. J. D'Angelo and M. J. Panzer, Decoupling the Ionic Conductivity and Elastic Modulus of Gel Electrolytes: Fully Zwitterionic Copolymer Scaffolds in Lithium Salt/Ionic Liquid Solutions, *Adv. Energy Mater.*, 2018, **8**, 1–13.

28 F. Lind, L. Rebollar, P. Bengani-Lutz, A. Asatekin and M. J. Panzer, Zwitterion-Containing Ionogel Electrolytes, *Chem. Mater.*, 2016, **28**, 8480–8483.

29 M. E. Taylor and M. J. Panzer, Fully-Zwitterionic Polymer-Supported Ionogel Electrolytes Featuring a Hydrophobic Ionic Liquid, *J. Phys. Chem. B*, 2018, **122**, 8469–8476.

30 M. E. Taylor, D. Clarkson, S. G. Greenbaum and M. J. Panzer, Examining the

Impact of Polyzwitterion Chemistry on Lithium Ion Transport in Ionogel Electrolytes, *ACS Appl. Polym. Mater.*, 2021, **3**, 2635–2645.

31 S. D. Jones, H. Nguyen, P. M. Richardson, Y.-Q. Chen, K. E. Wyckoff, C. J. Hawker, R. J. Clément, G. H. Fredrickson and R. A. Segalman, Design of Polymeric Zwitterionic Solid Electrolytes with Superionic Lithium Transport, *ACS Cent. Sci.*, 2022, **8**, 169–175.

32 J. Ning, G. Li and K. Haraguchi, Synthesis of highly stretchable, mechanically tough, zwitterionic sulfobetaine nanocomposite gels with controlled thermosensitivities, *Macromolecules*, 2013, **46**, 5317–5328.

33 A. J. D'Angelo and M. J. Panzer, Design of Stretchable and Self-Healing Gel Electrolytes via Fully Zwitterionic Polymer Networks in Solvate Ionic Liquids for Li-Based Batteries, *Chem. Mater.*, 2019, **31**, 2913–2922.

34 K. D. Fong, J. Self, B. D. McCloskey and K. A. Persson, Ion correlations and their impact on transport in polymer-based electrolytes, *Macromolecules*, 2021, **54**, 2575–2591.

35 Z. Zhu and S. J. Paddison, Perspective: Morphology and ion transport in ion-containing polymers from multiscale modeling and simulations, *Front. Chem.*, 2022, **10**, 981508.

36 D. J. Siegel, L. Nazar, Y.-M. Chiang, C. Fang and N. P. Balsara, Establishing a unified framework for ion solvation and transport in liquid and solid electrolytes, *Trends Chem.*, 2021, **3**, 807–818.

37 M. J. Deck and Y.-Y. Hu, Leveraging local structural disorder for enhanced ion transport, *J. Mater. Res.*, 2023, **38**, 2631–2644.

38 J. Buckingham, T. R. Reina and M. S. Duyar, Recent advances in carbon dioxide capture for process intensification, *Carbon Capture Sci. Technol.*, 2022, 100031.

39 N. P. D. Sawaya, F. Paesani and D. P. Tabor, Near- and long-term quantum algorithmic approaches for vibrational spectroscopy, *Phys. Rev. A*, 2021, **104**, 062419.

40 G. Ortiz, J. E. Gubernatis, E. Knill and R. Laflamme, Quantum algorithms for fermionic simulations, *Phys. Rev. A*, 2001, **64**, 022319.

41 H. P. Paudel, M. Syamlal, S. E. Crawford, Y.-L. Lee, R. A. Shugayev, P. Lu, P. R. Ohodnicki, D. Mollot and Y. Duan, Quantum Computing and Simulations for Energy Applications: Review and Perspective, *ACS Eng. Au*, 2022, **2**, 151–196.

42 J. Tilly, H. Chen, S. Cao, D. Picozzi, K. Setia, Y. Li, E. Grant, L. Wossnig, I. Rungger, G. H. Booth and J. Tennyson, The Variational Quantum Eigensolver: A review of methods and best practices, *Phys. Rep.*, 2022, **986**, 1–128.

43 O. Higgott, D. Wang and S. Brierley, Variational Quantum Computation of Excited States, *Quantum*, 2019, **3**, 156.

44 C. Hempel, C. Maier, J. Romero, J. McClean, T. Monz, H. Shen, P. Jurcevic, B. P. Lanyon, P. Love, R. Babbush, A. Aspuru-Guzik, R. Blatt and C. F. Roos, Quantum Chemistry Calculations on a Trapped-Ion Quantum Simulator, *Phys. Rev. X*, 2018, **8**, 031022.

45 P. J. Ollitrault, A. Baiardi, M. Reiher and I. Tavernelli, Hardware efficient quantum algorithms for vibrational structure calculations, *Chem. Sci.*, 2020, **11**, 6842–6855.

46 N. P. D. Sawaya and J. Huh, Quantum Algorithm for Calculating Molecular Vibronic Spectra, *J. Phys. Chem. Lett.*, 2019, **10**, 3586–3591.

47 S. McArdle, A. Mayorov, X. Shan, S. Benjamin and X. Yuan, Digital quantum simulation of molecular vibrations, *Chem. Sci.*, 2019, **10**, 5725–5735.

48 Z. Gao, H. Sun, L. Fu, F. Ye, Y. Zhang, W. Luo and Y. Huang, Promises, challenges, and recent progress of inorganic solid-state electrolytes for all-solid-state lithium batteries, *Adv. Mater.*, 2018, **30**, 1705702.

49 T. F. Miller, Z. G. Wang, G. W. Coates and N. P. Balsara, Designing polymer electrolytes for safe and high capacity rechargeable lithium batteries, *Acc. Chem. Res.*, 2017, **50**, 590–593.

50 B. Dunn, H. Kamath and J.-M. Tarascon, Electrical energy storage for the grid: a battery of choices, *Science (80-.).*, 2011, **334**, 928–935.

51 S. Muench, A. Wild, C. Friebe, B. Häupler, T. Janoschka and U. S. Schubert, Polymer-Based Organic Batteries, *Chem. Rev.*, 2016, **116**, 9438–9484.

52 W. Qian, J. Texter and F. Yan, Frontiers in poly(ionic liquid)s: Syntheses and applications, *Chem. Soc. Rev.*, 2017, **46**, 1124–1159.

53 W. H. Meyer, Polymer electrolytes for lithium-ion batteries, *Adv. Mater.*, 1998, **10**, 439–448.

54 H. Ohno, M. Yoshizawa and W. Ogihara, A new type of polymer gel electrolyte: zwitterionic liquid/polar polymer mixture, *Electrochim. Acta*, 2003, **48**, 2079–2083.

55 C. Tiyapiboonchaiya, J. M. Pringle, J. Sun, N. Byrne, P. C. Howlett, D. R. MacFarlane and M. Forsyth, The zwitterion effect in high-conductivity polyelectrolyte materials, *Nat. Mater.*, 2004, **3**, 29–32.

56 H. Ohno, M. Yoshizawa-Fujita and Y. Kohno, Design and properties of functional zwitterions derived from ionic liquids, *Phys. Chem. Chem. Phys.*, 2018, **20**, 10978–10991.

57 A. Islam, J. Li, M. Pervaiz, Z.-H. Lu, M. Sain, L. Chen and X. Ouyang, Zwitterions for Organic/Perovskite Solar Cells, Light-Emitting Devices, and Lithium Ion Batteries: Recent Progress and Perspectives, *Adv. Energy Mater.*, 2019, **9**, 1803354.

58 Q. Shao and S. Jiang, Molecular Understanding and Design of Zwitterionic Materials, *Adv. Mater.*, 2015, **27**, 15–26.

59 H. S. Sundaram, J.-R. Ella-Menye, N. D. Brault, Q. Shao and S. Jiang, Reversibly

switchable polymer with cationic/zwitterionic/anionic behavior through synergistic protonation and deprotonation, *Chem. Sci.*, 2014, **5**, 200–205.

60 Q. Shao and S. Jiang, Influence of charged groups on the properties of zwitterionic moieties: a molecular simulation study, *J. Phys. Chem. B*, 2014, **118**, 7630–7637.

61 M. Yoshizawa, M. Hirao, K. Ito-Akita and H. Ohno, Ion conduction in zwitterionic-type molten salts and their polymers, *J. Mater. Chem.*, 2001, **11**, 1057–1062.

62 L. Rebollar and M. J. Panzer, Zwitterionic Copolymer-Supported Ionogel Electrolytes: Impacts of Varying the Zwitterionic Group and Ionic Liquid Identities, *ChemElectroChem*, 2019, **6**, 2482–2488.

63 N. Byrne, P. C. Howlett, D. R. MacFarlane and M. Forsyth, The zwitterion effect in ionic liquids: Towards practical rechargeable lithium-metal batteries, *Adv. Mater.*, 2005, **17**, 2497–2501.

64 N. Byrne, P. C. Howlett, D. R. MacFarlane, M. E. Smith, A. Howes, A. F. Hollenkamp, T. Bastow, P. Hale and M. Forsyth, Effect of zwitterion on the lithium solid electrolyte interphase in ionic liquid electrolytes, *J. Power Sources*, 2008, **184**, 288–296.

65 S. Yamaguchi, M. Yoshizawa-Fujita, H. Zhu, M. Forsyth, Y. Takeoka and M. Rikukawa, Improvement of charge/discharge properties of oligoether electrolytes by zwitterions with an attached cyano group for use in lithium-ion secondary batteries, *Electrochim. Acta*, 2015, **186**, 471–477.

66 S. Yamaguchi, M. Yoshizawa-Fujita, Y. Takeoka and M. Rikukawa, Effect of a pyrrolidinium zwitterion on charge/discharge cycle properties of Li/LiCoO2 and graphite/Li cells containing an ionic liquid electrolyte, *J. Power Sources*, 2016, **331**, 308–314.

67 X. Peng, H. Liu, Q. Yin, J. Wu, P. Chen, G. Zhang, G. Liu, C. Wu and Y. Xie, A zwitterionic gel electrolyte for efficient solid-state supercapacitors, *Nat. Commun.*, , DOI:10.1038/ncomms11782.

68 A. Bakandritsos, D. D. Chronopoulos, P. Jakubec, M. Pykal, K. Čépe, T. Steriotis, S. Kalytchuk, M. Petr, R. Zbořil and M. Otyepka, High-Performance Supercapacitors Based on a Zwitterionic Network of Covalently Functionalized Graphene with Iron Tetraaminophthalocyanine, *Adv. Funct. Mater.*, 2018, **28**, 1801111.

69 T. Chakrabarty, A. K. Singh and V. K. Shahi, Zwitterionic silica copolymer based crosslinked organic–inorganic hybrid polymer electrolyte membranes for fuel cell applications, *RSC Adv.*, 2012, **2**, 1949–1961.

70 B. Cao, Q. Tang, L. Li, C.-J. Lee, H. Wang, Y. Zhang, H. Castaneda and G. Cheng, Integrated zwitterionic conjugated poly (carboxybetaine thiophene) as a new biomaterial platform, *Chem. Sci.*, 2015, **6**, 782–788.

71 B. P. Tripathi and V. K. Shahi, 3-[[3-(Triethoxysilyl) propyl] amino] propane-1-sulfonic acid− poly (vinyl alcohol) cross-linked zwitterionic polymer electrolyte

membranes for direct methanol fuel cell applications, *ACS Appl. Mater. Interfaces*, 2009, **1**, 1002–1012.

72 A. Narita, W. Shibayama and H. Ohno, Structural factors to improve physico-chemical properties of zwitterions as ion conductive matrices, *J. Mater. Chem.*, 2006, **16**, 1475–1482.

73 M. Yoshizawa, A. Narita and H. Ohno, Design of ionic liquids for electrochemical applications, *Aust. J. Chem.*, 2004, **57**, 139–144.

74 N. J. English and C. J. Waldron, Perspectives on external electric fields in molecular simulation: progress, prospects and challenges, *Phys. Chem. Chem. Phys.*, 2015, **17**, 12407–12440.

75 F. Mugele and J.-C. Baret, Electrowetting: from basics to applications, *J. Phys. Condens. matter*, 2005, **17**, R705.

76 Z. He, H. Cui, S. Hao, L. Wang and J. Zhou, Electric-field effects on ionic hydration: a molecular dynamics study, *J. Phys. Chem. B*, 2018, **122**, 5991–5998.

77 Y. Zhao, K. Dong, X. Liu, S. Zhang, J. Zhu and J. Wang, Structure of ionic liquids under external electric field: a molecular dynamics simulation, *Mol. Simul.*, 2012, **38**, 172–178.

78 G. Ren, R. Shi and Y. Wang, Structural, dynamic, and transport properties of concentrated aqueous sodium chloride solutions under an external static electric field, *J. Phys. Chem. B*, 2014, **118**, 4404–4411.

79 S. Kerisit, M. Vijayakumar, K. S. Han and K. T. Mueller, Solvation structure and transport properties of alkali cations in dimethyl sulfoxide under exogenous static electric fields, *J. Chem. Phys.*, 2015, **142**, 224502.

80 S. L. Perkins, P. Painter and C. M. Colina, Experimental and computational studies of choline chloride-based deep eutectic solvents, *J. Chem. Eng. Data*, 2014, **59**, 3652–3662.

81 K. G. Sprenger, V. W. Jaeger and J. Pfaendtner, The general AMBER force field (GAFF) can accurately predict thermodynamic and transport properties of many ionic liquids, *J. Phys. Chem. B*, 2015, **119**, 5882–5895.

82 Y. Zhang and E. J. Maginn, A simple AIMD approach to derive atomic charges for condensed phase simulation of ionic liquids, *J. Phys. Chem. B*, 2012, **116**, 10036–10048.

83 L. Martínez, R. Andrade, E. G. Birgin and J. M. Martínez, PACKMOL: a package for building initial configurations for molecular dynamics simulations, *J. Comput. Chem.*, 2009, **30**, 2157–2164.

84 W. Humphrey, A. Dalke and K. Schulten, VMD: visual molecular dynamics, *J. Mol. Graph.*, 1996, **14**, 33–38.

85 B. Doherty, X. Zhong, S. Gathiaka, B. Li and O. Acevedo, Revisiting OPLS Force

Field Parameters for Ionic Liquid Simulations, *J. Chem. Theory Comput.*, 2017, **13**, 6131–6145.

86 W. L. Jorgensen, D. S. Maxwell and J. Tirado-Rives, Development and testing of the OPLS all-atom force field on conformational energetics and properties of organic liquids, *J. Am. Chem. Soc.*, 1996, **118**, 11225–11236.

87 Q. Shao, Y. He, A. D. White and S. Jiang, Difference in hydration between carboxybetaine and sulfobetaine, *J. Phys. Chem. B*, 2010, **114**, 16625–16631.

88 H. J. C. Berendsen, J. P. M. Postma, W. F. Van Gunsteren, A. Dinola and J. R. Haak, Molecular dynamics with coupling to an external bath, *J. Chem. Phys.*, 1984, **81**, 3684–3690.

89 G. Bussi, D. Donadio and M. Parrinello, Canonical sampling through velocity rescaling, *J. Chem. Phys.*, 2007, **126**, 014101.

90 T. Darden, D. York and L. Pedersen, Particle mesh Ewald: An N ·log(N) method for Ewald sums in large systems, *J. Chem. Phys.*, 1993, **98**, 10089–10092.

91 B. Hess, H. Bekker, H. J. C. Berendsen and J. G. E. M. Fraaije, LINCS: A Linear Constraint Solver for molecular simulations, *J. Comput. Chem.*, 1997, **18**, 1463–1472.

92 M. J. Abraham, T. Murtola, R. Schulz, S. Páll, J. C. Smith, B. Hess and E. Lindah, Gromacs: High performance molecular simulations through multi-level parallelism from laptops to supercomputers, *SoftwareX*, 2015, **1**–**2**, 19–25.

93 E. Choi and A. Yethiraj, Entropic mechanism for the lower critical solution temperature of poly (ethylene oxide) in a room temperature ionic liquid, *ACS Macro Lett.*, 2015, **4**, 799–803.

94 J. G. McDaniel and A. Yethiraj, Influence of electronic polarization on the structure of ionic liquids, *J. Phys. Chem. Lett.*, 2018, **9**, 4765–4770.

95 C. Y. Son, J. G. McDaniel, J. R. Schmidt, Q. Cui and A. Yethiraj, First-principles united atom force field for the ionic liquid BMIM+ BF4–: An alternative to charge scaling, *J. Phys. Chem. B*, 2016, **120**, 3560–3568.

96 D. Bedrov, J. P. Piquemal, O. Borodin, A. D. MacKerell, B. Roux and C. Schröder, Molecular Dynamics Simulations of Ionic Liquids and Electrolytes Using Polarizable Force Fields, *Chem. Rev.*, 2019, **119**, 7940–7995.

97 J. W. Fergus, Ceramic and polymeric solid electrolytes for lithium-ion batteries, *J. Power Sources*, 2010, **195**, 4554–4569.

98 A. M. Stephan, Review on gel polymer electrolytes for lithium batteries, *Eur. Polym. J.*, 2006, **42**, 21–42.

99 A. Abouimrane, P.-J. Alarco, Y. Abu-Lebdeh, I. Davidson and M. Armand, Plastic crystalline phases of crown ether: salt complexes and their utilization in lithium-metal batteries, *J. Power Sources*, 2007, **174**, 1193–1196.

100 R. E. A. Dillon and D. F. Shriver, Ion transport in cryptand and crown ether lithium salt complexes, *Chem. Mater.*, 1999, **11**, 3296–3301.

101 K. Dokko, N. Tachikawa, K. Yamauchi, M. Tsuchiya, A. Yamazaki, E. Takashima, J.-W. Park, K. Ueno, S. Seki and N. Serizawa, Solvate ionic liquid electrolyte for Li–S batteries, *J. Electrochem. Soc.*, 2013, **160**, A1304.

102 W. A. Henderson, N. R. Brooks, W. W. Brennessel and V. G. Young, Triglyme−Li+ cation solvate structures: models for amorphous concentrated liquid and polymer electrolytes (I), *Chem. Mater.*, 2003, **15**, 4679–4684.

103 T. Mandai, K. Yoshida, K. Ueno, K. Dokko and M. Watanabe, Criteria for solvate ionic liquids, *Phys. Chem. Chem. Phys.*, 2014, **16**, 8761–8772.

104 K. Yoshida, M. Nakamura, Y. Kazue, N. Tachikawa, S. Tsuzuki, S. Seki, K. Dokko and M. Watanabe, Oxidative-stability enhancement and charge transport mechanism in glyme–lithium salt equimolar complexes, *J. Am. Chem. Soc.*, 2011, **133**, 13121–13129.

105 K. Yoshida, M. Tsuchiya, N. Tachikawa, K. Dokko and M. Watanabe, Change from glyme solutions to quasi-ionic liquids for binary mixtures consisting of lithium bis (trifluoromethanesulfonyl) amide and glymes, *J. Phys. Chem. C*, 2011, **115**, 18384–18394.

106 C. Do, P. Lunkenheimer, D. Diddens, M. Götz, M. Weiß, A. Loidl, X.-G. Sun, J. Allgaier and M. Ohl, Li+ transport in poly (ethylene oxide) based electrolytes: neutron scattering, dielectric spectroscopy, and molecular dynamics simulations, *Phys. Rev. Lett.*, 2013, **111**, 18301.

107 Z. Xue, D. He and X. Xie, Poly(ethylene oxide)-based electrolytes for lithium-ion batteries, *J. Mater. Chem. A*, 2015, **3**, 19218–19253.

108 O. Buriez, Y. B. Han, J. Hou, J. B. Kerr, J. Qiao, S. E. Sloop, M. Tian and S. Wang, Performance limitations of polymer electrolytes based on ethylene oxide polymers, *J. Power Sources*, 2000, **89**, 149–155.

109 H. Zhang, F. Chen, O. Lakuntza, U. Oteo, L. Qiao, M. Martinez-Ibañez, H. Zhu, J. Carrasco, M. Forsyth and M. Armand, *Angew. Chemie - Int. Ed.*, 2019, 58, 12070–12075.

110 T. Morioka, K. Ota and Y. Tominaga, Effect of oxyethylene side chains on ion-conductive properties of polycarbonate-based electrolytes, *Polymer (Guildf).*, 2016, **84**, 21–26.

111 C. Zhang, K. Ueno, A. Yamazaki, K. Yoshida, H. Moon, T. Mandai, Y. Umebayashi, K. Dokko and M. Watanabe, Chelate effects in glyme/lithium bis(trifluoromethanesulfonyl)amide solvate ionic liquids. I. Stability of solvate cations and correlation with electrolyte properties, *J. Phys. Chem. B*, 2014, **118**, 5144–5153.

112 A. Narita, W. Shibayama, K. Sakamoto, T. Mizumo, N. Matsumi and H. Ohno, Lithium ion conduction in an organoborate zwitterion-LiTFSI mixture, *Chem.*

Commun., 2006, 1926–1928.

113 Y. Liu, M. Sheri, M. D. Cole, T. Emrick and T. P. Russell, Combining fullerenes and zwitterions in non-conjugated polymer interlayers to raise solar cell efficiency, *Angew. Chemie Int. Ed.*, 2018, **57**, 9675–9678.

114 C. Fu, L. Xu, F. W. Aquino, A. V. Cresce, M. Gobet, S. G. Greenbaum, K. Xu, B. M. Wong and J. Guo, Correlating Li+-Solvation Structure and its Electrochemical Reaction Kinetics with Sulfur in Subnano Confinement, *J. Phys. Chem. Lett.*, 2018, **9**, 1739–1745.

115 D. Brandell, A. Liivat, A. Aabloo and J. O. Thomas, Molecular dynamics simulation of the crystalline short-chain polymer system LiPF 6· PEO 6 (M w∼ 1000), *J. Mater. Chem.*, 2005, **15**, 4338–4345.

116 D. Brandell, A. Liivat, H. Kasemägi, A. Aabloo and J. O. Thomas, Molecular dynamics simulation of the LiPF 6 ·PEO 6 structure, *J. Mater. Chem.*, 2005, **15**, 1422–1428.

117 M. T. Nguyen and Q. Shao, Effect of Zwitterionic Molecules on Ionic Transport under Electric Fields: A Molecular Simulation Study, *J. Chem. Eng. Data*, 2020, **65**, 385–395.

118 V. Di Noto, S. Lavina, G. A. Giffin, E. Negro and B. Scrosati, Polymer electrolytes: Present, past and future, *Electrochim. Acta*, 2011, **57**, 4–13.

119 B. Adhikari and S. Majumdar, Polymers in sensor applications, *Prog. Polym. Sci.*, 2004, **29**, 699–766.

120 D. M. Seo, O. Borodin, S.-D. Han, Q. Ly, P. D. Boyle and W. A. Henderson, Electrolyte Solvation and Ionic Association, *J. Electrochem. Soc.*, 2012, **159**, A553–A565.

121 M. Andreev, J. J. De Pablo, A. Chremos and J. F. Douglas, Influence of Ion Solvation on the Properties of Electrolyte Solutions, *J. Phys. Chem. B*, 2018, **122**, 4029–4034.

122 T. Rüther, A. I. Bhatt, A. S. Best, K. R. Harris and A. F. Hollenkamp, Electrolytes for Lithium (Sodium) Batteries Based on Ionic Liquids: Highlighting the Key Role Played by the Anion, *Batter. Supercaps*, 2020, **3**, 793–827.

123 J. D. Forero-Saboya, E. Marchante, R. B. Araujo, D. Monti, P. Johansson and A. Ponrouch, Cation Solvation and Physicochemical Properties of Ca Battery Electrolytes, *J. Phys. Chem. C*, 2019, **123**, 29524–29532.

124 N. N. Rajput, T. J. Seguin, B. M. Wood, X. Qu and K. A. Persson, Elucidating Solvation Structures for Rational Design of Multivalent Electrolytes—A Review, *Top. Curr. Chem.*, 2018, **376**, 19.

125 B. E. Conway, Electrolyte Solutions: Solvation and Structural Aspects, *Annu. Rev. Phys. Chem.*, 1966, **17**, 481–528.

126 D. M. Seo, S. Reininger, M. Kutcher, K. Redmond, W. B. Euler and B. L. Lucht, Role of mixed solvation and ion pairing in the solution structure of lithium ion battery electrolytes, *J. Phys. Chem. C*, 2015, **119**, 14038–14046.

127 D. Moreno, M. Gonzalez-Miquel, V. R. Ferro and J. Palomar, Molecular and Thermodynamic Properties of Zwitterions versus Ionic Liquids: A Comprehensive Computational Analysis to Develop Advanced Separation Processes, *ChemPhysChem*, 2018, **19**, 801–815.

128 H. Qin and M. J. Panzer, Zwitterionic Copolymer-Supported Ionogel Electrolytes Featuring a Sodium Salt/Ionic Liquid Solution, *Chem. Mater.*, 2020, **32**, 7951–7957.

129 H. S. Woo, H. Son, J. Y. Min, J. Rhee, H. T. Lee and D. W. Kim, Ionic liquid-based gel polymer electrolyte containing zwitterion for lithium-oxygen batteries, *Electrochim. Acta*, 2020, **345**, 136248.

130 B. Soberats, M. Yoshio, T. Ichikawa, H. Ohno and T. Kato, Zwitterionic liquid crystals as 1D and 3D lithium ion transport media, *J. Mater. Chem. A*, 2015, **3**, 11232–11238.

131 G. Li, X. Guan, A. Wang, C. Wang and J. Luo, Cations and anions regulation through zwitterionic gel electrolytes for stable lithium metal anodes, *Energy Storage Mater.*, 2020, **24**, 574–578.

132 Z. Zhang, P. Zhang, Z. Liu, B. Du and Z. Peng, A Novel Zwitterionic Ionic Liquid-Based Electrolyte for More Efficient and Safer Lithium-Sulfur Batteries, *ACS Appl. Mater. Interfaces*, 2020, **12**, 11635–11642.

133 P. Wang, L. Tseng, W. Li, C. Lin and T. Wen, Zwitterionic polymer coupled with high concentrated electrolytes to achieve high ionic conductivity and wide electrochemical window for supreme specific energy aqueous supercapacitors, *J. Energy Storage*, 2021, **42**, 103060.

134 F. Makhlooghiazad, L. A. O'Dell, L. Porcarelli, C. Forsyth, N. Quazi, M. Asadi, O. Hutt, D. Mecerreyes, M. Forsyth and J. M. Pringle, Zwitterionic materials with disorder and plasticity and their application as non-volatile solid or liquid electrolytes, *Nat. Mater.*, 2022, **21**, 228–236.

135 M. T. Nguyen and Q. Shao, Effects of zwitterionic molecules on ionic association in ethylene oxide-based electrolytes, *Fluid Phase Equilib.*, 2020, **515**, 112572.

136 K. Pożyczka, M. Marzantowicz, J. R. Dygas and F. Krok, ionic conductivity and lithium transference number of poly(ethylene oxide):LiTFSI system, *Electrochim. Acta*, 2017, **227**, 127–135.

137 P. Bennington, C. Deng, D. Sharon, M. A. Webb, J. J. de Pablo, P. F. Nealey and S. N. Patel, Role of solvation site segmental dynamics on ion transport in ethylene-oxide based side-chain polymer electrolytes, *J. Mater. Chem. A*, 2021, **9**, 9937–9951.

138 K. M. Diederichsen, E. J. McShane and B. D. McCloskey, Promising Routes to a High Li+ Transference Number Electrolyte for Lithium Ion Batteries, *ACS Energy*

Lett., 2017, **2**, 2563–2575.

139 A. France-Lanord, Y. Wang, T. Xie, J. A. Johnson, Y. Shao-Horn and J. C. Grossman, Effect of Chemical Variations in the Structure of Poly(ethylene oxide)-Based Polymers on Lithium Transport in Concentrated Electrolytes, *Chem. Mater.*, 2020, **32**, 121–126.

140 J. R. Keith and V. Ganesan, Ion transport mechanisms in salt-doped polymerized zwitterionic electrolytes, *J. Polym. Sci.*, 2020, **58**, 578–588.

141 T. C. Lourenço, M. Ebadi, M. J. Panzer, D. Brandell and L. T. Costa, A molecular dynamics study of a fully zwitterionic copolymer/ionic liquid-based electrolyte: Li+ transport mechanisms and ionic interactions, *J. Comput. Chem.*, 2021, 1–15.

142 Z. Li, O. Borodin, G. D. Smith and D. Bedrov, Effect of organic solvents on Li+ Ion solvation and transport in ionic liquid electrolytes: A molecular dynamics simulation study, *J. Phys. Chem. B*, 2015, **119**, 3085–3096.

143 L. S. Dodda, I. Cabeza de Vaca, J. Tirado-Rives and W. L. Jorgensen, LigParGen web server: an automatic OPLS-AA parameter generator for organic ligands, *Nucleic Acids Res.*, 2017, **45**, W331–W336.

144 E. Mullins, R. Oldland, Y. A. Liu, S. Wang, S. I. Sandler, C. C. Chen, M. Zwolak and K. C. Seavey, Sigma-profile database for using COSMO-based thermodynamic methods, *Ind. Eng. Chem. Res.*, 2006, **45**, 4389–4415.

145 M. J. Frisch, G. W. Trucks, H. B. Schlegel, G. E. Scuseria, M. a. Robb, J. R. Cheeseman, G. Scalmani, V. Barone, G. a. Petersson, H. Nakatsuji, X. Li, M. Caricato, a. V. Marenich, J. Bloino, B. G. Janesko, R. Gomperts, B. Mennucci, H. P. Hratchian, J. V. Ortiz, a. F. Izmaylov, J. L. Sonnenberg, D. Williams-Young, F. Ding, F. Lipparini, F. Egidi, J. Goings, B. Peng, A. Petrone, T. Henderson, D. Ranasinghe, V. G. Zakrzewski, J. Gao, N. Rega, G. Zheng, W. Liang, M. Hada, M. Ehara, K. Toyota, R. Fukuda, J. Hasegawa, M. Ishida, T. Nakajima, Y. Honda, O. Kitao, H. Nakai, T. Vreven, K. Throssell, J. a. Montgomery Jr., J. E. Peralta, F. Ogliaro, M. J. Bearpark, J. J. Heyd, E. N. Brothers, K. N. Kudin, V. N. Staroverov, T. a. Keith, R. Kobayashi, J. Normand, K. Raghavachari, a. P. Rendell, J. C. Burant, S. S. Iyengar, J. Tomasi, M. Cossi, J. M. Millam, M. Klene, C. Adamo, R. Cammi, J. W. Ochterski, R. L. Martin, K. Morokuma, O. Farkas, J. B. Foresman and D. J. Fox, 2016, Gaussian 16, Revision C.01, Gaussian, Inc., Wallin.

146 E. Mullins, Y. A. Liu, A. Ghaderi and S. D. Fast, Sigma profile database for predicting solid solubility in pure and mixed solvent mixtures for organic pharmacological compounds with COSMO-based thermodynamic methods, *Ind. Eng. Chem. Res.*, 2008, **47**, 1707–1725.

147 A. Klamt, V. Jonas, T. Bürger and J. C. W. Lohrenz, Refinement and parametrization of COSMO-RS, *J. Phys. Chem. A*, 1998, **102**, 5074–5085.

148 D. E. Galvez-Aranda and J. M. Seminario, Ion Pairing, Clustering and Transport in a LiFSI-TMP Electrolyte as Functions of Salt Concentration using Molecular Dynamics Simulations, *J. Electrochem. Soc.*, 2021, **168**, 040511.

149 N. N. Rajput, V. Murugesan, Y. Shin, K. S. Han, K. C. Lau, J. Chen, J. Liu, L. A. Curtiss, K. T. Mueller and K. A. Persson, Elucidating the Solvation Structure and Dynamics of Lithium Polysulfides Resulting from Competitive Salt and Solvent Interactions, *Chem. Mater.*, 2017, **29**, 3375–3379.

150 V. Lesch, Z. Li, D. Bedrov, O. Borodin and A. Heuer, The influence of cations on lithium ion coordination and transport in ionic liquid electrolytes: A MD simulation study, *Phys. Chem. Chem. Phys.*, 2016, **18**, 382–392.

151 T. Gao and W. Lu, Mechanism and effect of thermal degradation on electrolyte ionic diffusivity in Li-ion batteries: A molecular dynamics study, *Electrochim. Acta*, 2019, **323**, 134791.

152 N. Sanchez-Ramirez, V. L. Martins, R. A. Ando, F. F. Camilo, S. M. Urahata, M. C. C. Ribeiro and R. M. Torresi, Physicochemical properties of three ionic liquids containing a tetracyanoborate anion and their lithium salt mixtures, *J. Phys. Chem. B*, 2014, **118**, 8772–8781.

153 N. Molinari, J. P. Mailoa and B. Kozinsky, Effect of Salt Concentration on Ion Clustering and Transport in Polymer Solid Electrolytes: A Molecular Dynamics Study of PEO-LiTFSI, *Chem. Mater.*, 2018, **30**, 6298–6306.

154 B. K. Annis, M. H. Kim, G. D. Wignall, O. Borodin and G. D. Smith, Study of the influence of LiI on the chain conformations of poly(ethylene oxide) in the melt by small-angle neutron scattering and molecular dynamics simulations, *Macromolecules*, 2000, **33**, 7544–7548.

155 W. S. Loo, K. I. Mongcopa, D. A. Gribble, A. A. Faraone and N. P. Balsara, Investigating the Effect of Added Salt on the Chain Dimensions of Poly(ethylene oxide) through Small-Angle Neutron Scattering, *Macromolecules*, 2019, **52**, 8724–8732.

156 Y. Kamiyama, M. Shibata, R. Kanzaki and K. Fujii, Lithium-ion coordination-induced conformational change of PEG chains in ionic-liquid-based electrolytes, *Phys. Chem. Chem. Phys.*, 2020, **22**, 5561–5567.

157 C. Fang, W. S. Loo and R. Wang, Salt Activity Coefficient and Chain Statistics in Poly(ethylene oxide)-Based Electrolytes, *Macromolecules*, 2021, **54**, 2873–2881.

158 O. Borodin and G. D. Smith, Mechanism of ion transport in amorphous poly(ethylene oxide)/ LiTFSI from molecular dynamics simulations, *Macromolecules*, 2006, **39**, 1620–1629.

159 M. R. Islam and C. C. Chen, COSMO-SAC sigma profile generation with conceptual segment concept, *Ind. Eng. Chem. Res.*, 2015, **54**, 4441–4454.

160 M. N. Ahmad, N. U. Karim, E. Normaya, B. Mat Piah, A. Iqbal and K. H. Ku Bulat, Artocarpus altilis extracts as a food-borne pathogen and oxidation inhibitors: RSM, COSMO RS, and molecular docking approaches, *Sci. Rep.*, 2020, **10**, 1–14.

161 A. Klamt, COSMO-RS for aqueous solvation and interfaces, *Fluid Phase Equilib.*, 2016, **407**, 152–158.

162 S. Rezaei Motlagh, R. Harun, D. Awang Biak, S. Hussain, W. Wan Ab Karim Ghani, R. Khezri, C. Wilfred and A. Elgharbawy, Screening of Suitable Ionic Liquids as Green Solvents for Extraction of Eicosapentaenoic Acid (EPA) from Microalgae Biomass Using COSMO-RS Model, *Molecules*, 2019, **24**, 713.

163 M. Hornig and A. Klamt, COSMOfrag: A novel tool for high-throughput ADME property prediction and similarity screening based on quantum chemistry, *J. Chem. Inf. Model.*, 2005, **45**, 1169–1177.

164 D. J. Brooks, B. V. Merinov, W. A. Goddard, B. Kozinsky and J. Mailoa, Atomistic Description of Ionic Diffusion in PEO–LiTFSI: Effect of Temperature, Molecular Weight, and Ionic Concentration, *Macromolecules*, 2018, **51**, 8987–8995.

165 S. Bush, Y. Duan, B. Gilbert, A. Hussey, J. Levy, D. Miller, R. Pooser and M. Syamlal, *Fossil Energy Workshop on Quantum Information Science & Technology (Summary Report)*, National Energy Technology Laboratory (NETL), Pittsburgh, PA, Morgantown, WV …, 2020.

166 G. S. Barron, B. T. Gard, O. J. Altman, N. J. Mayhall, E. Barnes and S. E. Economou, Preserving Symmetries for Variational Quantum Eigensolvers in the Presence of Noise, *Phys. Rev. Appl.*, 2021, **16**, 034003.

167 W. M. Kirby and P. J. Love, Contextuality Test of the Nonclassicality of Variational Quantum Eigensolvers, *Phys. Rev. Lett.*, 2019, **123**, 200501.

168 S.-X. Zhang, Z.-Q. Wan, C.-K. Lee, C.-Y. Hsieh, S. Zhang and H. Yao, Variational Quantum-Neural Hybrid Eigensolver, *Phys. Rev. Lett.*, 2022, **128**, 120502.

169 A. Kandala, A. Mezzacapo, K. Temme, M. Takita, M. Brink, J. M. Chow and J. M. Gambetta, Hardware-efficient variational quantum eigensolver for small molecules and quantum magnets, *Nature*, 2017, **549**, 242–246.

170 R. M. Parrish, E. G. Hohenstein, P. L. McMahon and T. J. Martínez, Quantum Computation of Electronic Transitions Using a Variational Quantum Eigensolver, *Phys. Rev. Lett.*, 2019, **122**, 230401.

171 N. H. Stair, R. Huang and F. A. Evangelista, A Multireference Quantum Krylov Algorithm for Strongly Correlated Electrons, *J. Chem. Theory Comput.*, 2020, **16**, 2236–2245.

172 M. Rossmannek, P. K. Barkoutsos, P. J. Ollitrault and I. Tavernelli, Quantum HF/DFT-embedding algorithms for electronic structure calculations: Scaling up to complex molecular systems, *J. Chem. Phys.*, 2021, **154**, 114105.

173 N. P. D. Sawaya, T. Menke, T. H. Kyaw, S. Johri, A. Aspuru-Guzik and G. G. Guerreschi, Resource-efficient digital quantum simulation of d-level systems for photonic, vibrational, and spin-s Hamiltonians, *npj Quantum Inf.*, 2020, **6**, 49.

174 V. Barone, M. Biczysko and J. Bloino, Fully anharmonic IR and Raman spectra of medium-size molecular systems: Accuracy and interpretation, *Phys. Chem. Chem. Phys.*, 2014, **16**, 1759–1787.

175 E. L. Sibert, Modeling vibrational anharmonicity in infrared spectra of high frequency vibrations of polyatomic molecules, *J. Chem. Phys.*, 2019, **150**, 090901.

176 B. Njegic and M. S. Gordon, Exploring the effect of anharmonicity of molecular vibrations on thermodynamic properties, *J. Chem. Phys.*, 2006, **125**, 224102.

177 T. L. Nguyen and J. R. Barker, Sums and densities of fully coupled anharmonic vibrational states: A comparison of three practical methods, *J. Phys. Chem. A*, 2010, **114**, 3718–3730.

178 C. Aieta, M. Micciarelli, G. Bertaina and M. Ceotto, Anharmonic quantum nuclear densities from full dimensional vibrational eigenfunctions with application to protonated glycine, *Nat. Commun.*, 2020, **11**, 4348.

179 O. Christiansen, A second quantization formulation of multimode dynamics, *J. Chem. Phys.*, 2004, **120**, 2140–2148.

180 P. J. Ollitrault, A. Kandala, C.-F. Chen, P. K. Barkoutsos, A. Mezzacapo, M. Pistoia, S. Sheldon, S. Woerner, J. M. Gambetta and I. Tavernelli, Quantum equation of motion for computing molecular excitation energies on a noisy quantum processor, *Phys. Rev. Res.*, 2020, **2**, 043140.

181 G. T. Rochelle, Amine Scrubbing for CO 2 Capture, *Science (80-.).*, 2009, **325**, 1652–1654.

182 G. Aleksandrowicz, T. Alexander, P. Barkoutsos, L. Bello, Y. Ben-Haim, D. Bucher, F. J. Cabrera-Hernández, J. Carballo-Franquis, A. Chen, C.-F. Chen, J. M. Chow, A. D. Córcoles-Gonzales, A. A. J. Cross, A. A. J. Cross, J. Cruz-Benito, C. Culver, S. D. L. P. González, E. D. La Torre, D. Ding, E. Dumitrescu, I. Duran, P. Eendebak, M. Everitt, I. F. Sertage, A. Frisch, A. Fuhrer, J. Gambetta, B. G. Gago, J. Gomez-Mosquera, D. Greenberg, I. Hamamura, V. Havlicek, J. Hellmers, Ł. Herok, H. Horii, S. Hu, T. Imamichi, T. Itoko, A. Javadi-Abhari, N. Kanazawa, A. Karazeev, K. Krsulich, P. Liu, Y. Luh, Y. Maeng, M. Marques, F. J. Martín-Fernández, D. T. McClure, D. McKay, S. Meesala, A. Mezzacapo, N. Moll, D. M. Rodríguez, G. Nannicini, P. Nation, P. Ollitrault, L. J. O'Riordan, H. Paik, J. Pérez, A. Phan, M. Pistoia, V. Prutyanov, M. Reuter, J. Rice, A. R. Davila, R. H. P. Rudy, M. Ryu, N. Sathaye, C. Schnabel, E. Schoute, K. Setia, Y. Shi, A. Silva, Y. Siraichi, S. Sivarajah, J. A. Smolin, M. Soeken, H. Takahashi, I. Tavernelli, C. Taylor, P. Taylour, K. Trabing, M. Treinish, W. Turner, D. Vogt-Lee, C. Vuillot, J. A. Wildstrom, J. Wilson, E. Winston, C. Wood, S. Wood, S. Wörner, I. Y. Akhalwaya and C. Zoufal, Qiskit: An Open-source Framework for Quantum Computing, , DOI:10.5281/ZENODO.2562111.

183 Q. Sun, T. C. Berkelbach, N. S. Blunt, G. H. Booth, S. Guo, Z. Li, J. Liu, J. D. McClain, E. R. Sayfutyarova, S. Sharma, S. Wouters and G. K. Chan, PySCF: the Python-based simulations of chemistry framework, *WIREs Comput. Mol. Sci.*, 2018, **8**, e1340.

184 Q. Sun, Libcint: An efficient general integral library for Gaussian basis functions, *J. Comput. Chem.*, 2015, **36**, 1664–1671.

185 B. Bauer, S. Bravyi, M. Motta and G. K.-L. Chan, Quantum Algorithms for Quantum Chemistry and Quantum Materials Science, *Chem. Rev.*, 2020, **120**, 12685–12717.

186 D. C. Liu and J. Nocedal, On the limited memory BFGS method for large scale optimization, *Math. Program.*, 1989, **45**, 503–528.

187 D. F. Shanno, Conditioning of quasi-Newton methods for function minimization, *Math. Comput.*, 1970, **24**, 647–656.

188 G. Kresse and J. Furthmüller, Efficiency of ab-initio total energy calculations for metals and semiconductors using a plane-wave basis set, *Comput. Mater. Sci.*, 1996, **6**, 15–50.

189 G. Henkelman, B. P. Uberuaga and H. Jónsson, A climbing image nudged elastic band method for finding saddle points and minimum energy paths, *J. Chem. Phys.*, 2000, **113**, 9901–9904.

190 W. Li, Z. Huang, C. Cao, Y. Huang, Z. Shuai, X. Sun, J. Sun, X. Yuan and D. Lv, Toward practical quantum embedding simulation of realistic chemical systems on near-term quantum computers, *Chem. Sci.*, 2022, **13**, 8953–8962.

191 C. Cao, J. Hu, W. Zhang, X. Xu, D. Chen, F. Yu, J. Li, H.-S. Hu, D. Lv and M.-H. Yung, Progress toward larger molecular simulation on a quantum computer: Simulating a system with up to 28 qubits accelerated by point-group symmetry, *Phys. Rev. A*, 2022, **105**, 062452.

192 A. Peruzzo, J. McClean, P. Shadbolt, M.-H. Yung, X.-Q. Zhou, P. J. Love, A. Aspuru-Guzik and J. L. O'Brien, A variational eigenvalue solver on a photonic quantum processor, *Nat. Commun.*, 2014, **5**, 4213.

193 J. M. Bowman, The self-consistent-field approach to polyatomic vibrations, *Acc. Chem. Res.*, 1986, **19**, 202–208.

194 J. Kongsted and O. Christiansen, Automatic generation of force fields and property surfaces for use in variational vibrational calculations of anharmonic vibrational energies and zero-point vibrational averaged properties, *J. Chem. Phys.*, 2006, **125**, 124108.

195 L. Veis, J. Višňák, H. Nishizawa, H. Nakai and J. Pittner, Quantum chemistry beyond Born–Oppenheimer approximation on a quantum computer: A simulated phase estimation study, *Int. J. Quantum Chem.*, 2016, **116**, 1328–1336.

196 K. Temme, S. Bravyi and J. M. Gambetta, Error Mitigation for Short-Depth Quantum Circuits, *Phys. Rev. Lett.*, 2017, **119**, 180509.

197 A. G. Császár, I. Simkó, T. Szidarovszky, G. C. Groenenboom, T. Karman and A. Van Der Avoird, Rotational-vibrational resonance states, *Phys. Chem. Chem. Phys.*, 2020, **22**, 15081–15104.

198 A. G. Császár, C. Fábri, T. Szidarovszky, E. Mátyus, T. Furtenbacher and G. Czakó, The fourth age of quantum chemistry: Molecules in motion, *Phys. Chem. Chem.*

Phys., 2012, **14**, 1085–1106.

199 E. Lötstedt, K. Yamanouchi, T. Tsuchiya and Y. Tachikawa, Calculation of vibrational eigenenergies on a quantum computer: Application to the Fermi resonance in CO2, *Phys. Rev. A*, 2021, **103**, 062609.

VITA

Manh Tien Nguyen

Education

Doctor of Philosophy, Chemical Engineering Aug 2018 – Aug 2023 (expected)

University of Kentucky, Lexington, Kentucky, USA

Bachelor of Chemical Engineering Sep 2009 – April 2014

Hochiminh City University of Technology, Vietnam

Professional positions

DOE Office of Science Graduate Student Research Program Aug 2022 – Aug 2023

National Energy Technology Laboratory, Pittsburgh-Pennsylvania

Intern Jun 2022 – Aug 2022

National Energy Technology Laboratory, Pittsburgh-Pennsylvania

Instrument Operator Sep 2016 – Jun 2018

Celerion Inc, Lincoln-Nebraska

Awards

Department of Energy's (DOE) Office of Science Graduate Student Research Program Award 2023

University of Kentucky CME Department - Outstanding Graduate Student Award 2023

Publications

Manh Tien Nguyen, Yueh-Lin Lee, Dominic Alfonso, Qing Shao, Yuhua Duan. "Description of Reaction and Vibrational Energetics of CO2-NH3 Interaction Using Quantum Computing Algorithms". AVS Quantum Science 5.1 (2023): 013801.

Abbas, Usman L., Qi Qiao, Manh Tien Nguyen, Jian Shi, and Qing Shao. "Structure and Hydrogen Bonds of Hydrophobic Deep Eutectic Solvent-Aqueous Liquid-Liquid Interfaces." AIChE Journal (2021): e17427.

Ding, Jiaqi, Nan Xu, Manh Tien Nguyen, Qi Qiao, Yao Shi, Yi He, and Qing Shao. "Machine learning for molecular thermodynamics." Chinese Journal of Chemical Engineering 31 (2021): 227-239.

Abbas, Usman L., Qi Qiao, Manh Tien Nguyen, Jian Shi, and Qing Shao. "Molecular dynamics simulations of heterogeneous hydrogen bond environment in hydrophobic deep eutectic solvents." AIChE Journal (2021): e17382.

Manh Tien Nguyen, and Qing Shao. "Effects of zwitterionic molecules on ionic association in ethylene oxide-based electrolytes." Fluid Phase Equilibria 515 (2020): 112572.

Manh Tien Nguyen, and Qing Shao. "Effect of Zwitterionic Molecules on Ionic Transport under Electric Fields: A Molecular Simulation Study." Journal of Chemical & Engineering Data 65, no. 2 (2019): 385-395.